



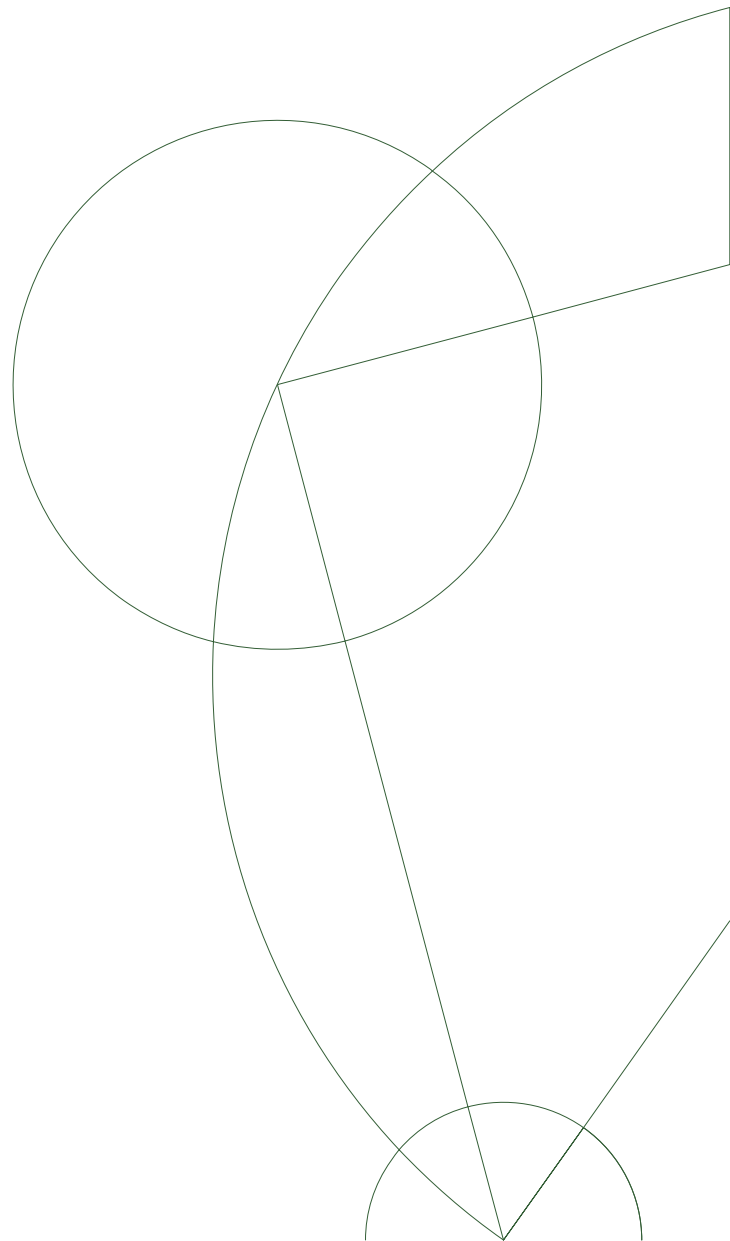
Master's Thesis in Physics

Daniel Steffensen

Topological Magnetic Superconductors

Supervisors: Prof. B.M. Andersen & Dr. P. Kotetes

September 20, 2017



Topological Magnetic Superconductors

Daniel Steffensen

Abstract

Topological phases of matter have recently attracted a lot of attention in condensed matter physics, and especially the engineering of topological superconductors. The excitations of these highly desired materials are the exotic so-called Majorana fermions, which are their own anti-particles and are governed by non-Abelian exchange statistics. With all these properties, Majorana fermions have been proposed to be an essential building block for topological quantum computers.

Among the vast number of proposals for engineering topological superconductors, we will in this thesis aim to explore and study an alternative route, with the possibility of intrinsic topological superconductivity. Certain magnetic textures can give rise to an effective Rashba spin-orbit coupling, which has been proven to be a crucial ingredient in engineering topological superconductors. Additionally has the relatively new family of high- T_c superconducting materials, namely the Iron-Based superconductors, found to have a rich phase diagram with a broad variety of magnetic phases. Furthermore these materials have the possibility of magnetism coexisting with superconductivity. It might thus be possible to have an iron-based superconductor in a magnetic phase, which generates an effective spin-orbit coupling coexisting with superconductivity, resulting in a topological superconductor.

In this thesis we have performed a topological classification of the iron-based superconductors in the nine proposed magnetic phases, coexisting with a general spin-singlet superconducting order parameter. We found that certain magnetic textures indeed support the possibility of topological superconductivity. In the process of this classification, we also did a symmetry point group investigation of the material in question. Specifically we investigated the system in the incommensurate Double- \mathbf{Q} C_4 -symmetric Spin-Whirl Crystal (\bullet) magnetic phase, which has the possibility of harboring helical, or chiral Majorana edge modes, where the latter are obtained by applying an external magnetic field. Since a brute-force investigation of the possible topological phases of the iron-based superconductors is a formidable task, we did a simple bottom-up approach. We started with a simple Single-band model and extended it to two bands in order to capture nesting between distinct pockets at the Fermi surface. We found that the low energy Hamiltonian can give rise to single- \mathbf{Q} nested points, effectively described by a quasi-1D model, giving rise to Majorana flat bands. Whereas other points in the reduced Brillouin zone give rise to genuine double- \mathbf{Q} nested points, with heli-

cal/chiral Majorana edge modes. However, the predicted helical edge modes did not arise, but instead generated a supercurrent by tilting the Majorana flat bands. This disagreement might be an artifact of the low energy approximation, and needs to be investigated further.

Preface

The search of Majorana fermions started in high energy physics, where Ettore Majorana in 1937 showed the possibility for a real solution to the Dirac equation [1]. Eight decades later the search is still ongoing, but has now also moved to other branches of physics, namely condensed matter physics. The collective behavior of the high number of electrons in a solid can lead to emergent quasiparticles, which also can include Majorana fermions (MFs). Among the systems providing the possibility of harboring MFs, one finds the so-called topological superconductors (TSCs). MFs are topologically protected in such systems, and their robustness, together with their non-Abelian exchange statistics, render them as suitable building blocks for quantum computers.

There has been numerous proposals to engineer topological superconductors, since they not yet have been convincingly proven to be directly accessible in nature. In this thesis we will study an alternative route; topological superconductivity induced by magnetism in multi-band superconductors. Iron-Based Superconductors constitute a prominent candidate, that exhibits a rich phase diagram where magnetism and superconductivity coexist and compete. In presenting this work, we have structured the thesis as follows;

Chapter 1 A brief introduction to topological phases, more specifically topological superconductors, will be given, followed by a discussion of the possible types of Majorana modes in topological systems in one and two dimensions. Additionally we also discuss general symmetry transformations, and the scheme of topological symmetry classification.

Chapter 2 We shortly introduce the iron-based superconductors that, by their rich phase diagram, could be prominent candidates for a topological superconductor. To put further emphasis on this, we formulate a general Hamiltonian for such a system, and topological classify the system in the different proposed magnetic phases coexisting with superconductivity. We also perform an extensive symmetry point group analysis.

Chapter 3 This chapter commences a bottom-up case study of a superconductor in one of the relevant magnetic phases classified in Chap.2. We start in 1D with a one-band model, and study how the addition of an extra band modifies our results.

Chapter 4 To obtain further insight of the possible topological phases induced by magnetism, we go one step up in the bottom-up approach, and study a two- and one-band model in 2D. The Hamiltonian of these systems supports Majorana

flat bands, but also the possibility of harboring chiral/helical Majorana modes, depending on the symmetry class.

Chapter 5 Conclusion and outlook.

Lastly I would like to thank my supervisor Brian M. Andersen for making this project possible, and for introducing me to the world of research. A special thanks to Morten H. Christensen and Daniel D. Scherer for invaluable discussions during this project, and in general thanks to the Condensed Matter Theory group at the Niels Bohr Institute for providing a good everyday mood, and friendly environment. Also a thanks to Daniel Mendler for providing the code used to generate the figures in Fig.1.5.(a). Last, but not least; I am grateful for the never ending help from my co-supervisor Panagiotis Kotetes. Thank you for always being patience during my long and incoherent questions, and for always lending a helping hand. I owe you a tub of gin. Also thanks to Club Mate for holding me awake.

Contents

1	Introduction to Topological Superconductivity	1
1.1	Topological Superconductivity	2
1.2	Topological Superconductivity Induced by Magnetism	4
1.3	Topological Classification	7
1.4	Symmetry Transformations	8
1.5	Emergent Topological Protected Edge States	11
1.6	Topological Invariants	12
2	Topological Magnetic Iron-Based Superconductors	17
2.1	General Hamiltonian for Magnetic Iron-Based Superconductors	20
2.2	Bogoliubov-de Gennes Formalism	24
2.3	Topological Classification of Iron-Based Superconductors	29
2.4	Point Group Symmetry for the FeSCs	33
3	Topological Phases in 1D Magnetic Superconductors	41
3.1	Single-Band Model	42
3.2	Two-Band Model	49
4	Topological Phases of 2D Magnetic Superconductors	57
4.1	Quasi-1D Single-Band Model	57
4.2	Quasi-1D Two-Band Model	62
4.3	2D Single-Band Model	66
5	Conclusions and Outlook	75
A	SU(N) Generators	81
B	Mean-Field Decoupling Approach	83
C	Topological Classification of FeSCs	89
D	Matrix Representation of C_{4v} Elements	95

Chapter 1

Introduction to Topological Superconductivity

Phases of matter have always been an interesting and intriguing topic in modern physics. The familiar solid, liquid and gas phases are accompanied by more exotic phases when quantum phenomena become important, which leads to charge density waves, Bose-Einstein condensates, spin density waves and superconductivity, just to name a few. The different phases can be reached through varying external parameters; pressure, doping, temperature *etc.*, and are usually caused by the synergy of the tremendously large number of degrees of freedom in the system in question. The underlying principle in defining phase transitions is symmetry breaking, *e.g.* a paramagnet has spin rotation symmetry, unlike the ordered ferromagnetic phase. Tied to symmetry breaking there is an order parameter (OP) that can be used in the phenomenological Ginzburg-Landau theory. It is important to state that an OP is not necessarily obvious, and it can be a challenging task to determine it, however, once determined it can be physically measured and experimentally verified. Along side the measurable OP, the newly established ground state is also characterized by a set of excitations referred to as quasiparticles.

In recent decades topological phases have been attracting attention in the different communities of physics. In mathematics, topology is the study of spaces, and provides a way to classify objects that are not connected by continuous deformations. The typical example is a coffee mug that can be continuously deformed into a doughnut, but not a coffee mug with two handles. The two mugs are thus topologically inequivalent. To distinguish the two, one can define a topological invariant (index) that describes the global features of the space, *e.g.* the number of handles on the cup. The topological phases in physics are named so, since no local OP can be defined, but rather a global one, a topological invariant. This indicates that distinct physical systems, like the coffee mug and doughnut, can be topologically equivalent. Note lastly that the topological invariant can be connected to measurable quantities, such as the Hall conductivity in the quantum Hall effect, but a generalization to Ginzburg-Landau theory is not straightforward.

To name a few well-established examples of systems with topological non-trivial phases we have: the quantum Hall effect [2], quantum spin Hall effect [3] and Haldane's Chern insulator [4]. Where the former and the latter constitute physically distinct systems, but

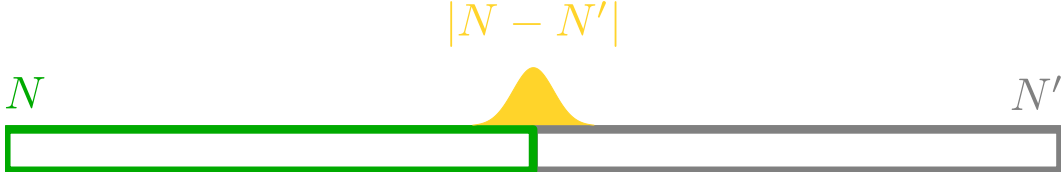


Figure 1.1: Illustration of the bulk-edge correspondence, where two bulk materials, with the invariants N and N' respectively, lead to $|N - N'|$ topological protected states located at their interface.

topologically equivalent phases. In analogy to the emergent single-particle and collective excitations for the regular phases of matter discussed in the first paragraph, the topological phases can also have new quasiparticle excitations. The nature of these excitations turns out to be very unconventional and exotic. A common feature for the new exotic states is that they are topologically protected due to the bulk-edge correspondence, stating that: At the interface of two systems, with respectively topological invariants N and N' , a number of $|N - N'|$ topologically protected excitations will arise in the vicinity of the interface [5], as shown in Fig. 1.1. The topological states are thus robust against any deformations and impurities, as long the topological indices remain and can be defined.

A physical intuition regarding the robustness of the topological states is that they only carry half the degrees of freedom compared to their bulk counterparts, and are therefore unaffected by local impurities that interact with the full degrees of freedom [6]. We stress here that the impurities need to be local, since a non-local impurity in principle could interact with the full degree of freedom. Take for instance the quantum Hall effect; here each edge has a single topological mode propagating in a single direction, often referred to as chiral modes. The unidirectional mode is therefore, by its topological nature, prohibited to move in the opposite direction, along which the chiral mode of the opposite edge is running. If the system has a local impurity at the edge, the protected mode simply circumvents it, and thus disperses without dissipation. Had the impurity instead interfered with the bulk topological index, then the mode would have lost its topological protection, and would thus have been scattered by the impurity.

1.1 Topological Superconductivity

The concept of obtaining topological edge modes with only half the degree of freedom compared to the bulk modes, has triggered the speculations about whether it is possible to split up the charge of an electron, and thereby make it robust against charge fluctuations and local charged impurities. An emergent particle with such qualities could be favorable for applications in many engineering problems. Mathematically splitting up an electron (hole) operator in two equal parts, is straightforwardly done by introducing two Majorana fermion (MF) operators, $\gamma_{\alpha,\beta}$, in the way:

$$c_i = \frac{\gamma_{i,\alpha} + i\gamma_{i,\beta}}{\sqrt{2}}, \quad c_i^\dagger = \frac{\gamma_{i,\alpha} - i\gamma_{i,\beta}}{\sqrt{2}}. \quad (1.1)$$

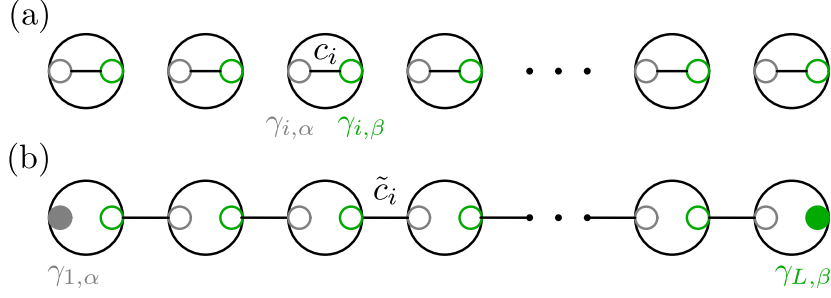


Figure 1.2: The Kitaev chain for a p -wave superconductor. (a) The fermionic operators c_i can be rewritten in terms of Majorana operators $\gamma_{i,\alpha}$. Here the big white circles represent electrons at the corresponding lattice sites. (b) In the limit for $\mu = 0$ and $\Delta = t$, the Hamiltonian can be diagonalized in terms of the operators \tilde{c}_i , constructed by pairing-up MF operators at neighboring sites, leaving two MFs localized at each end.

The MF operators fulfill $\{\gamma_\alpha, \gamma_\beta\} = \delta_{\alpha,\beta}$, $\gamma_\alpha^\dagger = \gamma_\alpha$ and $\gamma_\alpha^2 = 1/2$. Since the above only constitutes an alternative representation, one could argue that MFs always are accessible in condensed matter systems, however, since the pair of MFs tied to a single electron is localized at the exact same point in space, charge fluctuations/impurities will always interact with the full charge degree of freedom. This implies that it is desirable to separate a single electron into two MFs over a greater distance. By inverting Eq. 1.1 we find that a MF is made up of equal part electron and hole, and therefore is charge neutral:

$$\gamma_{i,\alpha} = \frac{c_i^\dagger + c_i}{\sqrt{2}}, \quad \gamma_{i,\beta} = i \frac{c_i^\dagger - c_i}{\sqrt{2}}. \quad (1.2)$$

Besides confirming the charge neutrality of the MFs, Eq. 1.2 also equips us with a clue of a possible type of systems that provide the possibility of supporting MFs, namely superconductors. A pairing potential, Δ , couples holes and electrons, as will be discussed in Sec. 2.2, and will give eigenstates consisting of linear combinations of holes and electrons

$$\gamma = \sum_{\mu\nu} (u_\mu c_\mu + v_\nu c_\nu^\dagger), \quad \gamma^\dagger = \sum_{\mu\nu} (u_\mu^* c_\mu^\dagger + v_\nu^* c_\nu) \quad (1.3)$$

where μ and ν are quantum numbers containing spin, orbital, crystal momentum *etc.* In order for the self-adjointed condition to be fulfilled we observe that $\mu = \nu$ and $u_\mu = v_\nu^*$. From the rules of adding up momenta, and the fact that the Cooper pairs are made up of spin-1/2 particles, we know the pairing either can be in a spin singlet or a triplet configuration. For a singlet configuration, with total spin of $S = 0$, we can set $\mu = \uparrow$ and $\nu = \downarrow$, ruling out a MF solution. Instead if the pairing is triplet, $S = 1$, we need to incorporate all spin indexes; $\mu = \{\uparrow, \downarrow\}$ and likewise for ν , which can indeed give rise to MF solutions, as seen from Eq. 1.3. Triplet pairing is therefore desired, such an example is the so-called p -wave superconductors, in order to get solutions of the MF type.

A MF solution does not necessarily imply spatially separated MFs, but rather that the quasiparticle excitations in the superconducting ground state are of that type. However, when the system resides in a topological non-trivial phase, we find a highly non-localized electron at

the boundaries of the system, *i.e.* two separated MFs. To make this statement transparent, let us consider a simple spinless 1D tight-binding Hamiltonian with p -wave superconductivity, as first proposed by A.Y. Kitaev [7]:

$$H = -\mu \sum_{i=1}^L c_i^\dagger c_i - \sum_{i=1}^{L-1} \left(t c_i^\dagger c_{i+1} - \Delta c_i c_{i+1} + \text{h.c.} \right), \quad (1.4)$$

where c_i annihilates an electron at site i . Reformulating the Hamiltonian in terms of MF operators, see Fig. 1.2.(a), we get the Hamiltonian

$$H = 2it \sum_{i=1}^{L-1} \gamma_{i,\beta} \gamma_{i+1,\alpha} \quad (1.5)$$

where we a priori have set $\mu = 0$ and $\Delta = t$. Already at this point we observe that the operators $\gamma_{1,\alpha}$ and $\gamma_{L,\beta}$ are missing from the summation in the Hamiltonian. Rewriting the Hamiltonian in the shifted fermionic operators \tilde{c}_i , which pair-up MFs at neighboring sites, diagonalizes the Hamiltonian;

$$\tilde{c}_i = \frac{\gamma_{i+1,\alpha} + i\gamma_{i,\beta}}{2} \quad \Rightarrow \quad H = -2t \sum_{i=1}^{N-1} \tilde{c}_i^\dagger \tilde{c}_i + \text{const.} \quad (1.6)$$

By considering Fig. 1.2.(b) it becomes evident that the solution leads to localized MFs at the ends of the chain, that can be combined into a single non-local zero energy electron

$$c_{\text{MF}} = \frac{\gamma_{1,\alpha} + i\gamma_{L,\beta}}{\sqrt{2}}. \quad (1.7)$$

We can thus confirm that topological edge states, with half an electron at each end, can be harbored in a p -wave superconductor. Since the protected states, as we will discuss later on, are linked to a topological invariant, these types of materials are referred to as topological superconductors. The MFs are highly interesting due to their non-Abelian exchange statistics, rendering them as suited building blocks for quantum computation [8].

1.2 Topological Superconductivity Induced by Magnetism

In the search of the highly coveted p -wave superconductors, and thereby the MFs, nature seems inadequate in supporting such materials. There has been candidates such as: the superfluid phases of ^3He [9], the spin-triplet superconductor Sr_2RuO_4 and in Bechgaard's salts [10], but they are all experimental inaccessible for implementing quantum computations. The community of condensed matter physics has therefore invested much time, and effort to achieve the desired pairing by alternative routes, counting examples as: MFs in carbon nanotubes [11], topological insulators in proximity to an s -wave superconductor [12], magnetic skyrmion textures [13], *etc.*

A well-established procedure for achieving topological superconductivity is through a hybrid nanostructure, consisting of a semiconducting wire with large Rashba spin-orbit coupling (SOC), in proximity to a bulk s -wave superconductor and an external magnetic field [14,15],

see Fig. 1.3.(d). The Bogoliubov-de Gennes (BdG) Hamiltonian of such a system will be of the form

$$H(k) = \frac{1}{2} \sum_k \widehat{\Psi}_k^\dagger \left[\tau_z \left(\frac{\hbar^2 k^2}{2m} - \mu + \sigma_x v \hbar k \right) + B \sigma_z + \Delta \tau_x \right] \widehat{\Psi}_k \quad (1.8)$$

with the spinor $\widehat{\Psi}_k = (\psi_{k\uparrow}, \psi_{k\downarrow}, \psi_{-k\downarrow}^\dagger, -\psi_{-k\uparrow}^\dagger)^\top$, where $\boldsymbol{\sigma} = (\sigma_x, \sigma_y, \sigma_z)$ and $\boldsymbol{\tau} = (\tau_x, \tau_y, \tau_z)$ are Pauli matrices acting on spin and Nambu space respectively, see App. A. Note that we for brevity have omitted all the identity matrices, and that the product between two matrices, belonging to different spaces, should be understood as a Kronecker product, *i.e.* $\tau_j \sigma_i \equiv \tau_j \otimes \sigma_i$. The parameters in the Hamiltonian v , B and Δ are the SOC coupling, magnetic field and superconducting gap respectively. At first glance this Hamiltonian seems like an ordinary s -wave superconductor, however, the SOC is an important ingredient and will generate an effective p -wave pairing.

Consider at first the spectrum of the Hamiltonian with $v = \Delta = 0$, but $B \neq 0$ as in Fig. 1.3.(a). The non-zero magnetic field lifts the Kramers degeneracy, producing a spinless regime when the chemical potential is in the magnetic gap. However, the spinless regime is solely governed by one spin projection, making an effective triplet pairing inaccessible, since the superconducting gap in Eq. 1.8 only pairs up electrons with opposite spin projection. If we instead turn on the SOC, $v \neq 0$, and set $B = 0$, the two spin bands get shifted depending on their spin projection along the spin x -axis, as shown in Fig. 1.3.(b). Again lifting the spin degeneracy with a magnetic field, we achieve an effective momentum dependent spinless regime, when the chemical potential is in the magnetic gap, Fig. 1.3.(c). Due to the momentum dependence of the spin, the singlet superconducting gap can now pair up electrons at opposite momenta and spin in this lower band, thus creating an effective p -wave pairing [16]. Lastly, one can make a direct mapping to the Kitaev chain in the limit of large magnetic field, $B/v \gg 1$ and $B/\Delta \gg 1$, by an effective projection onto the lower band [17].

It seems that the SOC is a necessary ingredient in engineering TSCs. Since this type of coupling originates from the broken inversion due to the substrate, it is usually material determined, and not easily controlled. This led researchers to find yet another alternative route to engineer TSCs, via an artificial SOC, that then in return could lead to an effective p -wave superconductor. One proposal is to have a magnetic spiral texture in vicinity to a semiconducting wire, which would give rise to an effective SOC [18], as displayed in Fig. 1.3.(d). To illustrate this, let us consider the case of a simple 1D wire in a symmetric spiral magnetic field;

$$\begin{aligned} H &= \int dr \widehat{\psi}^\dagger(r) \left[\frac{\hat{p}^2}{2m} - \mu + M(\cos(Qr)\sigma_z + \sin(Qr)\sigma_y) \right] \widehat{\psi}(r) \\ &= \int dr \widehat{\psi}^\dagger(r) e^{-iQr\sigma_x/2} \left[e^{iQr\sigma_x/2} \frac{\hat{p}^2}{2m} e^{-iQr\sigma_x/2} - \mu + M\sigma_z \right] e^{iQr\sigma_x/2} \widehat{\psi}(r), \end{aligned} \quad (1.9)$$

with the spinor $\widehat{\psi}(r) = (\psi_\uparrow(r), \psi_\downarrow(r))^\top$. In the second equality we simply performed a unitary transformation with $\widehat{U} = \exp(-iQr\sigma_x/2)$, to simplify the expression. The single particle

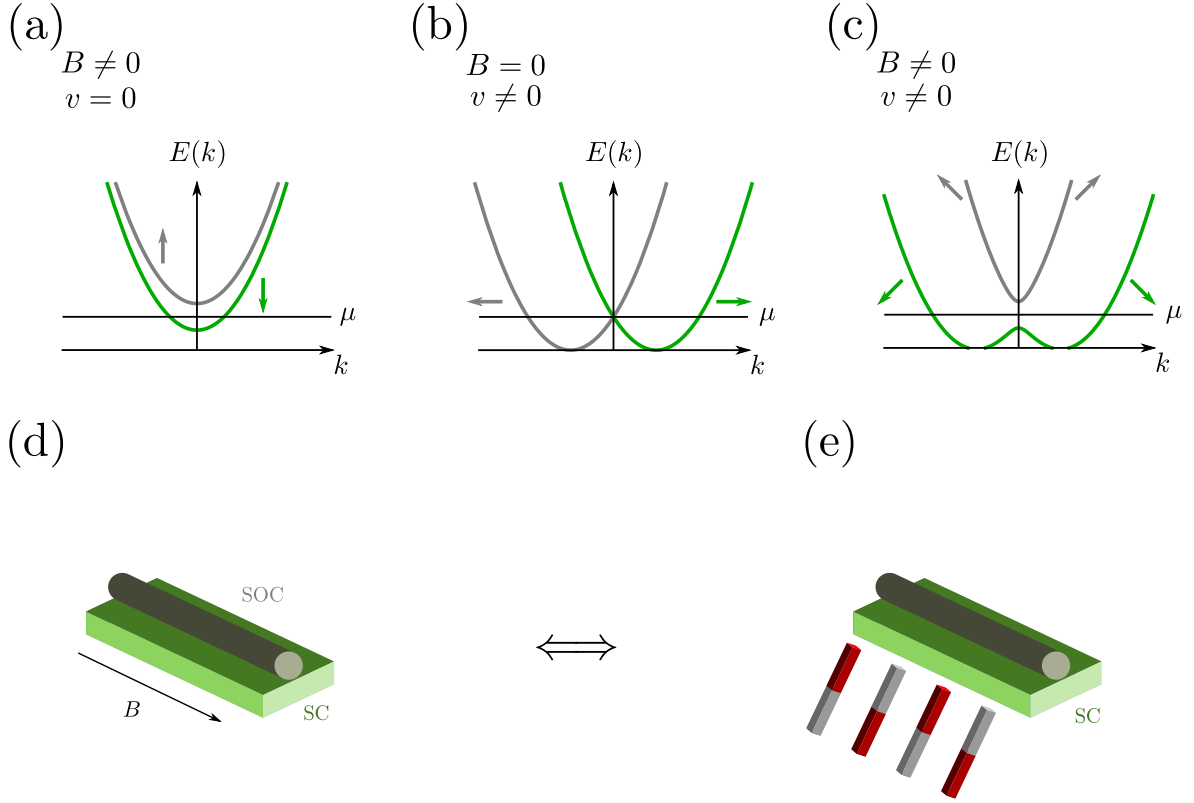


Figure 1.3: Engineering topological superconductivity. (a)-(c) Show the spectrum for Eq.1.8. in different scenarios. The small arrows represent spin projection for the given band. (d) Platform for engineering TSCs, with a nanowire deposited on a bulk s -wave superconductor and an external magnetic field. The nanowire sees a Rashba SOC, effectively generating a p -wave superconductor. (e) Equivalently a nanowire can be deposited on a bulk s -wave superconductor in the vicinity of a spatially varying magnetic field, effectively generating a SOC. The arrow connecting the two figures indicates that the two can be mapped to one another through a unitary transformation, as see in Eq. 1.9.

Symmetry				Spatial Dimensionality							
AZ	Θ^2	Ξ^2	Π^2	1	2	3	4	5	6	7	8
A	0	0	0	0	\mathbb{Z}	0	\mathbb{Z}	0	\mathbb{Z}	0	\mathbb{Z}
AIII	0	0	1	\mathbb{Z}	0	\mathbb{Z}	0	\mathbb{Z}	0	\mathbb{Z}	0
AI	1	0	0	0	0	0	\mathbb{Z}	0	\mathbb{Z}_2	\mathbb{Z}_2	\mathbb{Z}
BDI	1	1	1	\mathbb{Z}	0	0	0	\mathbb{Z}	0	\mathbb{Z}_2	\mathbb{Z}_2
D	0	1	0	\mathbb{Z}_2	\mathbb{Z}	0	0	0	\mathbb{Z}	0	\mathbb{Z}_2
DIII	-1	1	1	\mathbb{Z}_2	\mathbb{Z}_2	\mathbb{Z}	0	0	0	\mathbb{Z}	0
AII	-1	0	0	0	\mathbb{Z}_2	\mathbb{Z}_2	\mathbb{Z}	0	0	0	\mathbb{Z}
CII	-1	-1	1	\mathbb{Z}	0	\mathbb{Z}_2	\mathbb{Z}_2	\mathbb{Z}	0	0	0
C	0	-1	0	0	\mathbb{Z}	0	\mathbb{Z}_2	\mathbb{Z}_2	\mathbb{Z}	0	0
CI	1	-1	1	0	0	\mathbb{Z}	0	\mathbb{Z}_2	\mathbb{Z}_2	\mathbb{Z}	0

Table 1.1: The topological periodic table, from [19], shows the 10 symmetry classes. A given symmetry class is determined by the behavior of the symmetries in Eqs.1.11. upon squaring. In addition, the table shows the types of the possible topological invariants ($\mathbb{Z}, \mathbb{Z}_2, 0$) that one can define for each class in a given dimension. Note that the spatial dimension is shown up to eight, since one can employ Bott-Periodicity for higher dimensions.

Hamiltonian, after a Fourier transformation, ends up to obtain the form

$$\hat{\mathcal{H}}(k) = \frac{\hbar^2 k^2}{2m} + \underbrace{\left(\frac{\hbar^2 Q^2}{8m} - \mu \right)}_{\tilde{\mu}} - \frac{\hbar^2 Q}{2m} k \sigma_x + M \sigma_z, \quad (1.10)$$

where we arrive at a similar single-particle Hamiltonian as the kernel of Eq. 1.8, when s -wave pairing is included. Not only does this allow for a tunable effective SOC through the wave vector of the magnetic field Q , but also opens up new routes for engineering topological superconductivity.

1.3 Topological Classification

As discussed above, physically distinct systems can give rise to the same topological characteristics, so one could in principle search elsewhere for the desired TSC. To narrow down the vast search, a more systematic procedure for identifying topological phases were carried out [20–22]. This was done by an exhaustive classification of random matrices, and the classification is only applicable for non-interacting systems, which can be represented as matrices. The classification scheme is based on three discrete symmetries: the anti-unitary generalized time-reversal Θ , the anti-unitary generalized charge-conjugation Ξ and the unitary Π chiral

symmetry. The three discrete symmetries, if they are present, fulfill the following:

$$\Theta^\dagger \widehat{\mathcal{H}}(\mathbf{k}) \Theta = +\widehat{\mathcal{H}}(\mathbf{k}) \quad [\widehat{\mathcal{H}}(\mathbf{k}), \Theta] = 0, \quad (1.11a)$$

$$\Xi^\dagger \widehat{\mathcal{H}}(\mathbf{k}) \Xi = -\widehat{\mathcal{H}}(\mathbf{k}) \quad \Rightarrow \quad \{\widehat{\mathcal{H}}(\mathbf{k}), \Xi\} = 0, \quad (1.11b)$$

$$\Pi^\dagger \widehat{\mathcal{H}}(\mathbf{k}) \Pi = -\widehat{\mathcal{H}}(\mathbf{k}) \quad \{\widehat{\mathcal{H}}(\mathbf{k}), \Pi\} = 0. \quad (1.11c)$$

If both Θ and Ξ are present, it is possible to construct the unitary operator $\Theta\Xi = \widehat{U}_\Theta \mathcal{K} \widehat{U}_\Xi \mathcal{K} = \widehat{U}_\Theta \widehat{U}_\Xi^* = \Pi$, where it is clear from Eqs. 1.11.(a-b) that this operator anti-commutes with the Hamiltonian, hence leading to the so-called chiral symmetry. There is, however, the possibility of chiral symmetry even in the absence of Θ and Ξ , see class AIII in Table. 1.1. The three symmetries all square to $\pm\mathbb{1}$, and can be divided into 10 symmetry classes, shown in Table. 1.1. Each of these classes are labeled with a set of numbers, \mathbb{Z} , \mathbb{Z}_2 and 0, depending on the specific spatial dimensions. These sets indicate the possible type of topological invariants that can be defined in the given class and dimension, and reveal which systems are interesting from a topological perspective.

If the Hamiltonian in question is not a random matrix, *i.e.* it has some unitary symmetry $[\widehat{\mathcal{O}}, \widehat{\mathcal{H}}(\mathbf{k})] = 0$, it is possible to block diagonalize, and classify each block $\bigoplus_i \widehat{\mathcal{H}}^i(\mathbf{k})$. Such a unitary symmetry can originate from the relevant point group of the Hamiltonian \mathcal{G} , or a translation in real space [23]. As already stated, this classification only holds for non-interacting systems, but there has recently been an increasing interest in topological classification of interacting systems, giving rise to new phases [24].

1.4 Symmetry Transformations

We will in this section formulate how a general symmetry operator G effects the system in question, before proceeding with a topological classification of the prototypical Hamiltonian in Eq. 1.8 extended to two dimensions. The general formulation will be followed by examples of symmetries that are closely related to the three in Eqs.1.11.

Consider at first the abstract symmetry operator G in a Hilbert space spanned by the set $\{|n\rangle\}$, where G transforms the basis in the way

$$G |n\rangle = |m\rangle. \quad (1.12)$$

How is an arbitrary operator U in the new basis $\{|m\rangle\}$ related to the representation in the old basis? This can be seen through the relation for the matrix elements

$$\langle m|U|m'\rangle = \sum_{n'' n'''} \langle n|G^\dagger|n''\rangle \langle n''|U|n'''\rangle \langle n'''|G|n'\rangle. \quad (1.13)$$

The above indicates that in the matrix representation a symmetry acts as

$$U' = G^\dagger U G \doteq d^\dagger(G) \widehat{U} d(G) \quad (1.14)$$

where the sign \doteq stands for "represented as" [25], and where \widehat{U} and $d(G)$ are matrices defined in the old basis $\{|n\rangle\}$. Note that the matrix representation for the symmetry operation here is denoted by $d(G)$ as it is customary in group theoretical approaches [26,27], and not by a caret

as for the general operator U . The systems under consideration have translational symmetry, making it convenient to formulate the Hamiltonian in Bloch space. Redoing the formulation in Eq. 1.13, but now with the quantum number n replaced by a crystal momentum \mathbf{k} , and making the operator U diagonal in the $|\mathbf{k}\rangle$ basis, the transformation can be represented as

$$G^\dagger U G \doteq d^\dagger(G) \widehat{U}(G\mathbf{k}) d(G). \quad (1.15)$$

The action on the crystal momentum is not captured by a matrix representation, but by a transformation of the \mathbf{k} vector. In Sec. 1.3 we referred to antiunitary symmetry operators, which do not follow the usual unitary condition, but instead [25]

$$\langle n' | G^{-1} G | n \rangle = \langle m' | m \rangle = \langle n' | n \rangle^* = \langle n | n' \rangle \neq \langle n' | n \rangle. \quad (1.16)$$

Such an operator will have the general form $G = U_G \mathcal{K}$, where U_G is an unitary operator, and \mathcal{K} is complex conjugation. We will define complex conjugation to reverse the crystal momentum of the system $\mathcal{K}\mathbf{k} = -\mathbf{k}$, which we will address in Sec.2.1. Let us illustrate the discussed symmetry transformation and antiunitary operators with the following examples.

Inversion

Inversion is the operation that inverts the spatial coordinates of the system;

$$\mathcal{I}^\dagger \hat{\mathbf{r}} \mathcal{I} = -\hat{\mathbf{r}}, \quad \mathcal{I}^\dagger \hat{\mathbf{p}} \mathcal{I} = -\hat{\mathbf{p}}, \quad \mathcal{I}^\dagger \hat{\mathbf{S}} \mathcal{I} = \hat{\mathbf{S}}, \quad (1.17)$$

with $\hat{\mathbf{r}}$, $\hat{\mathbf{p}}$ and $\hat{\mathbf{S}}$ being the position, momentum and spin angular operator respectively. If we consider a general basis state with the following quantum numbers $|\mathbf{k}, \mu, \sigma\rangle$, where μ is orbital/band index and σ is spin projection, the inversion operation transforms the basis as

$$\mathcal{I} |\mathbf{k}, \mu, \sigma\rangle = |-\mathbf{k}, \mathcal{I}\mu, \sigma\rangle. \quad (1.18)$$

The transformation of μ depends on its physical origin. If μ is an orbital index, it will transform as the eigenfunctions of the hydrogen atom

$$\mathcal{I} R_{nl}(r) Y_l^m(\theta, \phi) = (-1)^l R_{nl}(r) Y_l^m(\theta, \phi), \quad (1.19)$$

as it is the case in tight-binding models (discussed in Sec. 2.1). Equivalently, one could simply consider the nomenclature of the orbitals in question, since they have been named after representative functions, *e.g.* the p_x orbital transforms as the function $f(x) = x$. Had μ instead been a band index, we would expect it to be invariant under inversion. This is indeed true if the system belongs to a symmetry point group with an inversion element, since $\widehat{\mathcal{H}}_0(\mathbf{k})$ has to transform with respect to the trivial irreducible representation, see Sec. 2.4 for details. Here $\widehat{\mathcal{H}}_0(\mathbf{k})$ is the free dispersion of the Hamiltonian.

Charge Conjugation

Charge conjugation, \mathcal{C} , is the operation that transforms a particle into its charge conjugated counterpart. In the BdG formalism (which we will discuss in Sec.2.2) this is equivalent to transforming an electron into a hole, with reversed crystal momentum. By construction the

BdG Hamiltonian has the following relation between the electron and the hole operator (see Eq. 2.21):

$$\widehat{\Psi}_{\mathbf{k}}^\dagger = \widehat{\Psi}_{-\mathbf{k}}^\tau \widehat{U}^\dagger \quad \Rightarrow \quad \widehat{\Psi}_{-\mathbf{k}}^\tau \widehat{U}^\dagger = \widehat{\Psi}_{\mathbf{k}}^\dagger \mathcal{K}^\dagger \widehat{U}^\dagger = \widehat{\Psi}_{\mathbf{k}}^\dagger d^\dagger(\mathcal{C}). \quad (1.20)$$

Where we have defined the matrix representation of charge conjugation to be $d(\mathcal{C}) = \widehat{U}\mathcal{K}$, and used that $\widehat{\Psi}_{\mathbf{k}}^\dagger \mathcal{K}^\dagger = \widehat{\Psi}_{-\mathbf{k}}^\tau$. By exploiting Eq. 1.15 we obtain the transformed Hamiltonian

$$\widehat{\mathcal{H}}'(\mathbf{k}) = \mathcal{C}^\dagger \widehat{\mathcal{H}}(\mathbf{k}) \mathcal{C} \doteq d^\dagger(\mathcal{C}) \widehat{\mathcal{H}}(\mathbf{k}) d(\mathcal{C}) = \widehat{U}^\dagger \widehat{\mathcal{H}}^\tau(-\mathbf{k}) \widehat{U}. \quad (1.21)$$

For a particle hole symmetric Hamiltonian, the latter equality will give

$$\widehat{U}^\dagger \widehat{\mathcal{H}}^\tau(-\mathbf{k}) \widehat{U} = -\widehat{\mathcal{H}}(\mathbf{k}) \quad \Rightarrow \quad \{\widehat{\mathcal{H}}(\mathbf{k}), d(\mathcal{C})\} = 0, \quad (1.22)$$

where we see that charge conjugation \mathcal{C} falls into the class of generalized charge conjugation operators in the topological classification, see Eq.1.11b.

Translation and Rotation

Translations and rotations are generated by their conjugated variables, *i.e.* translations are generated by linear momentum, whereas angular momentum generates rotations. Translation operation by a along the unit vector $\bar{\mathbf{n}}$ must act on a real space ket as [25]

$$t_a^{\bar{\mathbf{n}}} |\mathbf{r}\rangle = |\mathbf{r} + a\bar{\mathbf{n}}\rangle = e^{-ia\bar{\mathbf{n}}\cdot\hat{\mathbf{p}}/\hbar} |\mathbf{r}\rangle. \quad (1.23)$$

Similarly is the rotation operation defined as

$$R_\phi^{\bar{\mathbf{n}}} = e^{-i\phi\bar{\mathbf{n}}\cdot\hat{\mathbf{J}}/\hbar}, \quad (1.24)$$

with $\hat{\mathbf{J}} = \hat{\mathbf{L}} + \hat{\mathbf{S}}$ being the total angular momentum operator.

Time Reversal

Time reversal is, as the name states, the operation that reverses the time coordinate, $\mathcal{T}t = -t$. The operation is antiunitary, $\mathcal{T} \doteq d(U_{\mathcal{T}})\mathcal{K}$, and must transform the relevant operators as follows

$$\mathcal{T}^\dagger \hat{\mathbf{r}} \mathcal{T} = \hat{\mathbf{r}}, \quad \mathcal{T}^\dagger \hat{\mathbf{p}} \mathcal{T} = -\hat{\mathbf{p}}, \quad \mathcal{T}^\dagger \hat{\mathbf{S}} \mathcal{T} = -\hat{\mathbf{S}}. \quad (1.25)$$

We first note that the momentum operator in real space can be represented as $\hat{\mathbf{p}} = -i\hbar\nabla$, which indeed is odd under the antiunitary part of the operator. Next, applying the usual representation of the spin angular momentum operator, with \hat{S}_y imaginary, it is clear that one needs to do a rotation of π about the \hat{S}_y -axis in order to meet Eq. 1.25. The general matrix representation becomes

$$\mathcal{T} \doteq \widehat{U}_{\mathcal{T}} \mathcal{K} = e^{-i\hat{S}_y\pi/\hbar} \mathcal{K}, \quad (1.26)$$

where we have used the rotation operator defined in Eq. 1.24. If a system has time-reversal symmetry it fulfills the following relation

$$\mathcal{T}^\dagger \widehat{\mathcal{H}}(\mathbf{k}) \mathcal{T} = \widehat{\mathcal{H}}(\mathbf{k}) \quad \Rightarrow \quad [\mathcal{T}, \widehat{\mathcal{H}}(\mathbf{k})] = 0. \quad (1.27)$$

Time-reversal belongs therefore to the class of generalized time-reversal operators in Eq.1.11a.

1.5 Emergent Topological Protected Edge States

After having established the theory of symmetry transformations, we can now approach the topological classification of the prototypical Hamiltonian in Eq.1.8. Not only do the three discrete symmetries in Eqs. 1.11 help in the search for topological non-trivial systems, but also tell us something about the physical emergent edge states. To illustrate this, we will consider the aforementioned Hamiltonian used for engineering TSC, Eq. 1.8-1.9, and extend it to two dimensions in the following fashion:

$$\hat{\mathcal{H}}(\mathbf{k}) = \tau_z \left(\frac{\hbar^2 \mathbf{k}^2}{2m} - \mu \right) + \tau_z (\alpha \hbar k_y \sigma_x - \beta \hbar k_x \sigma_y) + B \sigma_z + \Delta \tau_x. \quad (1.28)$$

In the following, we will discuss four sub-cases of the above Hamiltonian, all with $\Xi^2 = \mathbb{1}$ indicating that the emergent topological protected states are of the Majorana type. In this classification note that $\mathcal{K}\mathbf{k} = -\mathbf{k}$, as will be discussed in the upcoming chapter. The distinct topological states for the four sub-cases are illustrated in Fig. 1.4.

$\alpha \neq 0, \beta = 0$ and $k_x = 0$

This case is exactly the prototypical Hamiltonian discussed above, belonging to the class BDI with the symmetries

$$\Theta^2 = (\sigma_z \mathcal{K})^2 = +\mathbb{1}, \quad \Xi^2 = (\tau_y \sigma_y \mathcal{K})^2 = +\mathbb{1}, \quad \Pi^2 = (\tau_y \sigma_x)^2 = +\mathbb{1}. \quad (1.29)$$

In this symmetry class a \mathbb{Z} invariant can be defined, which must mean that a number of \mathbb{Z} MFs are located at the edge of the system (assuming the system edge to be in contact with a topologically trivial material, *e.g.* the vacuum). See Fig. 1.4.(a) for the real space wave functions of the edges, as derived in [5].

$\alpha \neq 0, \beta \neq 0$ and $k_x \neq 0$

The corresponding two-dimensional version of the prototypical Hamiltonian Eq. 1.8 breaks both chiral and generalized time-reversal symmetry, due to the additional component of the Rashba SOC. The system resides in the class D, with the symmetries

$$\Theta^2 = 0, \quad \Xi^2 = (\tau_y \sigma_y \mathcal{K})^2 = +\mathbb{1}, \quad \Pi^2 = 0. \quad (1.30)$$

Table. 1.1 tell us that a \mathbb{Z} invariant can be defined for this system, giving rise to a number of \mathbb{Z} modes per edge. Note furthermore that chiral symmetry has been broken, which gives rise to chiral edge modes, similar to the quantum Hall effect. Again see Fig. 1.4.(b) and [5] for the real space wave function and derivation, respectively.

$\alpha \neq 0, \beta \neq 0, k_x \neq 0$ and $B = 0$

If we consider the system above, but now turn off the magnetic field B , the system obtains an enhanced symmetry, namely

$$\Theta^2 = (\sigma_y \mathcal{K})^2 = -\mathbb{1}, \quad \Xi^2 = (\tau_y \sigma_y \mathcal{K})^2 = +\mathbb{1}, \quad \Pi^2 = \tau_y^2 = +\mathbb{1}. \quad (1.31)$$

This render the system in the class DIII, with the possibility of a \mathbb{Z}_2 invariant in 2D. A generalized time-reversal squaring to $\Theta^2 = -1$ tell us that the emergent modes will come in Kramers pairs, similar to the physical time-reversal operator \mathcal{T} for spin-1/2 particles. The emergent states are therefore helical similar to the quantum spin Hall states, see again Fig.1.4.(c). This sub-case is an example of a Hamiltonian with the right symmetry to harbor MFs, however, when calculating the invariant one finds that it always is zero. For a discussion of this see Ref. [28].

$\alpha \neq 0, \beta = 0$ and $k_x \neq 0$

Again considering the two-dimensional prototypical Hamiltonian, but now turning off SOC along k_x , we find the symmetries

$$\Theta^2 = (\sigma_z \mathcal{K})^2 = +\mathbf{1}, \quad \Xi^2 = (\tau_y \sigma_y \mathcal{K})^2 = +\mathbf{1}, \quad \Pi^2 = (\tau_y \sigma_x)^2 = +\mathbf{1}. \quad (1.32)$$

Clearly this 2D system resides in the class BDI, where no topological invariant in the given dimensionality can be defined. One can consider the system as a stack of 1D BDI chains, allowing us to define a k_x -dependent topological invariant, since each of these can harbor MFs. The resulting invariant is often referred to as a *weak* invariant, since the states are not robust against the breaking of translational invariance along the x -direction. The emergent modes are termed Majorana flat bands (MFBs), due to their flat dispersions along k_x , as will become clearer in later chapters. The real space wave functions, due to the flat dispersions, are simply located at the edges, see Fig. 1.4.(d).

1.6 Topological Invariants

We have so far only mentioned the topological invariants as some abstract features of a topological system, but we will now come up with concrete examples of how to calculate them, and how to relate them to the bulk-edge correspondence. In topological band theory, two sets of bands are said to be topologically equivalent if their energy spectra can be continuously deformed into one another without closing a gap in the bulk. Once again think about the analogy of the mug and the doughnut, the two mugs cannot be continuously connected without gluing/cutting the space. We thus need to define a number that stays invariant under any deformations, except to those who lead to closings of the bulk gap. At the gap closing points the invariant is not defined while it is allowed to change across such a gap closing. We can also make the connection to the quantum Hall effect, where it has been shown, that the Hall conductance is proportional to an integer C , the so-called Chern number, defined as

$$C = \int \frac{d\mathbf{k}}{2\pi} F_{xy}(\mathbf{k}). \quad (1.33)$$

Here $F_{xy}(\mathbf{k})$ is the Berry curvature, defined as

$$F_{xy}(\mathbf{k}) = \partial_{k_x} A_y(\mathbf{k}) - \partial_{k_y} A_x(\mathbf{k}), \quad A_\mu(\mathbf{k}) = i \sum_{\nu} \langle \nu \mathbf{k} | \frac{\partial}{\partial k_\mu} | \nu \mathbf{k} \rangle, \quad (1.34)$$

with A_μ being the Berry potential, and $|\nu \mathbf{k}\rangle$ being the filled Bloch states. The use and definition of the Berry curvature/potential were established to show that the states of a

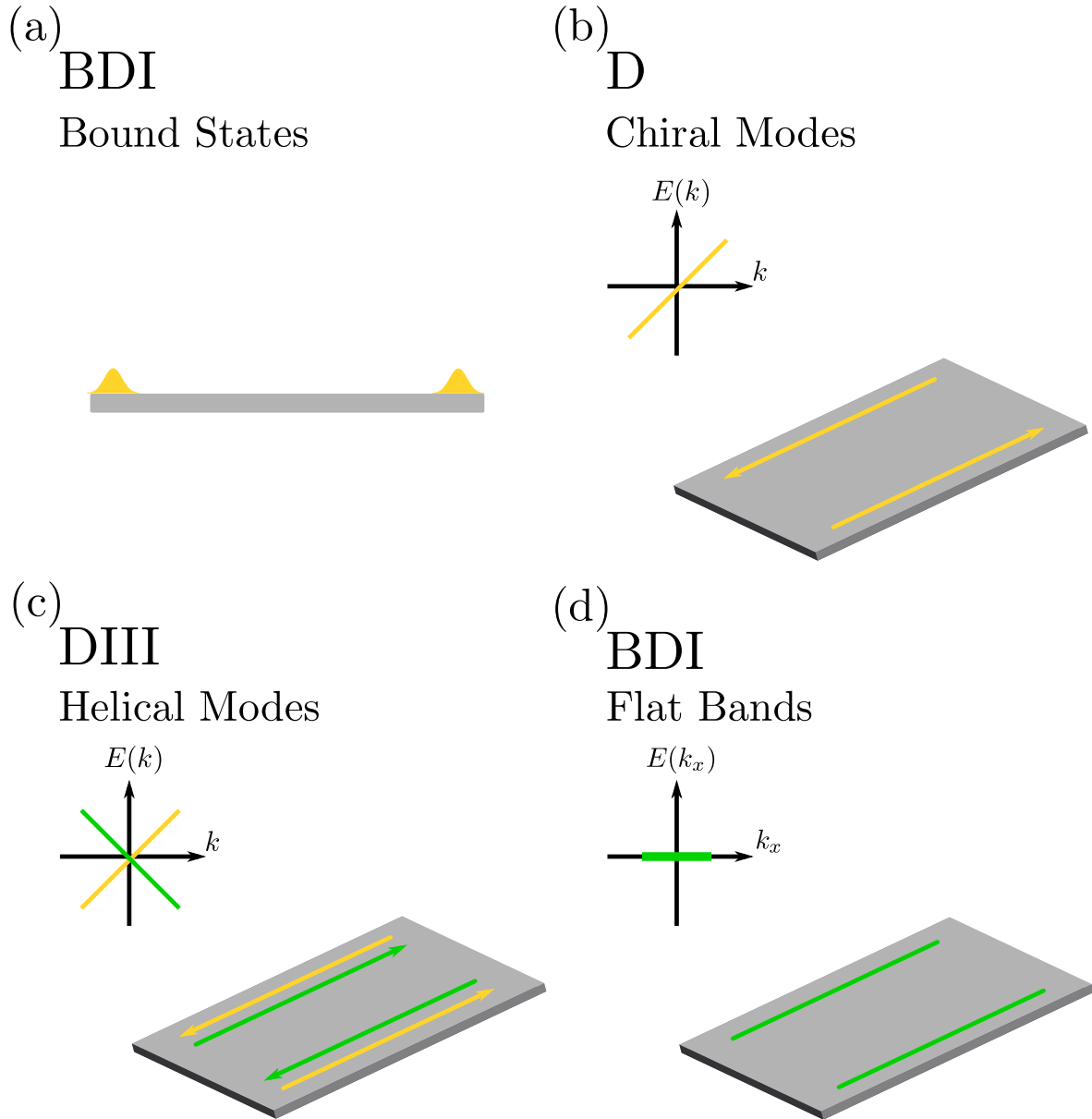


Figure 1.4: Emergent topologically protected edge states of the two-dimensional prototypical Hamiltonian of Eq. 1.8 for different sub-cases. In Figs. (b)-(d) we show the dispersions of the Majorana modes residing at one of the two edges. All states are of the Majorana type since $\Xi^2 = +1$.

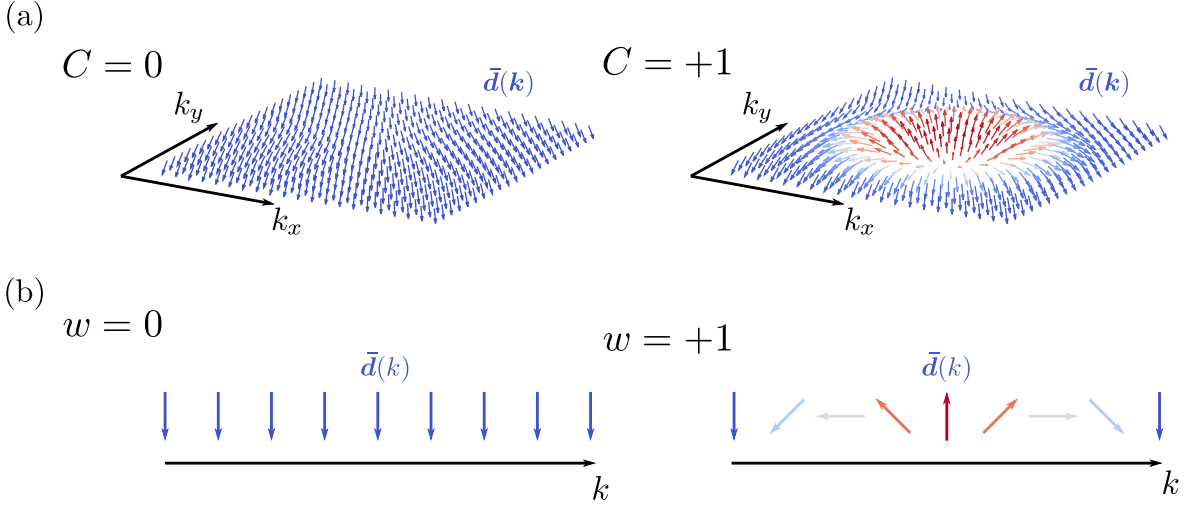


Figure 1.5: (a) Profile of the parameterizing vector $\bar{\mathbf{d}}(\mathbf{k})$ in the case of a trivial phase with $C = 0$, and in a topological non-trivial phase with $C = 1$. In the latter the $\bar{\mathbf{d}}(\mathbf{k})$ wraps around the S^2 sphere when \mathbf{k} is swept across the first BZ. (b) Winding of the parameterizing vector in 1D for a topologically trivial phase with $w = 0$, and a topologically non-trivial phase with $w = +1$. It is evident that for $w = +1$, the vector winds the S^1 sphere once.

system picks up a phase, besides the usual dynamic one, when a closed loop is traced out in parameter space [25], the so-called Berry/geometrical phase. The closed loop for Bloch electrons is exactly the well-known Brillouin zone (BZ), which in 2D takes the form of a torus T^2 . To obtain a better intuition about the Chern number, let us consider a simple two-level Hamiltonian

$$\hat{\mathcal{H}}(\mathbf{k}) = \mathbf{d}(\mathbf{k}) \cdot \boldsymbol{\sigma} \quad (1.35)$$

with $\boldsymbol{\sigma} = \{\sigma_x, \sigma_y, \sigma_z\}$ being the Pauli matrices spanning a two-dimensional Hilbert space, *e.g.* spin space. For this system the Chern number can be written as [29]

$$C = \frac{1}{4\pi} \int d\mathbf{k} [\partial_{k_x} \bar{\mathbf{d}}(\mathbf{k}) \times \partial_{k_y} \bar{\mathbf{d}}(\mathbf{k})] \cdot \bar{\mathbf{d}}(\mathbf{k}) \quad (1.36)$$

where we have defined the normalized vector $\bar{\mathbf{d}}(\mathbf{k}) = \mathbf{d}(\mathbf{k})/|\mathbf{d}(\mathbf{k})|$. Since the parameterizing vector $\bar{\mathbf{d}}(\mathbf{k})$ can be expressed as a vector on the S^2 Bloch sphere, we see that the Chern number is an integer counting the number of times $\bar{\mathbf{d}}(\mathbf{k})$ covers the S^2 Bloch sphere, when \mathbf{k} is integrated over the Brillouin torus T^2 , thus an effective mapping from T^2 to S^2 . In Fig. 1.5.(a) we show the configuration of the parameterizing vector $\bar{\mathbf{d}}(\mathbf{k})$ when swept across the whole Brillouin zone. It is clear from this figure that for $C = 0$, the $\bar{\mathbf{d}}(\mathbf{k})$ does not wind over the S^2 sphere, whereas for $C = +1$ the vector modulates such that it exactly wraps over the sphere once. The two phases with $C = \{0, 1\}$ are connected via a region in parameter space where the topological invariant is ill-defined. This region must be when a bulk gap closes, where $\mathbf{d}(\mathbf{k}) = \mathbf{0}$, leading to a diverging $\bar{\mathbf{d}}(\mathbf{k})$.

Equivalently systems in 1D can be studied by a winding number w , which is a mapping from the BZ S^1 sphere to the S^1 sphere of the parameterizing vector. The authors of [30]

developed an algebraic method to calculate the winding number for arbitrarily large matrices with chiral symmetry in one dimension. Due to the presence of the chiral symmetry Π , we can simultaneously diagonalize Π , and block off-diagonalize the Hamiltonian, in the way

$$\widehat{U}^\dagger \widehat{\mathcal{H}}(k) \widehat{U} = \begin{pmatrix} 0 & \hat{A}(k) \\ \hat{A}^\dagger(k) & 0 \end{pmatrix}, \quad \widehat{U}^\dagger \Pi \widehat{U} = \text{Diag} \{ \Pi_{11}, \Pi_{22} \dots \Pi_{NN} \}. \quad (1.37)$$

This allows us to define the normalized complex function $z(k) = \text{Det}[\hat{A}(k)] / |\text{Det}[\hat{A}(k)]|$, which has its poles when the bulk gap closes, as can be seen by the relation

$$\text{Det}[\widehat{U}^\dagger \widehat{\mathcal{H}}(k) \widehat{U}] = \prod_i E_i(k) = \text{Det}[\hat{A}(k)] \text{Det}[\hat{A}^\dagger(k)] \quad (1.38)$$

where $E_i(k)$ are the eigenenergies of the Hamiltonian. For a complex functions we can define a winding in the complex plane, which we can parametrize with the vector

$$\mathbf{d}(k) = (\text{Re}[\text{Det}[\hat{A}(k)]], \text{Im}[\text{Det}[\hat{A}(k)]], 0) \quad (1.39)$$

giving us the winding that counts the number of times $\bar{\mathbf{d}}(k)$ winds the S^1 sphere, while integrating over the BZ:

$$w = \frac{1}{2\pi} \int d\theta = \frac{1}{2\pi} \int dk \frac{d\theta}{dk} = -\frac{1}{2\pi} \int dk [\bar{\mathbf{d}}(k) \times \partial_k \bar{\mathbf{d}}(k)]_z. \quad (1.40)$$

Fig. 1.5.(b) illustrates the winding of the parameterizing vector $\bar{\mathbf{d}}(k)$ when k is swept across the BZ. It is clear that for $w = 0$, the vector does not wind the S^1 sphere, unlike the case of $w = 1$ where the vector winds once. Again note that the topological invariant is ill-defined when a gap closes, since $\bar{\mathbf{d}}(\mathbf{k})$ diverges, which implies that a topological phase transition can take place.

Lastly, we make a connection to the bulk-edge correspondence stated at the beginning of this chapter; we observe that the topological invariant is an integer, that only can change under gap closings. Therefore must two connected materials, with different invariants N and N' respectively, experience a number of $|N - N'|$ gap closings at the interface. This give rise to the zero energy topological protected edge modes.

Chapter 2

Topological Magnetic Iron-Based Superconductors

Let alone the interesting aspects of a superconducting phase: the Meissner effect, zero resistivity *etc.*, a whole new branch of superconductors was recently discovered by Kamihara *et al.* in 2008 [31], for which a plethora of magnetic, nematic and superconducting phases are accessible. The materials are referred to as iron-based superconductors (FeSCs) or iron pnictides/chalcogenides. Common characteristics for this family of materials is that their parent crystallographic structure all consists of quasi-2D layers with iron atoms placed on a square lattice, and a sublattice of As/Se above and below, as seen in Fig.2.1. Since a thorough introduction of the FeSCs is beyond the scope of this thesis, we will refer to the reviews of Refs. [32–34].

Particular interesting about these materials, within the context of this thesis, is the fact that they have a diverse phase diagram, as shown in Fig. 2.2.(a), adopted from [35]. In the diagram each colored region represents a distinct magnetic phase labeled by the phase's rotational symmetry, C_n , about the axes perpendicular to the quasi-2D layer. Some phases have an additional label C/IC following the rotational symmetry label, indicating whether the phase is commensurate/incommensurate. Lastly, at the foot of the magnetic dome, we see a superconducting dome, leaving some of the labels with an S indicating a superconducting phase. The occurrence of superconductivity at the foot of the magnetic dome is interesting by itself, since it has provided indication that the pairing glue is mediated by spin fluctuations, while it also give rise to regions where superconductivity coexists with magnetic phases. The coexistence supplemented with a broad variety of magnetic phases, renders these high- T_c materials as prominent candidates for TSCs.

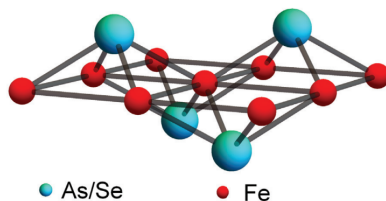


Figure 2.1: Quasi-2D crystal structure for the FeSCs, adopted from [32].

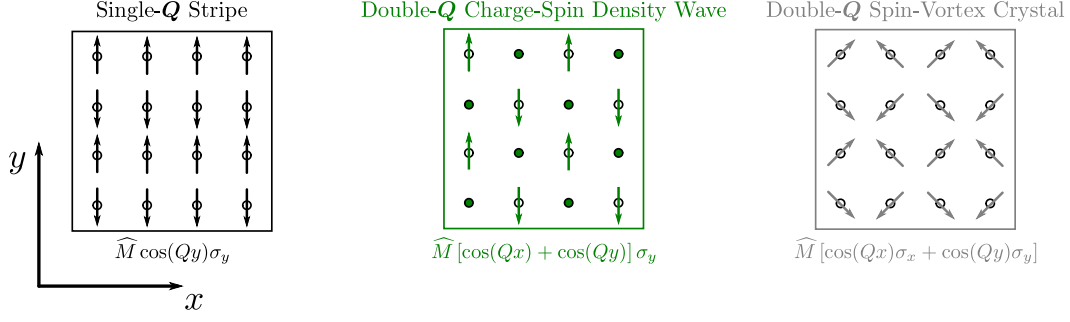


Figure 2.3: The three possible commensurate magnetic phases with $Q = \frac{\pi}{a}$. Note that the dark dots in the Double- Q charge-spin density wave phase represent charge ordering which also develops in this phase. The carets over the M below the figures represent matrices in orbital space.

where $Q = |\mathbf{Q}_l|$, and the carets denote matrices in orbital space, since a general magnetic OP will have different orbital weights. Here we have chosen an arbitrary direction for the ordering wave vectors \mathbf{Q}_l and of the moments, but one can easily perform rotations to connect to other spatial orientations. Note lastly that we have assumed the moments to be of equal lengths, but they could in principle be different [37]. In Fig. 3.1 we show the three phases.

Although the pairing mechanism of the FeSCs stays controversial, predictions about the nature of the pairing potential have already been established. The Cooper pairs consist of two electrons, and the total spin of the pairs are thus spin singlet, $S = 0$, or spin triplet, $S = 1$, assuming SOC to be absent. The lack of a net magnetic moment for the singlet configuration implies that, that the uniform spin susceptibility must be vanishing for $T \rightarrow 0$, which is indeed shown in Knight shift experiments (discussed in [38] Sec.4.). Based on these experimental data, it is strongly believed that the pairing truly is in the antisymmetric spin singlet configuration.

Returning to the experimental findings of [35], shown in Fig. 2.2.(a), we see that the three commensurate magnetic phases are insufficient to describe the broad variety of magnetic phases. This led the authors of [39] to study the possible incommensurate magnetic phases of a realistic five-orbital model, with a FS similar to the one depicted in Fig. 2.2.(b). Through Landau theory they found 9 possible incommensurate phases, whereof three of these were the extensions of the commensurate ones in Eqs. 2.2. The six new phases are shown below, and in Fig.2.4;

- Single- Q Magnetic Helix (●)

$$\widehat{\mathbf{M}}(\mathbf{r}) = \widehat{M} [\sin(\mathbf{Q}_1 \cdot \mathbf{r})\sigma_x + \cos(\mathbf{Q}_1 \cdot \mathbf{r})\sigma_y] \quad (2.3a)$$

- Double- Q Helix with in-plane Stripe (●)

$$\widehat{\mathbf{M}}(\mathbf{r}) = \widehat{M}_s \cos(\mathbf{Q}_1 \cdot \mathbf{r})\sigma_z + \widehat{M}_x \sin(\mathbf{Q}_2 \cdot \mathbf{r})\sigma_x + \widehat{M}_z \cos(\mathbf{Q}_2)\sigma_z \quad (2.3b)$$

- Double- Q Helix with out-of-plane Stripe (○)

$$\widehat{\mathbf{M}}(\mathbf{r}) = \widehat{M}_s \cos(\mathbf{Q}_1 \cdot \mathbf{r})\sigma_z + \widehat{M}_x \sin(\mathbf{Q}_2 \cdot \mathbf{r})\sigma_x + \widehat{M}_y \cos(\mathbf{Q}_2 \cdot \mathbf{r})\sigma_y \quad (2.3c)$$

- Double- \mathbf{Q} Double Parallel Helix (•)

$$\widehat{\mathbf{M}}(\mathbf{r}) = \widehat{M}_x [\sin(\mathbf{Q}_1 \cdot \mathbf{r}) + \sin(\mathbf{Q}_2 \cdot \mathbf{r})] \sigma_x + \widehat{M}_z [\cos(\mathbf{Q}_1 \cdot \mathbf{r}) + \cos(\mathbf{Q}_2 \cdot \mathbf{r})] \sigma_z \quad (2.3d)$$

- Double- \mathbf{Q} C_4 -symmetric Spin-Whirl Crystal (•)

$$\widehat{\mathbf{M}}(\mathbf{r}) = \widehat{M}_x [\cos(\mathbf{Q}_1 \cdot \mathbf{r}) + \cos(\mathbf{Q}_2 \cdot \mathbf{r})] \sigma_x + \widehat{M}_\perp [\sin(\mathbf{Q}_2 \cdot \mathbf{r}) \sigma_y + \sin(\mathbf{Q}_1 \cdot \mathbf{r}) \sigma_z] \quad (2.3e)$$

- Double- \mathbf{Q} C_2 -symmetric Spin-Whirl Crystal (•)

$$\widehat{\mathbf{M}}(\mathbf{r}) = \widehat{M}_s [\sin(\mathbf{Q}_1 \cdot \mathbf{r}) \sigma_x + \cos(\mathbf{Q}_1 \cdot \mathbf{r}) \sigma_z] + \widehat{M}_y \sin(\mathbf{Q}_2 \cdot \mathbf{r}) \sigma_y + \widehat{M}_z \cos(\mathbf{Q}_2 \cdot \mathbf{r}) \sigma_z. \quad (2.3f)$$

It is established that certain magnetic structures can lead to an effective SOC, which then again could lead to an effective p -wave pairing, see Sec. 1.2. It is therefore worthwhile to topologically classify these different phases when they coexist with superconductivity.

The FeSCs befall to be prominent candidates for topological superconductivity, due to their intrinsic development of regions with coexistence of magnetism and superconductivity. The troublesome procedure in engineering TSCs, discussed in Sec. 1.2, seems to be completely circumvented in the case of the FeSCs, as long as the magnetic phase can give rise to an effective SOC. To investigate this interesting new possibility for topological superconductivity, we will in the following formulate a general Hamiltonian for the FeSCs, which we at a later point generalize to multi-band systems, and topologically classify each of the 9 possible magnetic phases coexisting with certain classes of superconductivity.

2.1 General Hamiltonian for Magnetic Iron-Based Superconductors

A general Hamiltonian for a condensed matter system is typically of the type

$$H = H_e + H_I + H_{eI}, \quad (2.4)$$

where H_e describes the dynamics of the electronic degrees of freedom, H_I the ionic degrees of freedom and H_{eI} the interaction between the electrons and ions. We will, however, restrict the analysis to involve only the electronic dynamics H_e , subjected to a periodic potential generated by the static ions. We have here assumed the ions to have reached their equilibrium position, and thus only serve as a periodic potential. The Hamiltonian under interest then has the form

$$\begin{aligned} H &= H_0 + H_{\text{int}} \\ &= \int d\mathbf{r} \hat{\psi}^\dagger(\mathbf{r}) \left[-\frac{\hbar^2 \nabla^2}{2m} + V_I(\mathbf{r}) \right] \hat{\psi}(\mathbf{r}) \\ &\quad + \frac{1}{2} \sum_{\sigma \sigma'} \int d\mathbf{r} \int d\mathbf{r}' \psi_\sigma^\dagger(\mathbf{r}) \psi_{\sigma'}^\dagger(\mathbf{r}') V(\mathbf{r}, \mathbf{r}') \psi_{\sigma'}(\mathbf{r}') \psi_\sigma(\mathbf{r}) \end{aligned} \quad (2.5)$$

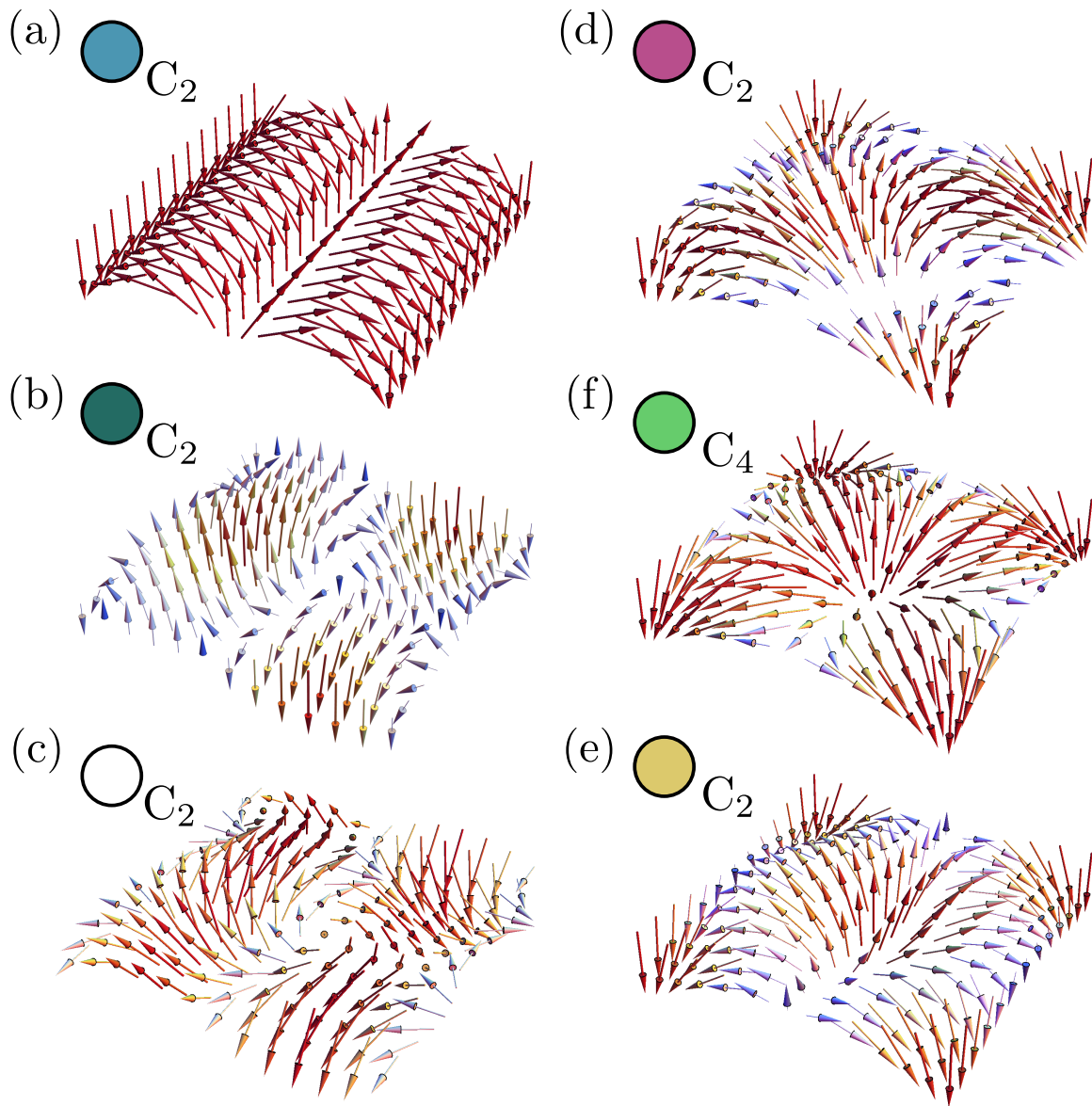


Figure 2.4: Magnetic profiles for the six new incommensurate phases, from [39]. The colored circles are tied to the Eqs. 2.3. This figure also contains the labels C_2 and C_4 representing the type of rotational symmetry preserved by the given magnetic phase.

where $V_I(\mathbf{r})$ is the periodic potential generated by the static ions, and $V(\mathbf{r}, \mathbf{r}')$ is the Coulomb electron-electron interaction. The field operator $\psi_\sigma(\mathbf{r})$ annihilates an electron at position \mathbf{r} with spin projection σ , and $\hat{\psi}(\mathbf{r}) = (\psi_\uparrow(\mathbf{r}), \psi_\downarrow(\mathbf{r}))^\top$. It is customary to expand the operators in the complete set of Wannier states [40], in order to obtain a convenient tight-binding Hamiltonian. We find the field operators in the new basis to be

$$\psi_\sigma^\dagger(\mathbf{r}) = \sum_\mu \sum_i \langle i\mu|\mathbf{r}\rangle d_{i\mu\sigma}^\dagger \quad (2.6)$$

where i labels the position of the static ion cores \mathbf{R}_i , and μ is the orbital/band of the itinerant electrons at the site. In the case of FeSCs, electrons are tightly bound to the $3d$ orbitals of the Fe atoms, which entitles us to make the crude approximation that the electron-electron interaction is dominated by on-site contributions, *i.e.* a delta function in lattice-site space [36, 41]. With this, we arrive at the tight-binding Hamiltonian

$$H = \sum_{ij} \sum_{\mu\nu} \hat{d}_{i\mu}^\dagger \left[-t_{ij}^{\mu\nu} + \mu_0 \delta_{i,j} \delta_{\mu,\nu} \right] \hat{d}_{j\nu} + \frac{1}{2} \sum_i \sum_{\substack{\mu\nu \\ \mu'\nu'}} \sum_{\sigma\sigma'} d_{i\sigma\mu}^\dagger d_{i\sigma'\nu}^\dagger V^{\mu\nu\nu'\mu'} d_{i\sigma'\nu'} d_{i\sigma\mu'} \quad (2.7)$$

where we have defined the following matrix elements

$$\mu_0 = \int d\mathbf{r} \langle i\mu|\mathbf{r}\rangle \left[-\frac{\hbar^2 \nabla^2}{2m} + V_I(\mathbf{r}) \right] \langle \mathbf{r}|i\mu\rangle, \quad (2.8a)$$

$$t_{ij}^{\mu\nu} = - \int d\mathbf{r} \langle i\mu|\mathbf{r}\rangle \left[-\frac{\hbar^2 \nabla^2}{2m} + V_I(\mathbf{r}) \right] \langle \mathbf{r}|j\nu\rangle, \quad (2.8b)$$

$$V^{\mu\nu\nu'\mu'} = \int d\mathbf{r} \int d\mathbf{r}' \langle \mu|\mathbf{r}\rangle \langle \nu|\mathbf{r}'\rangle V(\mathbf{r}, \mathbf{r}') \langle \mathbf{r}'|\nu'\rangle \langle \mathbf{r}|\mu'\rangle. \quad (2.8c)$$

Here are the hopping matrix elements $t_{ij}^{\mu\nu}$ often fitted to experimental data, or DFT calculations [32, 34, 42, 43]. Following the logic of App. B we can mean-field decouple the interaction in the magnetic channel, *i.e.* channels of the form $\langle d_{i\sigma\mu}^\dagger d_{j\sigma'\nu} \rangle$. In doing so, followed by a transformation to Fourier space, we retrieve the Hamiltonian

$$H^{\text{MF}}(\mathbf{k}) = H_0(\mathbf{k}) + H_{\text{mag}}(\mathbf{k}) \quad (2.9)$$

$$= \sum_{\mathbf{k}} \sum_{\mu\nu} \hat{d}_{\mathbf{k}\mu}^\dagger \xi_{\mathbf{k}}^{\mu\nu} \hat{d}_{\mathbf{k}\nu} + \sum_{\mathbf{k}\mathbf{q}_l} \hat{d}_{\mathbf{k}+\mathbf{q}_l\mu}^\dagger \mathbf{M}_l^{\mu\nu} \cdot \boldsymbol{\sigma} \hat{d}_{\mathbf{k}-\mathbf{q}_l\nu} + \text{const.}, \quad (2.10)$$

where $\xi_{\mathbf{k}}^{\mu\nu}$ are the dispersions in band space, $\mathbf{M}_l^{\mu\nu}$ are the magnetic order parameters defined in App. B, and $\mathbf{q}_l = \mathbf{Q}_l/2$ are the nesting vectors of the system. The nesting vectors will in the commensurate case be $\mathbf{Q}_1 = (\frac{\pi}{a}, 0)$ and $\mathbf{Q}_2 = (0, \frac{\pi}{a})$, as shown in Fig. 2.2.(b). For such a set of nesting vectors, $\mathbf{Q}_l = \frac{2\pi}{na}$ with $n \in \mathbb{Q} \setminus \{0\}$, it is possible to define a magnetic unit cell, with twice the size of the non-magnetic one. In extension to this we define a reduced Brillouin zone (RBZ), where the momentum summation now is over $\mathbf{k} \in (\mathbf{q}, -\mathbf{q}]$, which forces us to enlarge the spinor as follows

$$\hat{\psi}_{\mathbf{k}\mu} = (\psi_{\mathbf{k}+\mathbf{q}_2\mu}, \psi_{\mathbf{k}-\mathbf{q}_2\mu})^\top, \quad \psi_{\mathbf{k}\mu} = (\hat{d}_{\mathbf{k}+\mathbf{q}_1\mu}, \hat{d}_{\mathbf{k}-\mathbf{q}_1\mu})^\top. \quad (2.11)$$

Let us define the operator $\hat{d}_{\mathbf{k}}$ such that it captures both spin and orbital/band degrees of freedom. We can now write the Hamiltonian in the way

$$H^{\text{MF}}(\mathbf{k}) = \sum_{\mathbf{k} \in \text{RBZ}} \begin{pmatrix} \hat{d}_{\mathbf{k}+\mathbf{q}_1+\mathbf{q}_2}^\dagger & \hat{d}_{\mathbf{k}-\mathbf{q}_1+\mathbf{q}_2}^\dagger & \hat{d}_{\mathbf{k}+\mathbf{q}_1-\mathbf{q}_2}^\dagger & \hat{d}_{\mathbf{k}-\mathbf{q}_1-\mathbf{q}_2}^\dagger \\ \hat{\xi}_{\mathbf{k}+\mathbf{q}_1+\mathbf{q}_2} & \widehat{\mathbf{M}}_1 \cdot \boldsymbol{\sigma} & \widehat{\mathbf{M}}_2 \cdot \boldsymbol{\sigma} & 0 \\ \widehat{\mathbf{M}}_{-1} \cdot \boldsymbol{\sigma} & \hat{\xi}_{\mathbf{k}-\mathbf{q}_1+\mathbf{q}_2} & 0 & \widehat{\mathbf{M}}_2 \cdot \boldsymbol{\sigma} \\ \widehat{\mathbf{M}}_{-2} \cdot \boldsymbol{\sigma} & 0 & \hat{\xi}_{\mathbf{k}+\mathbf{q}_1-\mathbf{q}_2} & \widehat{\mathbf{M}}_1 \cdot \boldsymbol{\sigma} \\ 0 & \widehat{\mathbf{M}}_{-2} \cdot \boldsymbol{\sigma} & \widehat{\mathbf{M}}_{-1} \cdot \boldsymbol{\sigma} & \hat{\xi}_{\mathbf{k}-\mathbf{q}_1-\mathbf{q}_2} \end{pmatrix} \begin{pmatrix} \hat{d}_{\mathbf{k}+\mathbf{q}_1+\mathbf{q}_2} \\ \hat{d}_{\mathbf{k}-\mathbf{q}_1+\mathbf{q}_2} \\ \hat{d}_{\mathbf{k}+\mathbf{q}_1-\mathbf{q}_2} \\ \hat{d}_{\mathbf{k}-\mathbf{q}_1-\mathbf{q}_2} \end{pmatrix}, \quad (2.12)$$

where the carets in the matrix represent matrices in orbital/band space. As we mentioned earlier, the six new magnetic phases are incommensurate, which means that we cannot define a magnetic unit cell, nor a RBZ. This is due to the fact that the incommensurate wave vectors $Q_l = \frac{2\pi}{na}$ with $n \in \mathbb{R} \setminus \mathbb{Q}$, eventually will result in an infinite long spinor in Eq. 2.12. We will, however, do the approximation of only considering nesting close to the Fermi surface, *i.e.* cut-off the momentum summation, such that we only consider the lowest order of harmonics [39]. In doing so, we obtain a closed set of equations on the same form as Eq. 2.12, but with Q replaced by some incommensurate vector.

In order to circumvent writing the matrix in Eq. 2.12 explicitly, we employ the Pauli matrices λ and ρ , acting on the momentum-transfer spaces \mathbf{Q}_1 and \mathbf{Q}_2 respectively, and get

$$\begin{aligned} H_{\text{low}}^{\text{MF}}(\mathbf{k}) &= \sum_{\mathbf{k} \in \text{RBZ}} \Psi_{\mathbf{k}}^\dagger \left[\hat{h}_0^+(\mathbf{k}) + \hat{h}_1^-(\mathbf{k})\lambda_z + \hat{h}_2^-(\mathbf{k})\rho_z + \hat{h}_3^+(\mathbf{k})\lambda_z\rho_z \right. \\ &\quad \left. + \left(\frac{\widehat{\mathbf{M}}_1 + \widehat{\mathbf{M}}_{-1}}{2} \rho_x - \frac{\widehat{\mathbf{M}}_1 - \widehat{\mathbf{M}}_{-1}}{2i} \rho_y + \frac{\widehat{\mathbf{M}}_2 + \widehat{\mathbf{M}}_{-2}}{2} \lambda_x - \frac{\widehat{\mathbf{M}}_2 - \widehat{\mathbf{M}}_{-2}}{2i} \lambda_y \right) \cdot \boldsymbol{\sigma} \right] \Psi_{\mathbf{k}}. \\ &= \sum_{\mathbf{k} \in \text{RBZ}} \Psi_{\mathbf{k}}^\dagger \hat{h}(\mathbf{k}) \Psi_{\mathbf{k}} \end{aligned} \quad (2.13)$$

with the same spinor as in Eq.2.12, and the subscript of the Hamiltonian indicating that this is a low energy model for the incommensurate case. We have furthermore defined the matrices $\hat{h}_i^s(\mathbf{k})$ in the following manner;

$$\hat{h}_0^+(\mathbf{k}) = \frac{\hat{\xi}_{\mathbf{k}+\mathbf{q}_1+\mathbf{q}_2} + \hat{\xi}_{\mathbf{k}-\mathbf{q}_1+\mathbf{q}_2} + \hat{\xi}_{\mathbf{k}+\mathbf{q}_1-\mathbf{q}_2} + \hat{\xi}_{\mathbf{k}-\mathbf{q}_1-\mathbf{q}_2}}{4}, \quad (2.14a)$$

$$\hat{h}_1^-(\mathbf{k}) = \frac{\hat{\xi}_{\mathbf{k}+\mathbf{q}_1+\mathbf{q}_2} + \hat{\xi}_{\mathbf{k}-\mathbf{q}_1+\mathbf{q}_2} - \hat{\xi}_{\mathbf{k}+\mathbf{q}_1-\mathbf{q}_2} - \hat{\xi}_{\mathbf{k}-\mathbf{q}_1-\mathbf{q}_2}}{4}, \quad (2.14b)$$

$$\hat{h}_2^-(\mathbf{k}) = \frac{\hat{\xi}_{\mathbf{k}+\mathbf{q}_1+\mathbf{q}_2} - \hat{\xi}_{\mathbf{k}-\mathbf{q}_1+\mathbf{q}_2} + \hat{\xi}_{\mathbf{k}+\mathbf{q}_1-\mathbf{q}_2} - \hat{\xi}_{\mathbf{k}-\mathbf{q}_1-\mathbf{q}_2}}{4}, \quad (2.14c)$$

$$\hat{h}_3^+(\mathbf{k}) = \frac{\hat{\xi}_{\mathbf{k}+\mathbf{q}_1+\mathbf{q}_2} - \hat{\xi}_{\mathbf{k}-\mathbf{q}_1+\mathbf{q}_2} - \hat{\xi}_{\mathbf{k}+\mathbf{q}_1-\mathbf{q}_2} + \hat{\xi}_{\mathbf{k}-\mathbf{q}_1-\mathbf{q}_2}}{4}. \quad (2.14d)$$

To understand the meaning of the superscripts s of the matrices $\hat{h}_i^s(\mathbf{k})$, we first need to discuss the action of complex conjugation \mathcal{K} . The single-particle Hamiltonian $\hat{h}(\mathbf{k})$ in Eq. 2.13, is defined by the basis states $|\mathbf{k}, \mathbf{q}_l, \mu, \sigma\rangle$. The momentum dependence turns out to be an important property when considering complex conjugation, as can be seen by projecting the

basis onto real space (where we for brevity have dropped all quantum numbers, except for crystal momentum);

$$\langle \mathbf{r} | \mathbf{k} \rangle^* = \left(u_{\mathbf{k}}(\mathbf{r}) e^{i\mathbf{k} \cdot \mathbf{r}} \right)^* = u_{\mathbf{k}}^*(\mathbf{r}) e^{-i\mathbf{k} \cdot \mathbf{r}} \quad \Rightarrow \quad u_{-\mathbf{k}}^*(\mathbf{r}) e^{i\mathbf{k} \cdot \mathbf{r}} = \langle \mathbf{r} | -\mathbf{k} \rangle^* \equiv \mathcal{K} \langle \mathbf{r} | \mathbf{k} \rangle, \quad (2.15)$$

where we used the Bloch wave-function $\langle \mathbf{r} | \mathbf{k} \rangle = u_{\mathbf{k}}(\mathbf{r}) \exp(i\mathbf{k} \cdot \mathbf{r})$. We can see from the expressions above, that we can capture the action of \mathcal{K} by reversing the crystal momentum, and taking the complex conjugation of $u_{\mathbf{k}}(\mathbf{r})$. The ordering wave vectors will also be reversed under complex conjugation, however, since we have incorporated the star of the ordering wave vectors in the basis $|\mathbf{k}, \mathbf{q}_l, \mu, \sigma\rangle$, the complex conjugation can be captured in the matrix representation

$$\mathcal{K} \doteq \lambda_x \rho_x \mathcal{K}', \quad (2.16)$$

with \mathcal{K}' not acting on the ordering wave vectors, but only on \mathbf{k} . To confirm the validity of this representation consider the relation

$$\begin{aligned} \mathcal{K} \begin{pmatrix} \langle \mathbf{r} | \mathbf{k} + \mathbf{q}_1 + \mathbf{q}_2 \rangle \\ \langle \mathbf{r} | \mathbf{k} - \mathbf{q}_1 + \mathbf{q}_2 \rangle \\ \langle \mathbf{r} | \mathbf{k} + \mathbf{q}_1 - \mathbf{q}_2 \rangle \\ \langle \mathbf{r} | \mathbf{k} - \mathbf{q}_1 - \mathbf{q}_2 \rangle \end{pmatrix} &= \begin{pmatrix} \langle \mathbf{r} | -\mathbf{k} - \mathbf{q}_1 - \mathbf{q}_2 \rangle^* \\ \langle \mathbf{r} | -\mathbf{k} + \mathbf{q}_1 - \mathbf{q}_2 \rangle^* \\ \langle \mathbf{r} | -\mathbf{k} - \mathbf{q}_1 + \mathbf{q}_2 \rangle^* \\ \langle \mathbf{r} | -\mathbf{k} + \mathbf{q}_1 + \mathbf{q}_2 \rangle^* \end{pmatrix} \doteq \begin{pmatrix} 0 & 0 & 0 & 1 \\ 0 & 0 & 1 & 0 \\ 0 & 1 & 0 & 0 \\ 1 & 0 & 0 & 0 \end{pmatrix} \begin{pmatrix} \langle \mathbf{r} | -\mathbf{k} + \mathbf{q}_1 + \mathbf{q}_2 \rangle^* \\ \langle \mathbf{r} | -\mathbf{k} - \mathbf{q}_1 + \mathbf{q}_2 \rangle^* \\ \langle \mathbf{r} | -\mathbf{k} + \mathbf{q}_1 - \mathbf{q}_2 \rangle^* \\ \langle \mathbf{r} | -\mathbf{k} - \mathbf{q}_1 - \mathbf{q}_2 \rangle^* \end{pmatrix} \\ &= \lambda_x \rho_x \mathcal{K}' \begin{pmatrix} \langle \mathbf{r} | \mathbf{k} + \mathbf{q}_1 + \mathbf{q}_2 \rangle \\ \langle \mathbf{r} | \mathbf{k} - \mathbf{q}_1 + \mathbf{q}_2 \rangle \\ \langle \mathbf{r} | \mathbf{k} + \mathbf{q}_1 - \mathbf{q}_2 \rangle \\ \langle \mathbf{r} | \mathbf{k} - \mathbf{q}_1 - \mathbf{q}_2 \rangle \end{pmatrix}. \end{aligned} \quad (2.17)$$

Alas, the superscript of the matrices $\hat{h}_i^s(\mathbf{k})$ is simply the symmetry under complex conjugation;

$$\mathcal{K}^\dagger \hat{h}_i^s(\mathbf{k}) \mathcal{K} \doteq \lambda_x \rho_x \mathcal{K}'^\dagger \hat{h}_i^s(\mathbf{k}) \mathcal{K}' \lambda_x \rho_x = s \hat{h}_i^s(\mathbf{k}). \quad (2.18)$$

2.2 Bogoliubov-de Gennes Formalism

As it is clear from the preceding sections, the Hamiltonian of the FeSCs has to include the possibility for a superconducting order parameter. Although the pairing mechanism is controversial, it is adequate to describe the gap function through the usual BdG formalism. After a mean-field decoupling in the Cooper channel, of an effective attractive interaction, see App. B, the Hamiltonian obtains the form

$$H_{\text{sc}}^{\text{MF}}(\mathbf{k}) = \sum_{\mathbf{k}} \Psi_{\mathbf{k}}^\dagger \hat{h}(\mathbf{k}) \Psi_{\mathbf{k}} + \frac{1}{2} \sum_{\mathbf{k} \mathbf{q}} \left(\Psi_{\mathbf{k}+\mathbf{q}/2}^\dagger \hat{\Delta}_{\mathbf{k}\mathbf{q}} \Psi_{-\mathbf{k}+\mathbf{q}/2}^\dagger + \text{h.c.} \right) + \text{const.} \quad (2.19)$$

where the total momentum of the Cooper pairs, as usually, is set to zero, $\mathbf{q} = \mathbf{0}$, since we are here not concerned with a superconductor in a large magnetic field with the possibility of a Fulde-Ferrell-Larkin-Ovchinnikov phase (for an example see [44]). The matrix $\hat{h}(\mathbf{k})$ and the spinor $\Psi_{\mathbf{k}}$ are defined to be the same as in Eq.2.13. The Hamiltonian is now bilinear in

creation (annihilation) operators, but to rewrite it on a matrix form we need to double the degrees of freedom, and thereby include the single-hole behavior, therefore

$$\begin{aligned}
 H(\mathbf{k}) &= \frac{1}{2} \sum_{\mathbf{k}} \begin{pmatrix} \Psi_{\mathbf{k}}^\dagger & \Psi_{-\mathbf{k}}^\top \lambda_x \rho_x \end{pmatrix} \begin{pmatrix} \hat{h}(\mathbf{k}) & \hat{\Delta}_{\mathbf{k}} \\ \hat{\Delta}_{\mathbf{k}}^\dagger & -\lambda_x \rho_x \hat{h}^\top(-\mathbf{k}) \lambda_x \rho_x \end{pmatrix} \begin{pmatrix} \Psi_{\mathbf{k}} \\ \lambda_x \rho_x (\Psi_{-\mathbf{k}}^\dagger)^\top \end{pmatrix} + \cancel{\frac{1}{2} \sum_{\mathbf{k}} \text{Tr}[\hat{h}(\mathbf{k})]} \\
 &= \frac{1}{2} \sum_{\mathbf{k}} \hat{\Psi}_{\mathbf{k}}^\dagger \hat{\mathcal{H}}(\mathbf{k}) \hat{\Psi}_{\mathbf{k}}. \tag{2.20}
 \end{aligned}$$

The trace over $\hat{h}(\mathbf{k})$ originates from the inclusion of the single-hole behavior, $-\lambda_x \rho_x \hat{h}^\top(-\mathbf{k}) \lambda_x \rho_x$, and is simply a constant shift of the eigenenergies and can therefore be dropped. Here we again see the matrix representation $\lambda_x \rho_x$ that reverse the ordering wave-vectors, as seen in Eq. 2.17, which is necessary since a hole has the opposite crystal momentum compared to its electronic counterpart.

The BdG formalism has the advantage that certain symmetry transformations obtain a simplified form, as will become clear later in this chapter. Consider at first the relation for the spinor

$$\hat{\Psi}_{\mathbf{k}}^\dagger = \hat{\Psi}_{-\mathbf{k}}^\top \tau_x \lambda_x \rho_x \tag{2.21}$$

inserting this in Eq. 2.20. gives the powerful relation

$$\hat{\mathcal{H}}(\mathbf{k}) = -\tau_x \lambda_x \rho_x \hat{\mathcal{H}}^\top(-\mathbf{k}) \tau_x \lambda_x \rho_x, \tag{2.22}$$

which will be used throughout in the upcoming sections. Furthermore it reflects the antisymmetry of the pairing potential $\hat{\Delta}_{\mathbf{k}} = -\hat{\Delta}_{-\mathbf{k}}^\top$. This restriction on the pairing potential, helps in formulating a general superconducting OP.

Superconducting Order Parameter

As mentioned above, we know that the pairing potential needs to be antisymmetric under quantum number exchange of the electrons; $\hat{\Delta}_{\mathbf{k}} = -\hat{\Delta}_{-\mathbf{k}}^\top$. We also know that this matrix is defined in orbital/band, spin and Bloch space. Thus all combinations generating an antisymmetric pairing function are allowed. Based on this, we can have the following combinations for spin singlet pairing

- Symmetric in Bloch space and orbital/band exchange.
- Antisymmetric in Bloch space and orbital/band exchange.

Which generates a general singlet pairing OP on the form

$$\hat{\Delta}_{\mathbf{k}} = i \left(\hat{\Delta}_{\text{orb}}^+ f(\mathbf{k}) + i \hat{\Delta}_{\text{orb}}^- d(\mathbf{k}) \right) \sigma_y, \tag{2.23}$$

where we have defined the even/odd functions, $f(\mathbf{k}) = f(-\mathbf{k})$, $d(\mathbf{k}) = -d(-\mathbf{k})$, and the matrices in band/orbital space $\hat{\Delta}_{\text{orb}}^s$, with the property

$$\left(\hat{\Delta}_{\text{orb}}^s \right)^\top = s \hat{\Delta}_{\text{orb}}^s. \tag{2.24}$$

Notice that we here have defined the odd orbital/band matrices as complex matrices, similar to the usual representation of spin operators with \hat{S}_y being imaginary. For a five-orbital model the orbital space would be spanned by the $SU(5)$ matrices defined in App. A, where we have used the same definition with the antisymmetric orbitals being imaginary. Lastly we include the possibility of a complex pairing by splitting $\hat{\Delta}_{\mathbf{k}}$ up into real and imaginary parts, so that

$$\hat{\Delta}_{\mathbf{k}} = \hat{\Delta}_{\mathbf{k}}^{\text{Re}} + i\hat{\Delta}_{\mathbf{k}}^{\text{Im}}. \quad (2.25)$$

With a general singlet pairing potential established in Eq.2.23, we observe that a convenient rotation of the hole component of the spinor can be performed

$$\hat{\Psi}_{\mathbf{k}}^\dagger = \left(\Psi_{\mathbf{k}}^\dagger, -i\Psi_{-\mathbf{k}}^\dagger \lambda_x \rho_x \sigma_y \right) \quad (2.26)$$

which results in a pairing potential diagonal in spin space, and a convenient representation of the magnetic OPs. The BdG relations in Eq.2.21., and Eq.2.22. get modified to

$$\hat{\Psi}_{\mathbf{k}}^\dagger = \hat{\Psi}_{-\mathbf{k}}^\dagger \tau_y \lambda_x \rho_x \sigma_y, \quad \hat{\mathcal{H}}(\mathbf{k}) = -\tau_y \lambda_x \rho_x \sigma_y \hat{\mathcal{H}}^\dagger(-\mathbf{k}) \tau_y \lambda_x \rho_x \sigma_y. \quad (2.27)$$

The final single-particle BdG Hamiltonian thus becomes

$$\begin{aligned} \hat{\mathcal{H}}(\mathbf{k}) = & \tau_z \left(\hat{h}_0^+(\mathbf{k}) + \hat{h}_1^-(\mathbf{k})\lambda_z + \hat{h}_2^-(\mathbf{k})\rho_z + \hat{h}_3^+(\mathbf{k})\lambda_z\rho_z \right) \\ & + \left(\frac{\widehat{M}_1 + \widehat{M}_{-1}}{2} \rho_x - \frac{\widehat{M}_1 - \widehat{M}_{-1}}{2i} \rho_y + \frac{\widehat{M}_2 + \widehat{M}_{-2}}{2} \lambda_x - \frac{\widehat{M}_2 - \widehat{M}_{-2}}{2i} \lambda_y \right) \cdot \boldsymbol{\sigma} \\ & + \tau_x \left(\hat{\Delta}_0^{+\text{Re}}(\mathbf{k}) + \hat{\Delta}_1^{-\text{Re}}(\mathbf{k})\lambda_z + \hat{\Delta}_2^{-\text{Re}}(\mathbf{k})\rho_z + \hat{\Delta}_3^{+\text{Re}}(\mathbf{k})\lambda_z\rho_z \right) \\ & - \tau_y \left(\hat{\Delta}_0^{+\text{Im}}(\mathbf{k}) + \hat{\Delta}_1^{-\text{Im}}(\mathbf{k})\lambda_z + \hat{\Delta}_2^{-\text{Im}}(\mathbf{k})\rho_z + \hat{\Delta}_3^{+\text{Im}}(\mathbf{k})\lambda_z\rho_z \right) \end{aligned} \quad (2.28)$$

where we have defined the matrices $\hat{\Delta}_i^{s\text{Re/Im}}(\mathbf{k})$ in a similar way as in Eqs.2.14, but with $\hat{\xi}_{\mathbf{k}}$ replaced by $\hat{\Delta}_{\mathbf{k}}$.

Symmetries in BdG Formalism

To incorporate the symmetry operation, defined in Eq. 1.15, in the BdG formalism, we should also include the transformation of the hole sector. By means of the fermionic anti-commutation relations, we arrive at the matrix representation of G in the BdG formalism as

$$D(G) = \frac{d(G) + \lambda_x \rho_x \sigma_y d^\dagger(G) \lambda_x \rho_x \sigma_y}{2} \mathbb{1}_\tau + \frac{d(G) - \lambda_x \rho_x \sigma_y d^\dagger(G) \lambda_x \rho_x \sigma_y}{2} \tau_z. \quad (2.29)$$

The BdG Hamiltonian in the symmetry transformed basis is related to the old basis through the relation

$$G^\dagger \hat{\mathcal{H}}(\mathbf{k}) G \doteq D^\dagger(G) \hat{\mathcal{H}}(G\mathbf{k}) D(G). \quad (2.30)$$

Let us revisit the aforementioned symmetries in Sec. 1.4 now that the basis $|\mathbf{k}, \mathbf{q}_l, \mu, \sigma\rangle$ of the single-particle Hamiltonian $\hat{h}(\mathbf{k})$ has been established, and that we know how the BdG Hamiltonian transforms.

Inversion

We have the relation for the inversion transformed basis

$$\mathcal{I}|\mathbf{k}, \mathbf{q}_l, \mu, \sigma\rangle = |-\mathbf{k}, -\mathbf{q}_l, \mathcal{I}\mu, \sigma\rangle. \quad (2.31)$$

The systems under consideration either have μ as a band index, *i.e.* invariant under inversion if the inversion is an element of the symmetry point group, or as $3d$ -orbitals. These orbitals have orbital angular momentum $l = 2$, which means $\mathcal{I}\mu = \mu$ (see Eq. 1.19). We are thus only concerned with the transformation of the wave vectors. In order to reverse the ordering wave vectors we have, see Eq. 2.17

$$d(\mathcal{I}) = D(\mathcal{I}) = \lambda_x \rho_x. \quad (2.32)$$

The BdG Hamiltonian in the transformed basis is related to the old in the way;

$$\mathcal{I}^\dagger \widehat{\mathcal{H}}(\mathbf{k}) \mathcal{I} \doteq \lambda_x \rho_x \widehat{\mathcal{H}}(\mathcal{I}\mathbf{k}) \lambda_x \rho_x = -\tau_y \sigma_y \widehat{\mathcal{H}}^\Gamma(\mathbf{k}) \tau_y \sigma_y, \quad (2.33)$$

where Eq.2.27. was used in the last equality.

Charge Conjugation

From Eq.2.27 we find the matrix representation of charge conjugation to be

$$d(\mathcal{C}) = D(\mathcal{C}) = \tau_y \lambda_x \rho_x \sigma_y \mathcal{K}'. \quad (2.34)$$

The BdG Hamiltonian will transform as follows

$$D^\dagger(\mathcal{C}) \widehat{\mathcal{H}}(\mathbf{k}) D(\mathcal{C}) = \tau_y \lambda_x \rho_x \sigma_y \widehat{\mathcal{H}}^\Gamma(-\mathbf{k}) \tau_y \lambda_x \rho_x \sigma_y = -\widehat{\mathcal{H}}(\mathbf{k}) \quad (2.35)$$

where we made use of Eq.2.27 in the latter equality. One notes that this antiunitary charge conjugation coincides with the generalized charge conjugation, $\Xi = D(\mathcal{C})$, discussed in Chap. 2.3, for classes that can harbor MFs. This generalized charge conjugation operator renders the Hamiltonian in one of the three Majorana classes; BDI, D or DIII.

Translation

How do translation operations now modify the basis of our system? To answer this question, let us for now drop the quantum numbers: \mathbf{q}_l, μ and σ for clearance, and consider a translation by a single lattice constant a along $\bar{\mathbf{n}}$

$$\begin{aligned} t_a^{\bar{\mathbf{n}}} |\mathbf{k}\rangle &= \int d\mathbf{r} t_a^{\bar{\mathbf{n}}} |\mathbf{r}\rangle \langle \mathbf{r} | \mathbf{k}\rangle = \int d\mathbf{r} |\mathbf{r} + \bar{\mathbf{n}}a\rangle \langle \mathbf{r} | \mathbf{k}\rangle = \int d\mathbf{r} |\mathbf{r}\rangle \langle \mathbf{r} - \bar{\mathbf{n}}a | \mathbf{k}\rangle \\ &= \int d\mathbf{r} |\mathbf{r}\rangle u_{\mathbf{k}}(\mathbf{r} - \bar{\mathbf{n}}a) e^{i\mathbf{k} \cdot (\mathbf{r} - \bar{\mathbf{n}}a)} = \int d\mathbf{r} |\mathbf{r}\rangle \langle \mathbf{r} | \mathbf{k}\rangle e^{-i\mathbf{k} \cdot \bar{\mathbf{n}}a} = |\mathbf{k}\rangle e^{-i\mathbf{k} \cdot \bar{\mathbf{n}}a}, \end{aligned} \quad (2.36)$$

where the Bloch wave function $\langle \mathbf{r} | \mathbf{k}\rangle = u_{\mathbf{k}}(\mathbf{r}) \exp(i\mathbf{k} \cdot \mathbf{r})$, and the periodicity $u_{\mathbf{k}}(\mathbf{r} + \bar{\mathbf{n}}a) = u_{\mathbf{k}}(\mathbf{r})$ were used. The translation thus acts as a $U(1)$ rotation on the basis states. By including the ordering wave vectors in the basis, the following translations have the matrix representations

$$D(t_a^{\bar{\mathbf{x}}}) = \tau_z \rho_z, \quad D(t_a^{\bar{\mathbf{y}}}) = \tau_z \lambda_z, \quad D(t_a^{(1,1)}) = \lambda_z \rho_z. \quad (2.37)$$

The overall $U(1)$ phases have been removed in the matrix representations above, since they leave the Hamiltonian inert.

Lastly it is possible to define, in a similar way, a translation in momentum space. Consider the basis state, where we again have dropped the remaining quantum numbers for clarity, translated by the momentum p along $\bar{\mathbf{n}}$

$$t_p^{\bar{\mathbf{n}}} |\mathbf{k}\rangle = |\mathbf{k} + p\bar{\mathbf{n}}\rangle. \quad (2.38)$$

If the translation coincides with the ordering wave-vectors, we must have the following matrix representations

$$D(t_Q^{\bar{\mathbf{x}}}) = \rho_x, \quad D(t_Q^{\bar{\mathbf{y}}}) = \lambda_x, \quad D(t_Q^{(1,1)}) = \lambda_x \rho_x. \quad (2.39)$$

Note that a translation of $Q(1,1)$ is used in defining the complex conjugation operator $\mathcal{K} = t_Q^{(1,1)} \mathcal{K}' \doteq \lambda_x \rho_x \mathcal{K}'$, since this translation changes the sign of all the ordering wave-vectors.

Time Reversal

For spin-1/2 particles we retrieve the following matrix representation

$$\mathcal{T} \doteq \widehat{U}_{\mathcal{T}} \mathcal{K} = e^{-i\widehat{S}_y \pi / \hbar} \mathcal{K} = -i\sigma_y \mathcal{K} = -i\lambda_x \rho_x \sigma_y \mathcal{K}', \quad (2.40)$$

which transforms the Hamiltonian as

$$\widehat{\mathcal{H}}'(\mathbf{k}) = \lambda_x \rho_x \sigma_y \mathcal{K}'^\dagger \widehat{\mathcal{H}}(\mathbf{k}) \mathcal{K}' \lambda_x \rho_x \sigma_y = \lambda_x \rho_x \sigma_y \widehat{\mathcal{H}}^\dagger(-\mathbf{k}) \lambda_x \rho_x \sigma_y = -\tau_y \widehat{\mathcal{H}}(\mathbf{k}) \tau_y \quad (2.41)$$

where Eq. 2.27. again was exploited in the latter equality.

Simplification of Magnetic Order Parameters

On physical grounds we would expect the magnetic OPs to transform in certain ways under symmetry transformations. Let us denote the terms of the Hamiltonian with magnetic OPs as $\widehat{\mathcal{H}}_{\text{mag}}$. We have therefore the following restrictions

$$\mathcal{C}^\dagger \widehat{\mathcal{H}}_{\text{mag}} \mathcal{C} = -\widehat{\mathcal{H}}_{\text{mag}}, \quad \mathcal{T}^\dagger \widehat{\mathcal{H}}_{\text{mag}} \mathcal{T} = -\widehat{\mathcal{H}}_{\text{mag}}. \quad (2.42)$$

To see the effects of the two symmetry operations, let us consider the magnetic OPs with ordering wave vector \mathbf{Q}_1 from $\widehat{\mathcal{H}}_{\text{mag}}$;

$$\widehat{\mathcal{H}}_{\text{mag}}^{\mathbf{Q}_1} = \left[\frac{\widehat{M}_1 + \widehat{M}_{-1}}{2} \rho_x - \frac{\widehat{M}_1 - \widehat{M}_{-1}}{2i} \rho_y \right] \cdot \boldsymbol{\sigma}. \quad (2.43)$$

The magnetic OPs are clearly odd under time-reversal, see Eq.2.41. The particle hole symmetry puts a restriction on the OPs, as can be seen from the relation

$$\begin{aligned} \mathcal{C}^\dagger \widehat{\mathcal{H}}_{\text{mag}}^{\mathbf{Q}_1} \mathcal{C} &= \mathcal{C}^\dagger \left[\frac{\widehat{M}_1 + \widehat{M}_{-1}}{2} \rho_x - \frac{\widehat{M}_1 - \widehat{M}_{-1}}{2i} \rho_y \right] \cdot \boldsymbol{\sigma} \mathcal{C} \\ &= - \left[\mathcal{K}'^\dagger \frac{\widehat{M}_1 + \widehat{M}_{-1}}{2} \mathcal{K}' \rho_x - \mathcal{K}'^\dagger \frac{\widehat{M}_1 - \widehat{M}_{-1}}{2i} \mathcal{K}' \rho_y \right] \cdot \boldsymbol{\sigma}. \end{aligned} \quad (2.44)$$

and similarly for an magnetic OP with \mathbf{Q}_2 . Since \mathcal{K}' does not act on the ordering wave vector, we must have the relation $\mathcal{K}'^\dagger \widehat{\mathbf{M}}_l \mathcal{K}' = \widehat{\mathbf{M}}_l^*$, compared to the full complex conjugation which would act as $\mathcal{K}'^\dagger \widehat{\mathbf{M}}_l \mathcal{K}' = \widehat{\mathbf{M}}_{-l}^*$. Consider the complex conjugation \mathcal{K}' on the OP, as follows

$$\begin{aligned} \mathcal{K}'^\dagger \left[\frac{\widehat{\mathbf{M}}_l + \widehat{\mathbf{M}}_{-l}}{2} \right] \mathcal{K}' &= \left[\frac{\widehat{\mathbf{M}}_l + \widehat{\mathbf{M}}_{-l}}{2} \right]^* = \left[\frac{\widehat{\mathbf{M}}_l + \widehat{\mathbf{M}}_l^\dagger}{2} \right]^* = \frac{\widehat{\mathbf{M}}_l^* + \widehat{\mathbf{M}}_l^\dagger}{2} = \left[\frac{\widehat{\mathbf{M}}_l + \widehat{\mathbf{M}}_{-l}}{2} \right]^\dagger \\ &\Downarrow \\ \left[\frac{\widehat{\mathbf{M}}_l + \widehat{\mathbf{M}}_{-l}}{2} \right]^\dagger &= \frac{\widehat{\mathbf{M}}_l + \widehat{\mathbf{M}}_{-l}}{2} \end{aligned} \quad (2.45)$$

with the latter equation true for a magnetic OP odd under charge conjugation, as dictated in Eq.2.42. Applying the same analysis to the second OP in Eq.2.43, we get similarly

$$\begin{aligned} \mathcal{K}'^\dagger \left[\frac{\widehat{\mathbf{M}}_l - \widehat{\mathbf{M}}_{-l}}{2i} \right] \mathcal{K}' &= \left[\frac{\widehat{\mathbf{M}}_l - \widehat{\mathbf{M}}_{-l}}{2i} \right]^* = \left[\frac{\widehat{\mathbf{M}}_l - \widehat{\mathbf{M}}_l^\dagger}{2i} \right]^* = -\frac{\widehat{\mathbf{M}}_l^* - \widehat{\mathbf{M}}_l^\dagger}{2i} = \left[\frac{\widehat{\mathbf{M}}_l - \widehat{\mathbf{M}}_{-l}}{2i} \right]^\dagger \\ &\Downarrow \\ \left[\frac{\widehat{\mathbf{M}}_l - \widehat{\mathbf{M}}_{-l}}{2i} \right]^\dagger &= \frac{\widehat{\mathbf{M}}_l - \widehat{\mathbf{M}}_{-l}}{2i}. \end{aligned} \quad (2.46)$$

Since both matrices are symmetric under complex conjugation, *i.e.* real matrices, one might as well define the following compact notation

$$\widehat{\mathbf{M}}_l^{\text{Re}} = \frac{\widehat{\mathbf{M}}_l + \widehat{\mathbf{M}}_{-l}}{2}, \quad \widehat{\mathbf{M}}_l^{\text{Im}} = \frac{\widehat{\mathbf{M}}_l - \widehat{\mathbf{M}}_{-l}}{2i}. \quad (2.47)$$

The superscript nomenclature is appropriate due to the fact that the matrices are real. This results in the compact single particle Hamiltonian

$$\begin{aligned} \widehat{\mathcal{H}}(\mathbf{k}) &= \tau_z \left(\hat{h}_0^+(\mathbf{k}) + \hat{h}_1^-(\mathbf{k})\lambda_z + \hat{h}_2^-(\mathbf{k})\rho_z + \hat{h}_3^+(\mathbf{k})\lambda_z\rho_z \right) \\ &\quad + \left(\widehat{\mathbf{M}}_1^{\text{Re}}\rho_x - \widehat{\mathbf{M}}_1^{\text{Im}}\rho_y + \widehat{\mathbf{M}}_2^{\text{Re}}\lambda_x - \widehat{\mathbf{M}}_2^{\text{Im}}\lambda_y \right) \cdot \boldsymbol{\sigma} \\ &\quad + \tau_x \left(\hat{\Delta}_0^{+\text{Re}}(\mathbf{k}) + \hat{\Delta}_1^{-\text{Re}}(\mathbf{k})\lambda_z + \hat{\Delta}_2^{-\text{Re}}(\mathbf{k})\rho_z + \hat{\Delta}_3^{+\text{Re}}(\mathbf{k})\lambda_z\rho_z \right) \\ &\quad - \tau_y \left(\hat{\Delta}_0^{+\text{Im}}(\mathbf{k}) + \hat{\Delta}_1^{-\text{Im}}(\mathbf{k})\lambda_z + \hat{\Delta}_2^{-\text{Im}}(\mathbf{k})\rho_z + \hat{\Delta}_3^{+\text{Im}}(\mathbf{k})\lambda_z\rho_z \right) \end{aligned} \quad (2.48)$$

2.3 Topological Classification of Iron-Based Superconductors

With the low energy Hamiltonian for the FeSCs established, it is now possible to classify the different magnetic phases coexisting with superconductivity. Since the procedure for classifying the Hamiltonians is somewhat cumbersome, only a single classification scheme is shown here. The interested reader is encouraged to study all the classifications in detail in App. C. Classification tables summarizing the results of this section are to be found in Table. 2.1-2.2.

Topological Classification of Double- \mathbf{Q} C_4 -symmetric Spin-Whirl Crystal (●)

The Fourier components of the Double- \mathbf{Q} C_4 -symmetric Spin-Whirl (●) magnetic OPs from Eq. 2.3e are

$$\widehat{\mathbf{M}}_1 = \frac{1}{2} \left(\widehat{M}_x, 0, -i\widehat{M}_\perp \right), \quad \widehat{\mathbf{M}}_2 = \frac{1}{2} \left(\widehat{M}_x, -i\widehat{M}_\perp, 0 \right). \quad (2.49)$$

The magnitudes of the fields are related through the Landau parameter Λ [39], in the way

$$\widehat{M}_x = \frac{\widehat{M} \sin(\Lambda)}{\sqrt{2}}, \quad \widehat{M}_\perp = \frac{\widehat{M} \cos(\Lambda)}{\sqrt{2}}. \quad (2.50)$$

After insertion in Eq. 2.48 we obtain the Hamiltonian to be classified:

$$\begin{aligned} \widehat{\mathcal{H}}(\mathbf{k}) = & \tau_z \left[\widehat{h}_0^+(\mathbf{k}) + \widehat{h}_1^-(\mathbf{k})\lambda_z + \widehat{h}_2^-(\mathbf{k})\rho_z + \widehat{h}_3^+(\mathbf{k})\lambda_z\rho_z \right] \\ & + \frac{\widehat{M}_x\rho_x\sigma_x + \widehat{M}_\perp\rho_y\sigma_z}{2} + \frac{\widehat{M}_x\lambda_x\sigma_x + \widehat{M}_\perp\lambda_y\sigma_y}{2} \\ & + \tau_x \left(\widehat{\Delta}_0^{+\text{Re}}(\mathbf{k}) + \widehat{\Delta}_1^{-\text{Re}}(\mathbf{k})\lambda_z + \widehat{\Delta}_2^{-\text{Re}}(\mathbf{k})\rho_z + \widehat{\Delta}_3^{+\text{Re}}(\mathbf{k})\lambda_z\rho_z \right) \\ & - \tau_y \left(\widehat{\Delta}_0^{+\text{Im}}(\mathbf{k}) + \widehat{\Delta}_1^{-\text{Im}}(\mathbf{k})\lambda_z + \widehat{\Delta}_2^{-\text{Im}}(\mathbf{k})\rho_z + \widehat{\Delta}_3^{+\text{Im}}(\mathbf{k})\lambda_z\rho_z \right). \end{aligned} \quad (2.51)$$

We will first in the classification consider a real superconducting order parameter, followed by a more general complex one. We will also assume the matrices in orbital/band space to be without any symmetries, hence not leading to any unitary symmetries. We obtain the following classification for the different gap functions

- **Real Superconducting OP:**

For a strictly real superconducting order parameter, *i.e.* $\widehat{\Delta}_i^{s\text{Im}}(\mathbf{k}) = 0$, the system acquires a chiral symmetry, along with a generalized time-reversal and charge-conjugation symmetry;

$$\Theta^2 = (\lambda_y\rho_y\sigma_y\mathcal{K}')^2 = -\mathbf{1}, \quad \Xi^2 = (\tau_y\lambda_x\rho_x\sigma_y\mathcal{K}')^2 = +\mathbf{1}, \quad \Pi^2 = (\tau_y\lambda_z\rho_z)^2 = \mathbf{1}. \quad (2.52)$$

The Hamiltonian thus belongs to the class DIII, with an \mathbb{Z}_2 invariant in 2D. The magnetic texture in question cannot be defined in 1D, due to the double- \mathbf{Q} nesting, and the topological invariant in 1D should therefore not be considered. We furthermore observe that the generalized time-reversal operator can be rewritten in the form $\Theta = D(t_a^{(1,1)})D(\mathcal{T})$, constituting a hidden symmetry [23], with a translation of one lattice constant in x and y -direction, followed by a time-reversal operation.

- **Complex Superconducting OP:**

By setting $\widehat{\Delta}_i^{s\text{Im}} \neq 0$, the presence of all Nambu matrices breaks chiral symmetry and generalized time-reversal. However, charge conjugation is still present;

$$\Theta^2 = 0, \quad \Xi^2 = (\tau_y\lambda_x\rho_x\sigma_y\mathcal{K}')^2 = +\mathbf{1}, \quad \Pi^2 = 0. \quad (2.53)$$

It is clear that the system resides in the class D, where a \mathbb{Z} invariant can be defined in 2D.

For classification of the remaining magnetic phases coexisting with superconductivity, see the Tables. 2.1-2.2.

Real Superconducting OP			
Phase	Class	1	2
Single- Q Stripe	$\text{BDI} \oplus \text{BDI}$	\mathbb{Z}	0
Double- Q Charge-Spin Density Wave	$\text{CI} \oplus \text{CI}$	-	0
Double- Q Spin-Vortex Crystal	$\text{BDI} \oplus \text{BDI}$	-	0

Complex Superconducting OP			
Phase	Class	1	2
Single- Q Stripe	$\text{D} \oplus \text{D}$	\mathbb{Z}_2	\mathbb{Z}
Double- Q Charge-Spin Density Wave	$\text{C} \oplus \text{C}$	-	\mathbb{Z}
Double- Q Spin-Vortex Crystal	$\text{D} \oplus \text{D}$	-	\mathbb{Z}

Table 2.1: Table summarizing the topological classification for the commensurate magnetic phases, carried out in App. C. Each table considers distinct superconducting order parameters. The possible types of invariants are also shown in the table, for a given dimensionality. Certain magnetic textures can not be defined in 1D, and are indicated by a minus instead of the usual type of invariant.

Real Superconducting OP			
Phase	Class	1	2
Single- Q Magnetic Helix (●)	$\text{BDI} \oplus \text{BDI}$	\mathbb{Z}	0
Double- Q Helix with in-plane Stripe (●)	$\text{AIII} \oplus \text{AIII}$	-	0
Double- Q Helix with out-of-plane Stripe (○)	DIII	-	\mathbb{Z}_2
Double- Q Double Parallel Helix (●)	$\text{AIII} \oplus \text{AIII}$	-	0
Double- Q C_4 -symmetric Spin-Whirl Crystal (●)	DIII	-	\mathbb{Z}_2
Double- Q C_2 -symmetric Spin-Whirl Crystal (●)	DIII	-	\mathbb{Z}_2

Complex Superconducting OP			
Phase	Class	1	2
Single- Q Magnetic Helix (●)	$\text{D} \oplus \text{D}$	\mathbb{Z}_2	\mathbb{Z}
Double- Q Helix with in-plane Stripe (●)	$\text{A} \oplus \text{A}$	-	\mathbb{Z}
Double- Q Helix with out-of-plane Stripe (○)	D	-	\mathbb{Z}
Double- Q Double Parallel Helix (●)	$\text{A} \oplus \text{A}$	-	\mathbb{Z}
Double- Q C_4 -symmetric Spin-Whirl Crystal (●)	D	-	\mathbb{Z}
Double- Q C_2 -symmetric Spin-Whirl Crystal (●)	D	-	\mathbb{Z}

Table 2.2: Table summarizing the topological classification for the commensurate magnetic phases, carried out in App. C. Each table considers distinct superconducting order parameters. The possible types of invariants are also shown in the table, for a given dimensionality. Certain magnetic textures can not be defined in 1D, and are indicated by a minus instead of the usual type of invariant.

2.4 Point Group Symmetry for the FeSCs

Point group theory is an important tool in understanding phase transitions, predicting possible order parameters and selection rules [26, 27, 45–48]. Even more one needs to have in mind point group symmetries when doing topological classifications. Before discussing and applying the tools of point group theory on the FeSCs, we will first briefly introduce some relevant concepts and derivations based on Ref. [26, 27].

Point Group Symmetry

A symmetry point group is a finite group consisting of symmetry operations, where the given operation leaves at least one point invariant. The symmetry operations include rotations, mirror reflections, improper rotations *etc.*, which leave the physical, or abstract, object invariant. The fact that these operations form a finite group $\mathcal{G} = \{G_0, G_1, G_2 \dots G_{N-1}\}$, with N being the order of the group, apply us with the following usable knowledge:

- a) The group is stable, *i.e.* the product of any two elements in \mathcal{G} is itself contained in \mathcal{G} ;

$$\text{if } G_i, G_j \in \mathcal{G}, \quad \text{then } G_k = G_i G_j \quad \text{with } G_k \in \mathcal{G}. \quad (2.54)$$

- b) The associative law is true

$$G_i (G_j G_l) = (G_i G_j) G_l, \quad \text{for all elements } G_i, G_j, G_l \in \mathcal{G}. \quad (2.55)$$

- c) The set \mathcal{G} has an identity (also called unit) element satisfying

$$EG = GE = G, \quad \text{for all elements } G \in \mathcal{G}, \quad (2.56)$$

where it is customary to define the identity element as the first element in the set \mathcal{G} , *i.e.* $G_0 \equiv E$.

- d) For every element $G \in \mathcal{G}$, there exist an inverse element G^{-1} such that;

$$G^{-1}G = GG^{-1}, \quad \text{for all elements } G \in \mathcal{G}. \quad (2.57)$$

Point a) allows for a multiplication table, which tells us how the combination of elements are interrelated. Additionally such a table can illustrate whether a group is Abelian, *i.e.* $[G_i, G_j] = 0$, or not. Point d) informs that every symmetry operation has an inverse operation. Another important aspect of group theory is that the group \mathcal{G} can be divided further into disjoint conjugation classes K_i . Such classes are defined by all the elements G' that are connected to $G \in \mathcal{G}$ in the following way, see Fig.2.5.;

$$G' = U G U^{-1}, \quad \text{for } U \in \mathcal{G}. \quad (2.58)$$

The physical system under consideration is governed by the BdG Hamiltonian in momentum space $\hat{\mathcal{H}}(\mathbf{k})$, which we know transforms under a symmetry transformation as shown in Eq. 2.30. It is therefore desirable to represent the symmetry operations G through matrix representations $D(G)$, that has be chosen such that $D(G_i G_j) = D(G_i)D(G_j)$.

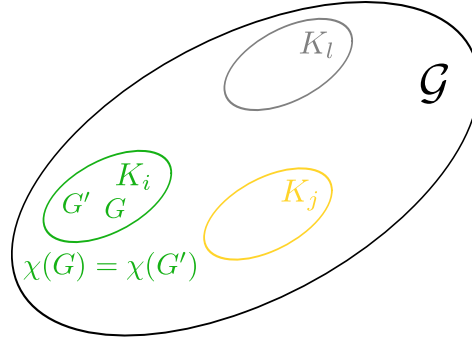


Figure 2.5: Representation of the group \mathcal{G} that has been divided into disjoint conjugation classes. Each element in a class K_i has, by construction, the same character $\chi(G)$.

The matrix representations are not unique, since a matrix $D(G_i)$ equivalently could have been represented through the similarity transformed matrix $U^{-1} D(G_i) U$, or as a direct sum of representations $D(G_i) \oplus D(G_j)$. To circumvent this issue it is customary only to consider irreducible representations (IRs), *i.e.* matrix representations that can not be further block diagonalized and reduced. A matrix representation for the element G_i in the IR Γ_j is usually denoted $D^{\Gamma_j}(G_i)$. Tied to these IRs are the traces of the matrices, also known as characters, $\chi^{\Gamma_j}(G_i) = \text{Tr} D^{\Gamma_j}(G_i)$, since these remain invariant under a change of basis. Note that elements in the same class by construction have the same character (they are all connected by similarity transformations), see again Fig.2.5.

Without specifying the matrix representation, it is possible to construct a character table that includes all the characters for the possible IRs of the group, and how the IRs transform under the symmetry elements. In order to construct this table we will introduce some essential tools. First of all, it can be shown that the dimensionality l_i of the irreducible matrix $D^{\Gamma_i}(G)$ has the property

$$\sum_i l_i^2 = N \quad (2.59)$$

where N is the order of the group. Next, a theorem of great importance is the "*Wonderful Orthogonality Theorem*" for Character,¹ which states the following:

$$\sum_G \chi^{\Gamma_j}(G) \chi^{\Gamma_i}(G^{-1}) = N \delta_{\Gamma_i, \Gamma_j}, \quad (2.60)$$

according to which inequivalent IRs are orthogonal.

In order to exemplify the somewhat abstract statements from above, let us construct the character table for the point group C_{4v} with the elements

$$C_{4v} = \{E, C_4, \bar{C}_4, C_2, \sigma_{xz}, \sigma_{yz}, \sigma_{x=y}, \sigma_{x=-y}\}. \quad (2.61)$$

Here E is the identity operator, C_n is the rotation of $2\pi/n$ about the z -axis, and σ_b is the reflection in the mirror plane b . For visualization of the elements see Fig. 2.6.(a). We first

¹Which follows directly from the "*Wonderful Orthogonality Theorem*" named by Van Vleck [27].

IR	E	$2C_4$	C_2	$2\sigma_v$	$2\sigma_d$	Linear, Rotations	Quadratic
A_1	1	1	1	1	1	z	$x^2 + y^2, z^2$
A_2	1	1	1	-1	-1	R_z	
B_1	1	-1	1	1	-1		$x^2 - y^2$
B_2	1	-1	1	-1	1		xy
E	2	0	-2	0	0	$(x, y), (R_x, R_y)$	(xz, yz)

Table 2.3: Character table for the point group C_{4v} , with the IRs in the first column, and the classes along the first row. We also show polynomial functions transforming according to the IRs.

find the five classes

$$K_1 = E, \quad K_2 = \{C_4, \bar{C}_4\}, \quad K_3 = C_2, \quad K_4 = \{\sigma_{xz}, \sigma_{yz}\}, \quad K_5 = \{\sigma_{x=y}, \sigma_{x=-y}\}, \quad (2.62)$$

which implies that there exists five IRs. Exploiting the fact that the identity element always can be represented as the identity matrix $\mathbf{1}$, which can be reduced to a 1×1 matrix, we know that at least one of the IRs has to be one-dimensional. We thus get the relation for the remaining dimensions of the IRs from Eq.2.59.:

$$\sum_i l_i = 1^2 + l_2^2 + l_3^2 + l_4^2 + l_5^2 = 8, \quad \Rightarrow \quad l_2 = l_3 = l_4 = 1, \quad \text{and} \quad l_5 = 2 \quad (2.63)$$

revealing that we have four one-dimensional IRs and one two-dimensional. The trivial IR, usually denoted A_1 , is easy to construct since it by definition is invariant under the action of all elements, and we therefore get the gray row in Table.2.3. Furthermore, the character for the identity element has to satisfy $\chi^{\Gamma_i}(E) = l_i$, leading the gray column in the same table. By insertion of $\chi^{A_1}(G^{-1})$ in the "Wonderful Orthogonality Theorem for Character" we arrive at the useful relation

$$\sum_G \chi^{\Gamma_i}(G) \chi^{A_1}(G^{-1}) = \sum_G \chi^{\Gamma_i}(G) = 0, \quad (2.64)$$

that, after some combinatorics and orthogonality checks, reveals the final character table seen in Table.2.3. Not all groups are as simple as the C_{4v} , and additional steps might be necessary in the determination of character tables. For a nice stepwise manual see [27] Chap. 3. Note, however, that literature often supplies already determined character tables, see e.g. [49].

With the character table and matrix representation established for the given group, it is possible to rewrite the Hamiltonian in IRs, and classify each term. Let us consider the Hamiltonian

$$\hat{\mathcal{H}}(\mathbf{k}) = \hat{h}^{A_1}(\mathbf{k}) + \hat{h}^{\Gamma}(\mathbf{k}), \quad (2.65)$$

where $\hat{h}^{\Gamma_i}(\mathbf{k})$ is a matrix transforming as the IR Γ_i . If Γ is anything but the trivial IR A_1 , the system no longer belongs to the given point group, but some subgroup of it, since the Hamiltonian is not invariant under all the elements. For an extensive symmetry breaking scheme see Ref. [45].

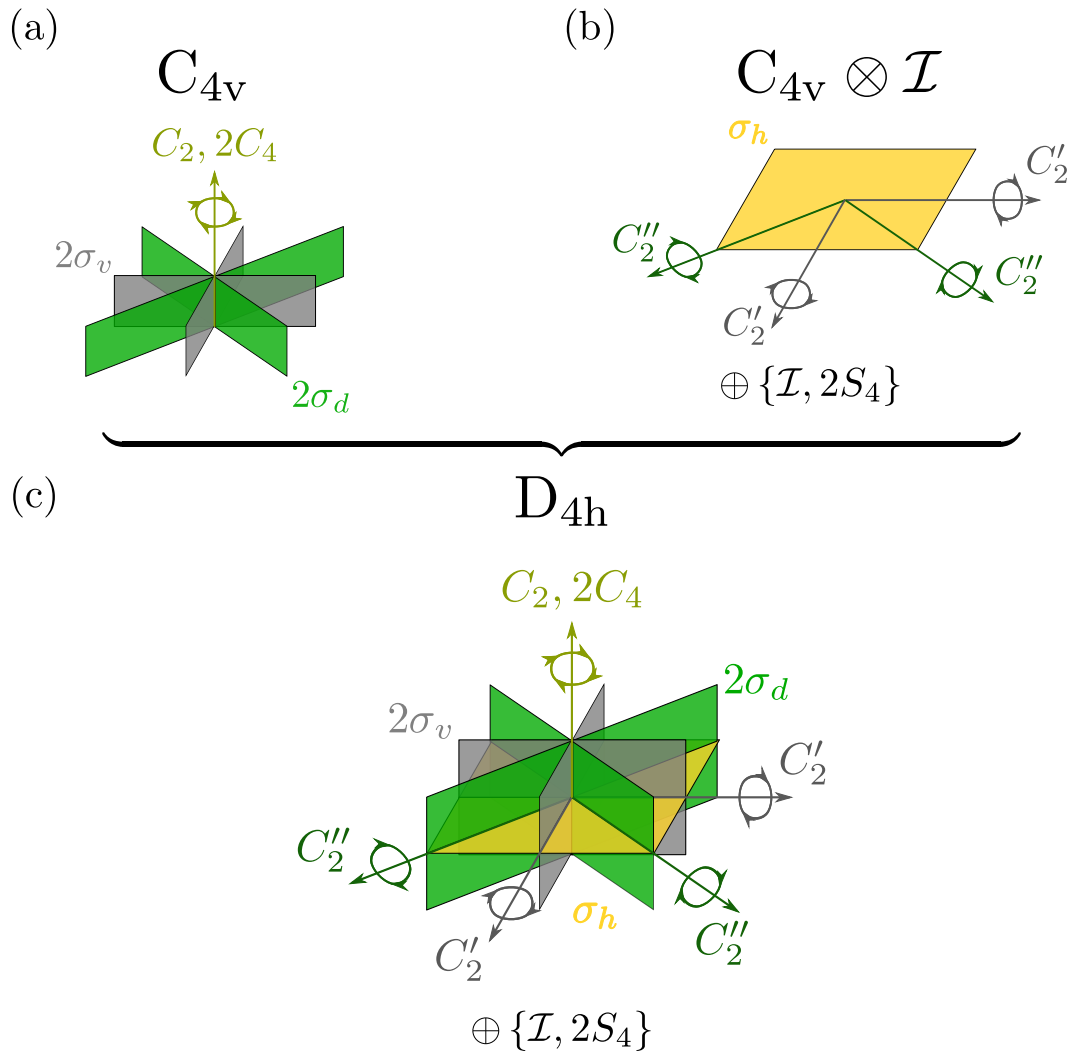


Figure 2.6: (a)-(b) Illustrate the decomposed point group $D_{4h} = C_{4v} \otimes \{E, \mathcal{I}\}$ used in the point group analysis. It is clear that the two decomposed cases, C_{4v} and $C_{4v} \otimes \mathcal{I}$ can be combined to the group D_{4h} in (c). The elements inversion, \mathcal{I} , and improper rotation, S_4 , are not illustrated but simply included as text. The figures were greatly inspired by Ref. [45].

IR	E	$2C_4$	C_2	$2C'_2$	$2C''_2$	\mathcal{I}	$2S_4$	σ_h	$2\sigma_v$	$2\sigma_d$	Linear, Rot.	Quadratic
A_{1g}	1	1	1	1	1	1	1	1	1	1	R_z	$x^2 + y^2, z^2$
A_{2g}	1	1	1	-1	-1	1	1	1	-1	-1		$x^2 - y^2$
B_{1g}	1	-1	1	1	-1	1	-1	1	1	-1		xy
B_{2g}	1	-1	1	-1	1	1	-1	1	-1	1		(xz, yz)
E_g	2	0	-2	0	0	2	0	-2	0	0		(R_x, R_y)
A_{1u}	1	1	1	1	1	-1	-1	-1	-1	-1	z	
A_{2u}	1	1	1	-1	-1	-1	-1	-1	1	1		
B_{1u}	1	-1	1	1	-1	-1	1	-1	-1	1		
B_{2u}	1	-1	1	-1	1	-1	1	-1	1	-1		
E_u	2	0	-2	0	0	-2	0	2	0	0	(x, y)	

Table 2.4: Character table for the point group D_{4h} , with the IRs down the first column, and the classes along the first row. The figure also shows the representative rotations and functions to quadratic order.

Iron-Based Superconductors

After having established the concepts of point groups, the theory will now be applied to the Hamiltonian in Eq.2.48. Where we both will consider μ to be an orbital index, and a band index. The FeSCs belong to the point group D_{4h} . For unified formalism, we will also consider the Hamiltonian, where μ defines a band index, to be D_{4h} invariant as well.

By considering Fig.2.6. it is clear that the point group can be decomposed in the way $D_{4h} = C_{4v} \otimes \{E, \mathcal{I}\}$, with E and \mathcal{I} being the identity and inversion element respectively. The two S_4 elements are improper rotations consisting of a rotation of $\pi/2$, followed by a mirror reflection in the plane perpendicular to the rotation axis. Since the matrix representation of the inversion element already is established in Eq.2.33., we only need to formulate the matrix representation for the elements of C_{4v} . Table.2.3. shows the character table of the group D_{4h} .

Matrix Representation of Group Elements

With the group elements and their physical effects on the system known, as illustrated in Fig. 2.6, it is straightforward to define the matrix representations as done in Sec. 2.2, followed by a classification of the generators of the Hamiltonian. In doing so, one needs to consider the following degrees of freedom for the general Hamiltonian in Eq. 2.48;

- Spin
- Momentum Transfer
- Orbital/Band
- Nambu.

The Hamiltonian has no SOC term, since it is here considered negligible, and the group elements thus leave the spin space inert. Therefore the matrix representation of the point group elements in the identity matrix in spin space. Additionally is the transformation in Nambu space already known from Eq. 2.29, leaving us only with the determination of the

transformation of the wave-vectors and orbitals/bands. However, since the band space has to transform as the trivial IR, since $\widehat{\mathcal{H}}_0(\mathbf{k})$ has to transform as A_{1g} , we can assume the bands to be invariant under all the elements of the group. Thus leaving us with the task of defining the transformations in orbital space, and the effect on the crystal momenta. Starting from the wave-vectors, we know that these transform as vectors;

$$\begin{aligned}
 E\mathbf{k} &= \mathbf{k}, & C_2\mathbf{k} &= -\mathbf{k}, \\
 C_4\mathbf{k} &= (-k_y, k_x), & \overline{C}_4\mathbf{k} &= (k_y, -k_x), \\
 \sigma_{xz}\mathbf{k} &= (k_x, -k_y), & \sigma_{yz}\mathbf{k} &= (-k_x, k_y), \\
 \sigma_{x=y}\mathbf{k} &= (k_y, k_x), & \sigma_{x=-y}\mathbf{k} &= (-k_y, -k_x),
 \end{aligned} \tag{2.66}$$

and similar for the ordering wave-vectors \mathbf{q}_l . However, since the basis includes the star of the ordering wave-vectors² the effects can be captured in the following matrix representations

$$\begin{aligned}
 \hat{d}_{\lambda\rho}(E) &= \mathbb{1}_\lambda \mathbb{1}_\rho & \hat{d}_{\lambda\rho}(C_2) &= \lambda_x \rho_x, \\
 \hat{d}_{\lambda\rho}(C_4) &= \frac{\rho_x + \lambda_x + i\lambda_z \rho_y - i\lambda_y \rho_z}{2}, & \hat{d}_{\lambda\rho}(\overline{C}_4) &= \frac{\rho_x + \lambda_x - i\lambda_z \rho_y + i\lambda_y \rho_z}{2}, \\
 \hat{d}_{\lambda\rho}(\sigma_{xz}) &= \lambda_x & \hat{d}_{\lambda\rho}(\sigma_{yz}) &= \rho_x, \\
 \hat{d}_{\lambda\rho}(\sigma_{x=y}) &= \frac{\mathbb{1}_\lambda \mathbb{1}_\rho + \lambda_x \rho_x + \lambda_y \rho_y + \lambda_z \rho_z}{2}, & \hat{d}_{\lambda\rho}(\sigma_{x=-y}) &= \frac{\mathbb{1}_\lambda \mathbb{1}_\rho + \lambda_x \rho_x - \lambda_y \rho_y - \lambda_z \rho_z}{2}.
 \end{aligned} \tag{2.67}$$

Note that the two momentum-transfer spaces λ and ρ are interrelated and can not be considered separately.

Assuming the band space to transform trivially under all symmetry operations, the resulting matrix representation must simply be $D(G) = \mathbb{1}$, for $G \in C_{4v}$. In orbital space, however, one needs to consider the transformation of each orbital. Exploiting the suggestive nomenclature of the orbitals, it is straightforward to see how each one of the orbitals transforms. Exemplifying this by considering the itinerant $3d$ electrons of the FeSCs, we arrive at the matrix representation (using the basis $\{xz, yz, xy, x^2 - y^2, z^2\}$)

$$\begin{aligned}
 \hat{d}_\kappa(E) &= \mathbb{1}_\kappa & \hat{d}_\kappa(C_2) &= \frac{1}{5}\mathbb{1}_\kappa - \frac{2}{\sqrt{3}}\kappa_8 + \frac{4}{\sqrt{15}}\kappa_{24}, \\
 \hat{d}_\kappa(C_4) &= -\frac{1}{5}\mathbb{1}_\kappa - i\kappa_2 + \frac{1}{\sqrt{3}}\kappa_8 - \kappa_{23} + \frac{1}{\sqrt{15}}\kappa_{24}, & \hat{d}_\kappa(\overline{C}_4) &= -\frac{1}{5}\mathbb{1}_\kappa + i\kappa_2 + \frac{1}{\sqrt{3}}\kappa_8 - \kappa_{23} + \frac{1}{\sqrt{15}}\kappa_{24}, \\
 \hat{d}_\kappa(\sigma_{xz}) &= \frac{1}{5}\mathbb{1}_\kappa + \kappa_3 + \frac{1}{\sqrt{3}}\kappa_8 + \frac{4}{\sqrt{15}}\kappa_{24} & \hat{d}_\kappa(\sigma_{yz}) &= \frac{1}{5}\mathbb{1}_\kappa - \kappa_3 + \frac{1}{\sqrt{3}}\kappa_8 + \frac{4}{\sqrt{15}}\kappa_{24}, \\
 \hat{d}_\kappa(\sigma_{x+y}) &= \frac{1}{5}\mathbb{1}_\kappa + \kappa_1 - \frac{1}{\sqrt{3}}\kappa_8 - \kappa_{23} - \frac{1}{\sqrt{15}}\kappa_{24}, & \hat{d}_\kappa(\sigma_{x-y}) &= \frac{1}{5}\mathbb{1}_\kappa - \kappa_1 - \frac{1}{\sqrt{3}}\kappa_8 - \kappa_{23} - \frac{1}{\sqrt{15}}\kappa_{24}.
 \end{aligned}$$

Where κ denote the $SU(5)$ generators acting in orbital space, defined in App. A. The representation in terms of κ is compact, but unfortunately not transparent. Due to this, we have included the explicit matrix form of the representations in App. D, to get a better physical intuition of each transformation. We are now entitled to combine all the above to get the

²The set of wave vectors that are obtained by applying all the point group elements to the fundamental wave-vector.

final matrix representation of the elements of the group C_{4v} ;

$$\begin{aligned}
 \hat{D}(E) &= \mathbb{1}, \\
 \hat{D}(C_2) &= \left[\frac{1}{5}\mathbb{1}_\kappa - \frac{2}{\sqrt{3}}\kappa_8 + \frac{4}{\sqrt{15}}\kappa_{24} \right] \lambda_x \rho_x, \\
 \hat{D}(C_4) &= \left[-\frac{1}{5}\mathbb{1}_\kappa - i\kappa_2 + \frac{1}{\sqrt{3}}\kappa_8 - \kappa_{23} + \frac{1}{\sqrt{15}}\kappa_{24} \right] \frac{\rho_x + \lambda_x + i\lambda_z \rho_y - i\lambda_y \rho_z}{2}, \\
 \hat{D}(\bar{C}_4) &= \left[-\frac{1}{5}\mathbb{1}_\kappa + i\kappa_2 + \frac{1}{\sqrt{3}}\kappa_8 - \kappa_{23} + \frac{1}{\sqrt{15}}\kappa_{24} \right] \frac{\rho_x + \lambda_x - i\lambda_z \rho_y + i\lambda_y \rho_z}{2}, \\
 \hat{D}(\sigma_{xz}) &= \left[\frac{1}{5}\mathbb{1}_\kappa + \kappa_3 + \frac{1}{\sqrt{3}}\kappa_8 + \frac{4}{\sqrt{15}}\kappa_{24} \right] \lambda_x, \\
 \hat{D}(\sigma_{yz}) &= \left[\frac{1}{5}\mathbb{1}_\kappa - \kappa_3 + \frac{1}{\sqrt{3}}\kappa_8 + \frac{4}{\sqrt{15}}\kappa_{24} \right] \rho_x, \\
 \hat{D}(\sigma_{x+y}) &= \left[\frac{1}{5}\mathbb{1}_\kappa + \kappa_1 - \frac{1}{\sqrt{3}}\kappa_8 - \kappa_{23} - \frac{1}{\sqrt{15}}\kappa_{24} \right] \frac{\mathbb{1}_{\lambda\rho} + \lambda_x \rho_x + \lambda_y \rho_y + \lambda_z \rho_z}{2}, \\
 \hat{D}(\sigma_{x-y}) &= \left[\frac{1}{5}\mathbb{1}_\kappa - \kappa_1 - \frac{1}{\sqrt{3}}\kappa_8 - \kappa_{23} - \frac{1}{\sqrt{15}}\kappa_{24} \right] \frac{\mathbb{1}_{\lambda\rho} + \lambda_x \rho_x - \lambda_y \rho_y - \lambda_z \rho_z}{2}.
 \end{aligned} \tag{2.68}$$

By replacing the matrices in orbital space by identity matrices we retrieve the representation for μ being a band index. We can now take each possible generator of the Hamiltonian, and see how it transforms under the elements of the group. In doing so, we also need to check if the given generators are irreducible or not. We arrive at the table of single IRs in Table.2.5. The IR of combined generators is retrieved from the product table, shown in Table.2.6., *e.g.* $\kappa_{22}\lambda_y\rho_y$ transforms as the IR $B_{1g} \otimes B_{1u} = A_{1u}$. Had the generators been accompanied by a scalar field transforming as the IR Γ , *i.e.* $f^\Gamma(\mathbf{k})\kappa_{22}\lambda_y\rho_y$, the resulting IR would similarly be $\Gamma \otimes A_{1u}$. It is now possible to classify all possible terms arising in the Hamiltonian, and investigate which terms break a symmetry.

Generators	E	$2C_4$	C_2	$2\sigma_v$	$2\sigma_d$	\mathcal{I}	I.R.
τ_x, τ_y, τ_z	1	1	1	1	1	1	A_{1g}
$\kappa_2, \kappa_{18}, (\lambda_y\rho_z - \lambda_z\rho_y)$	1	1	1	-1	-1	1	A_{2g}
κ_{22}	1	-1	1	1	-1	1	B_{1g}
$\kappa_{20}, (\lambda_y\rho_z + \lambda_z\rho_y)$	1	-1	1	-1	1	1	B_{2g}
$(\kappa_5, \kappa_7), (\kappa_{10}, \kappa_{14}), (\kappa_{12}, \kappa_{16}),$ $(\lambda_y, \rho_y), (\lambda_x\rho_y, \lambda_y\rho_x)$	2	0	-2	0	0	2	E_g
κ_{17}	1	1	1	-1	-1	-1	A_{1u}
$\kappa_8, \kappa_{23}, \kappa_{24}, (\lambda_x + \rho_x), \lambda_x\rho_x$	1	1	1	1	1	-1	A_{2u}
$\kappa_1, \kappa_{19}, \lambda_y\rho_y, \lambda_z\rho_z$	1	-1	1	-1	1	-1	B_{1u}
$\kappa_3, \kappa_{21}, (\lambda_x - \rho_x)$	1	-1	1	1	-1	-1	B_{2u}
$(\kappa_4, \kappa_6), (\kappa_9, \kappa_{13}), (\kappa_{11}, \kappa_{15}),$ $(\lambda_z, \rho_z), (\lambda_x\rho_z, \lambda_z\rho_x),$	2	0	-2	2	0	-2	E_u

Table 2.5: The possible IRs in the Hamiltonian. The IRs of combined generators can be found by the means of the product table in Table. 2.6.

\otimes	A_{1g}	A_{2g}	B_{1g}	B_{2g}	E_g	A_{1u}	A_{2u}	B_{1u}	B_{2u}	E_u
A_{1g}	A_{1g}	A_{2g}	B_{1g}	B_{2g}	E_g	A_{1u}	A_{2u}	B_{1u}	B_{2u}	E_u
A_{2g}	A_{2g}	A_{1g}	B_{2g}	B_{1g}	E_g	A_{2u}	A_{1u}	B_{2u}	B_{1u}	E_u
B_{1g}	B_{1g}	B_{2g}	A_{1g}	A_{2g}	E_g	B_{1u}	B_{2u}	A_{1u}	A_{2u}	E_u
B_{2g}	B_{2g}	B_{1g}	A_{2g}	A_{1g}	E_g	B_{2u}	B_{1u}	A_{2u}	A_{1u}	E_u
E_g	E_g	E_g	E_g	E_g	$A_{1g} \oplus A_{2g}$ $\oplus B_{1g} \oplus B_{2g}$	E_u	E_u	E_u	E_u	$A_{1u} \oplus A_{2u}$ $\oplus B_{1u} \oplus B_{2u}$
A_{1u}	A_{1u}	A_{2u}	B_{1u}	B_{2u}	E_u	A_{1g}	A_{2g}	B_{1g}	B_{2g}	E_g
A_{2u}	A_{2u}	A_{1u}	B_{2u}	B_{1u}	E_u	A_{2g}	A_{1g}	B_{2g}	B_{1g}	E_g
B_{1u}	B_{1u}	B_{2u}	A_{1u}	A_{2u}	E_u	B_{1g}	B_{2g}	A_{1g}	A_{2g}	E_g
B_{2u}	B_{2u}	B_{1u}	A_{2u}	A_{1u}	E_u	B_{2g}	B_{1g}	A_{2g}	A_{1g}	E_g
E_u	E_u	E_u	E_u	E_u	$A_{1u} \oplus A_{2u}$ $\oplus B_{1u} \oplus B_{2u}$	E_g	E_g	E_g	E_g	$A_{1g} \oplus A_{2g}$ $\oplus B_{1g} \oplus B_{2g}$

Table 2.6: Product table for the point group D_{4h} . This table can be used to see how two IR generators in Table. 2.5 can be combined into a single IR.

Chapter 3

Topological Phases in 1D Magnetic Superconductors

After having thoroughly performed the topological classification for the wide variety of possible magnetic phases in a magnetic superconductor, Eq. 2.48, see Table. 2.1-2.2, the focus will in the proceeding be aimed at the Double- \mathbf{Q} C_4 -symmetric Spin-Whirl Crystal (\bullet) phase:

$$\widehat{\mathbf{M}}(\mathbf{r}) = \widehat{M}_x [\cos(\mathbf{Q}_1 \cdot \mathbf{r}) + \cos(\mathbf{Q}_2 \cdot \mathbf{r})] \sigma_x + \widehat{M}_\perp [\sin(\mathbf{Q}_2 \cdot \mathbf{r}) \sigma_y + \sin(\mathbf{Q}_1 \cdot \mathbf{r}) \sigma_z]. \quad (3.1)$$

This magnetic texture is interesting since it can render the system in of the three Majorana classes, BDI, D and DIII, where the former is achieved through dimensional reduction resulting in a magnetic helix phase (\bullet). The system belongs to the classes DIII (D) for a real (complex) superconducting order parameter. However, as we will discuss later, the class D is also accessible for a real superconducting order parameter by inclusion of a magnetic field. We can thus limit our analysis to real superconducting OPs, and still achieve the three Majorana classes.

Since a brute-force study of the topological phases of the five-orbital Hamiltonian, Eq. 2.48, in an incommensurate phase is a demanding task, a bottom-up approach will be applied. We will thus start from a simple Single-Band Model (1BM) in 1D, followed by the extension to a Two-Band Model (2BM). The extension to two bands is in order to capture the essence of nesting between different pockets, as will become more clear in the 2D models in Chap.4. A dimensional reduction of Eq.3.1 leaves the magnetic texture as a general isotropic helix(\bullet). The simplest commensurate ordering wave-vector that supports such modulation is $Q = \frac{3\pi}{2a} \equiv \frac{\pi}{2a}$, with a periodicity of four lattice sites. A ordering wave vector of the usual commensurate type, $Q = \pi/a$ will simply result in the usual single- \mathbf{Q} magnetic stripe phase. The simplification of assuming a commensurate ordering wave-vector allows us to consider the system exactly, since we do not need to make any approximations in order to get a closed set of equations, as it is the case for the incommensurate phases in Chap. 2. This simplification does not violate the topological properties of the system, since these are solely determined by the magnetic texture, and not the magnetic ordering wave-vector, as can be seen from Eq.1.10 which belongs to the class BDI for an, in general, incommensurate wave-vector. Lastly we will in the following keep the superconducting OPs at the minimal s -wave form, in order to make the whole process simple and transparent.

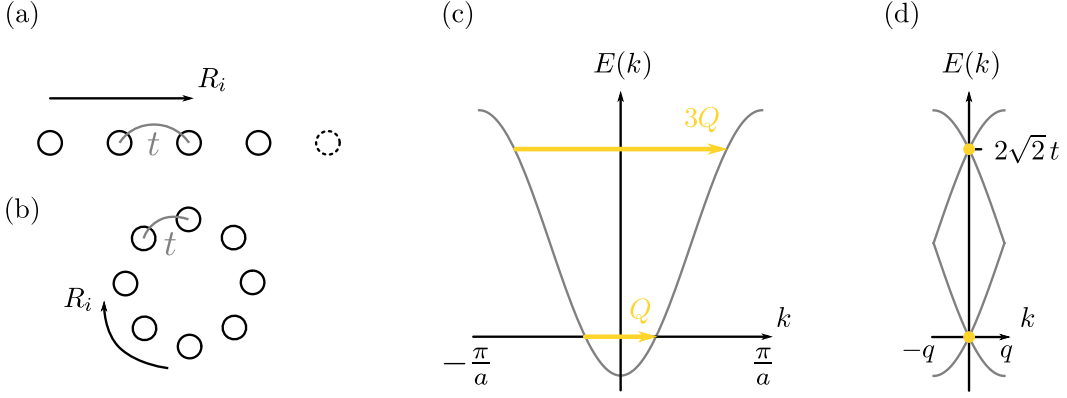


Figure 3.1: (a) Real space representation of the Single-Band Model introduced in Eq. 3.2. (b) The system can be viewed as a ring of atoms when imposing periodic boundary conditions. (c) Shows the band structure in the first BZ, with the nesting vectors indicated by yellow arrows. (d) Shows the RBZ after foldings with respect to Q . The nested points, k_{NP} , are indicated by yellow dots.

3.1 Single-Band Model

For the simple 1BM consider the tight-binding Hamiltonian of an electron with nearest neighbor hopping, moving in an anisotropic helical magnetic field:

$$H = \sum_{ij} \hat{d}_i^\dagger [-t\delta_{j,i\pm a} + \mu\delta_{i,j} + M_x \cos(QR_i)\delta_{i,j}\sigma_x + M_\perp \sin(QR_i)\delta_{i,j}\sigma_y] \hat{d}_j \quad (3.2)$$

where a is the lattice constant, and $\hat{d}_i = (d_{i\uparrow}, d_{i\downarrow})^\top$. This Hamiltonian is nothing but a lattice version of the Hamiltonian in Eq.1.9., with an anisotropic magnetic helix. If we were to define the Hamiltonian in Bloch space, we need to define the momentum transfer spaces in 1D, similar to the formalism in Eq. 2.48. Additionally, since the RBZ will reign from $k \in (-q, q]$, we would need to include an extra momentum transfer space in the way

$$\eta : \{k, k - 4q\}, \quad \rho : \{k + q, k - q\} \quad (3.3)$$

to cover the old BZ. The single-particle Hamiltonian in Bloch space becomes

$$\hat{h}(k) = h_0^+(k) + h_1^+(k)\eta_z + h_2^-(k)\rho_z + h_3^-(k)\eta_z\rho_z + \frac{M_x\rho_x\sigma_x + M_\perp\rho_y\sigma_y}{2} + \eta_x \frac{M_x\rho_x\sigma_x - M_\perp\rho_y\sigma_y}{2}, \quad (3.4)$$

where $h_i^s(k)$ is, as usual, linear combinations of ξ_k shifted by appropriate momenta. Note that a rotation in spin space can be performed in order to connect to the dimensional reduced system in the perpendicular direction. We have in Fig. 3.1.(a) shown the real space representation of the hopping matrix elements. When imposing periodic boundary conditions the chain of atoms can be viewed as a ring, Fig. 3.1.(b). In Fig. 3.1.(c) we show the band structure, $\xi_k = -2t \cos(k) + \mu$, in the first BZ. Here the chemical potential has been tuned such that nesting takes place at the Fermi level, $\mu = \sqrt{2}t$, as indicated by the yellow arrow. It is evident from this figure, that nesting also takes place at finite energy (note that $3Q \equiv -Q$). Lastly the RBZ is shown in Fig. 3.1.(d) where the yellow points are the nested points $k_{\text{NP}} \in \text{RBZ}$.

Single-Band Model in the Isotropic Helix Phase

Adopting the relation for the magnetic moments magnitudes, see Eq. 2.50, we must be in the isotropic phase when $M_x = M_\perp = M/2$. A peculiar feature for this phase is that the Hamiltonian easily can be simplified through a unitary transformation, as seen in Eq. 1.9 and Fig. 1.3.(b)-(c). The Hamiltonian takes the form

$$\begin{aligned} H &= \sum_{ij} \hat{d}_i^\dagger \left[-t\delta_{j,i\pm a} + \mu\delta_{i,j} + \frac{M\delta_{ij}(\cos(QR_i)\sigma_x + \sin(QR_i)\sigma_y)}{2} \right] \hat{d}_j \\ &= \sum_{ij} \hat{d}_i^\dagger e^{-iqR_i\sigma_z} \left[-e^{iqR_i\sigma_z} t\delta_{j,i\pm a} e^{-iqR_j\sigma_z} + \mu\delta_{i,j} + \frac{M\delta_{ij}\sigma_x}{2} \right] e^{iqR_j\sigma_z} \hat{d}_j, \end{aligned} \quad (3.5)$$

allowing us to avoid the use of the momentum transfer spaces ρ and η when transforming to Bloch space. The single particle Hamiltonian, after the inclusion of an s -wave superconducting OP, takes the following form in Bloch space

$$\begin{aligned} \hat{\mathcal{H}}(k) &= \tau_z \xi_{k-q\sigma_z} + \frac{M\sigma_x}{2} + \Delta\tau_x \\ &= \tau_z (\xi_k^+ + \xi_k^- \sigma_z) + \frac{M\sigma_x}{2} + \Delta\tau_x, \end{aligned} \quad (3.6)$$

where the spinor has been extended to the BdG spinor $\hat{\Psi}_k^\dagger = (\hat{d}_k^\dagger, -i\hat{d}_{-k}^\dagger \sigma_y)$, with the spin-rotated hole component. Note that the latter equality is true since the dispersion ξ_k is even under inversion, and can be split up as follows

$$\xi_{k-q\sigma_z} = \xi_k^+ + \xi_k^- \sigma_z \quad (3.7)$$

with the superscripts indicating the symmetry under inversion. The Hamiltonian belongs to the class BDI as expected from Table. 2.2 and Chap. 1, with the symmetries $\Theta = \sigma_x \mathcal{K}$, $\Xi = \tau_y \sigma_y \mathcal{K}$ and $\Pi = \tau_y \sigma_z$. As discussed in the beginning of this chapter, a complex superconducting order parameter can render the Hamiltonian to be in the class D. But, as it is clear from the given symmetries, the Hamiltonian can make the same transition by including a magnetic field $\hat{\mathcal{H}}_z = \mathbf{B} \cdot \boldsymbol{\sigma}$, which breaks Θ and Π .

The presence of chiral symmetry allows us to calculate the winding invariant through the procedure discussed in Sec. 1.6. The unitary operator $\hat{U} = (\tau_y \sigma_z + \tau_z)/\sqrt{2}$ brings Eq. 3.6. on the desired off diagonal form

$$\hat{U}^\dagger \hat{\mathcal{H}}(k) \hat{U} = \begin{pmatrix} 0 & \hat{A}(k) \\ \hat{A}^\dagger(k) & 0 \end{pmatrix}, \quad \hat{A}(k) = -i(\xi_k^+ \sigma_z + \xi_k^-) - \frac{M\sigma_y}{2} - \Delta. \quad (3.8)$$

The parametrizing vector $\mathbf{d}(k)$ thus becomes

$$d_x(k) = \text{Re} [\text{Det}[\hat{A}(k)]] = (\xi_k^+)^2 - (\xi_k^-)^2 - \frac{M^2}{4} + \Delta^2 \quad (3.9a)$$

$$d_y(k) = \text{Im} [\text{Det}[\hat{A}(k)]] = 2\xi_k^- \Delta. \quad (3.9b)$$

From the parametrizing vector we can extract an important relation for the nested points k_{NP} , fulfilling $\xi_{k_{\text{NP}\pm q}} = \xi_{k_{\text{NP}\mp q}}$, and the gap closing points k_{GC} , namely that they coincide, $k_{\text{NP}} \equiv k_{\text{GC}}$ (the yellow dots in Fig. 3.1.(d)). In order to show this, we know that gap closings

must occur whenever $\mathbf{d}(k) = \mathbf{0}$, since the unit vector $\bar{\mathbf{d}}(k)$ will diverge, resulting in an ill-defined topological invariant. We observe that the component $d_y(k)$ is vanishing for $\xi_k^- = 0$, since the superconducting s -wave gap always is non-zero. We thus find that gap closings take place at the wave-vectors fulfilling

$$\xi_{k_{GC}}^- = 0. \quad (3.10)$$

These wave-vectors are exactly the same satisfying the condition for nesting, as can be seen in the relation

$$\xi_{k_{GC} \pm q} = \xi_{k_{GC} \mp q} \quad \Rightarrow \quad \cancel{\xi_{k_{GC}}^+} \mp \xi_{k_{GC}}^- = \cancel{\xi_{k_{GC}}^+} \pm \xi_{k_{GC}}^-, \quad (3.11)$$

which yields $k_{GC} \equiv k_{NP}$. Now that the gap closing points are known, we can determine the criteria for gap closing by solving $d_x(k_{NP}) = 0$, leaving us with

$$M = \pm 2\sqrt{\Delta^2 + (\xi_{k_{NP}}^+)^2} \equiv \pm 2\sqrt{\Delta^2 + \xi_{NP}^2}. \quad (3.12)$$

We have defined $\xi_{NP} = \xi_{k_{NP}}^+ = \xi_{k_{NP} \pm q}$ as the energy at the nested point. For the 1BM the energies at the nested points are $\xi_{NP} = \{0, 2\sqrt{2}t\}$, as indicated by the yellow dots in Fig. 3.1.(d). The knowledge of the nested points can furthermore be used to linearize $\mathbf{d}(k)$ about the nested points, since the main contributions of the winding number stem from these. For our 1BM we have $k_{NP} = \{0, \pi/a\}$ for $k \in \text{BZ}$, obtained from Eq.3.11. After a linearization we arrive at

$$d_x(k) \approx \xi_{NP}^2 - \frac{M^2}{4} + \Delta^2, \quad d_y(k) \approx 2\Delta v_{NP}k. \quad (3.13)$$

where the expansion coefficients are defined as

$$\xi_k^+ \approx \xi_{NP}, \quad \xi_k^- \approx v_{NP}k, \quad (3.14)$$

where it is clear that ξ_{NP} and v_{NP} both are functions of the nested points k_{NP} . The winding is then easily found to be

$$w = \sum_{k_{NP} \in \text{BZ}} \text{Sign}[\Delta v_{NP}] \frac{\text{Sign}\left[\frac{M^2}{4} - \Delta^2 - \xi_{NP}^2\right]}{2}. \quad (3.15)$$

Finally inserting the parameters for the 1BM, with $\text{Sign}[v_{NP}] = \{+1, -1\}$, one arrives at

$$w = \text{Sign}[\Delta] \frac{\text{Sign}\left[\frac{M^2}{4} - \Delta^2\right] - \left[\frac{M^2}{4} - \Delta^2 - 8t^2\right]}{2}. \quad (3.16)$$

The invariant reveals that the system is in a topological non-trivial phase for $2\Delta < M < 2\sqrt{\Delta^2 + 8t^2}$, with a single Majorana fermion per end when opening the ring in Fig. 3.1.(b).

Single-Band Model in the Anisotropic Helix Phase

Extending the analysis from the section above to a more general magnetic phase, namely the anisotropic magnetic helix, one can not perform the unitary transformation of Eq. 1.9 in real

space, and therefore needs to fold to the RBZ and include the additional momentum transfer spaces defined in Eq. 3.3,

$$\begin{aligned} \widehat{\mathcal{H}}(k) = & \tau_z (h_0^+(k) + h_1^+(k)\eta_z + h_2^-(k)\rho_z + h_3^-(k)\eta_z\rho_z) \\ & + \frac{M_x\rho_x\sigma_x + M_\perp\rho_y\sigma_y}{2} + \eta_x \frac{M_x\rho_x\sigma_x - M_\perp\rho_y\sigma_y}{2} + \Delta\tau_x \end{aligned} \quad (3.17)$$

with the following spinor of the system

$$\widehat{\Psi}_k^\dagger = \left(\Psi_k^\dagger, -i\Psi_{-k}^\dagger\rho_x\sigma_y \right), \quad \Psi_k^\dagger = \left(\hat{d}_{k+q}^\dagger, \hat{d}_{k-q}^\dagger, \hat{d}_{k-3q}^\dagger, \hat{d}_{k+3q}^\dagger \right). \quad (3.18)$$

In this formalism complex conjugation acquires the form $\mathcal{K} = \rho_x\mathcal{K}'$, in correspondence to a dimensionally reduced complex conjugation operation defined for Eq. 2.48. The single particle Hamiltonian acquires the unitary symmetry $\rho_z\sigma_z$, which allows for a block diagonalization by means of the operator $\widehat{\mathcal{O}} = (\rho_z\sigma_z + \sigma_x)/\sqrt{2}$

$$\begin{aligned} \widehat{\mathcal{O}}^\dagger\widehat{\mathcal{H}}(k)\widehat{\mathcal{O}} = & \tau_z (h_0^+(k) + h_1^+(k)\eta_z + h_2^-(k)\rho_z + h_3^-(k)\eta_z\rho_z) \\ & + \rho_x \frac{M_x\sigma - M_\perp}{2} + \eta_x\rho_x \frac{M_x\sigma + M_\perp}{2} + \Delta\tau_x, \end{aligned} \quad (3.19)$$

where $\sigma = \pm 1$ are the eigenvalues of σ_x . The block diagonal Hamiltonian $\widehat{\mathcal{H}}^{\sigma=1}(k) \oplus \widehat{\mathcal{H}}^{\sigma=-1}(k)$ belongs to the symmetry class $\text{BDI} \oplus \text{BDI}$ with the symmetries $\Theta = \rho_x\mathcal{K}'$, $\Xi = \tau_y\rho_y\mathcal{K}'$ and $\Pi = \tau_y\rho_z$. It is now possible to classify each block and define its corresponding invariant w^σ . The chiral symmetry allows for the block off-diagonalization through $\widehat{U} = (\tau_y\rho_z + \tau_z)/\sqrt{2}$

$$\widehat{U}^\dagger\widehat{\mathcal{H}}^\sigma(k)\widehat{U} = \begin{pmatrix} 0 & \hat{A}^\sigma(k) \\ (\hat{A}^\sigma(k))^\dagger & 0 \end{pmatrix}, \quad (3.20a)$$

with the matrix

$$\begin{aligned} \hat{A}^\sigma(k) = & -i (h_0^+(k)\rho_z + h_1^+(k)\eta_z\rho_z + h_2^-(k) + h_3^-(k)\eta_z) \\ & - \rho_y \frac{M_x\sigma - M_\perp}{2} - \eta_x\rho_y \frac{M_x\sigma + M_\perp}{2} - \Delta. \end{aligned} \quad (3.20b)$$

If we next consider the 1BM, we see that we have a single gap closing point at $k_{\text{NP}} = 0$ for $k \in \text{RBZ}$, as seen in Fig. 3.1.(d). We can thus once again linearize about this point to get

$$h_0^+(k) \approx \sqrt{2}t, \quad h_1^+(k) \approx -\sqrt{2}t, \quad (3.21a)$$

$$h_2^-(k) \approx 0, \quad h_3^-(k) \approx -\sqrt{2}tk. \quad (3.21b)$$

This results in the parametrizing vector $\mathbf{d}^\sigma(k)$ with the components

$$d_x^\sigma(k) = (M_x^2 - \Delta^2)(M_\perp^2 - \Delta^2) + 2t^2(4\Delta^2 - [M_x - \sigma M_\perp]^2) \quad (3.22a)$$

$$d_y^\sigma(k) = -16\sqrt{2}t^3\Delta k, \quad (3.22b)$$

with the resulting invariant for each block

$$w^\sigma = \text{Sign}[t\Delta] \frac{\text{Sign} \left[(M_x^2 - \Delta^2)(M_\perp^2 - \Delta^2) + 2t^2(4\Delta^2 - [M_x - \sigma M_\perp]^2) \right]}{2}. \quad (3.23)$$

The invariants w^σ can now be combined into one single invariant w , which has to coincide with Eq. 3.16 obtained for an isotropic helix in the limit $M_x = M_\perp = M/2$. There are several

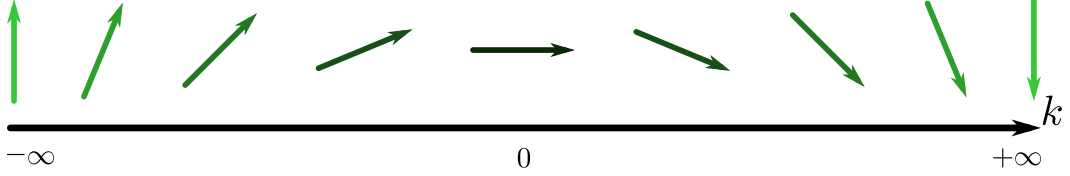


Figure 3.2: The winding of the parameterizing vectors $\bar{\mathbf{d}}^\sigma(k)$ of k . This figure clearly illustrates that the parameterizing vectors can not be compactified. We have in the figure assumed $\text{Sign}[d_x^\sigma(k)] = +1$ and $\text{Sign}[t\Delta] = +1$.

routes to determine the combination of the windings: one can plot the windings in parameter space in the isotropic helix limit, and see how these should be combined to coincide with the parameter space of Eq. 3.16. Alternatively one can approach this algebraically, again in the isotropic helix limit;

$$\begin{aligned}
 w^{\sigma=+1} \pm w^{\sigma=-1} &= \frac{\text{Sign} \left[\left(\frac{M^2}{4} - \Delta^2 \right)^2 + 8t^2\Delta^2 \right] \pm \text{Sign} \left[\left(\frac{M^2}{4} - \Delta^2 \right)^2 + 8t^2\Delta^2 - 2t^2M^2 \right]}{2} \\
 &= \frac{1 \pm \text{Sign} \left[\left(\frac{M^2}{4} - \Delta^2 \right) \left(\frac{M^2}{4} - \Delta^2 - 8t^2 \right) \right]}{2} \\
 &= \frac{\text{Sign} \left[\frac{M^2}{4} - \Delta^2 \right] \pm \text{Sign} \left[\frac{M^2}{4} - \Delta^2 - 8t^2 \right]}{2},
 \end{aligned} \tag{3.24}$$

where we have assumed $t\Delta > 0$. Lastly one could include an infinitesimal term, which breaks the unitary symmetry $\rho_z\sigma_z$, and do a determination of the invariant of the total Hamiltonian $\hat{\mathcal{H}}(k)$. Followed by letting the infinitesimal symmetry breaking term go to zero, and see how this result is related to the winding of the two blocks w^σ . It is of great importance that the infinitesimal symmetry-breaking term only breaks the symmetry $\rho_z\sigma_z$, and not any other. From the algebraic method shown, it is clear that the total winding must be

$$w = w^{\sigma=+1} - w^{\sigma=-1}. \tag{3.25}$$

The unintuitive combination of windings is due to the fact that the parametrizing vectors $\bar{\mathbf{d}}^\sigma(k)$ do not have the same value at the RBZ boundaries, *i.e.* they are not compactified. This means that the winding of each block does not constitute a topological invariant, since they cannot cover the S^1 sphere alone, but only in combination [50]. To illustrate the behavior of the parametrizing vectors, we have illustrated the winding of $\bar{\mathbf{d}}^\sigma(k)$ in Fig. 3.2, as a function of momentum, with $k \in [-\infty, +\infty)$, since $\bar{\mathbf{d}}^\sigma(k)$ has been linearized. This figure clearly illustrates that $\bar{\mathbf{d}}^\sigma(k)$ cannot be compactified, and their respective windings are therefore not topological invariants.

We have plotted the topological phase diagrams for different values of Λ in Fig. 3.3.(a), where Λ connects the two magnitudes in the way

$$M_x = M \sin(\Lambda)/\sqrt{2}, \quad M_\perp = M \cos(\Lambda)/\sqrt{2}. \tag{3.26}$$

For the yellow regions in the phase diagram we find $w = 1$, and thus we expect one MF localized at each end of the open system. In Fig. 3.3.(b) we show the gap closings and re-openings of the bandstructure for a path in parameter space (I-VI), in the case of anisotropic

magnetic helix with $\Lambda = \frac{\pi}{8}$. Lastly, Fig.3.3.(c) depicts the absolute square of the real space Majorana wave functions for an asymmetric spiral with $\Lambda = \pi/8$.

Low Energy Projection of Single-Band Model

The calculations carried out in the above sections are exact, since the Hamiltonian has the simple form in Eq. 3.17. Had the Hamiltonian been of a more complicated structure, or simply of greater dimensionality, one could do a low energy projection. Such a projection is not necessary in this chapter, however, we will simply outline the procedure, so it is clearer for more complicated systems discussed later. As we know, gap closings take place at the nested points k_{NP} , where the 1BM has the following energies at the nested points $\xi_{\text{NP}} = \{0, 2\sqrt{2}t\}$. It is desired to get an effective low energy Hamiltonian, which describes the nested points at the Fermi level $\xi_{\text{NP}} = 0$, without including the higher energy contributions. This can be done by finding the bands that partake in the nesting at the Fermi level, and project the Hamiltonian onto these, *i.e.* the states fulfilling

$$\hat{\mathcal{H}}_0(\mathbf{k}_{\text{NP}})|\nu \mathbf{k}_{\text{NP}}\rangle = 0. \quad (3.27)$$

For the given 1BM the low energy state is $|\eta_z = +1\rangle$, resulting in the low energy Hamiltonian

$$\hat{\mathcal{H}}^{l\sigma}(\mathbf{k}) = \tau_z \left(\frac{\xi_{k+q} + \xi_{k-q}}{2} + \frac{\xi_{k+q} - \xi_{k-q}}{2} \rho_z \right) + \rho_x \frac{M_x \sigma - M_{\perp}}{2} + \Delta \tau_x. \quad (3.28)$$

We find the winding number to be

$$w^{\sigma} = \text{Sign}[\Delta] \frac{\text{Sign} \left[\left(\frac{M_x \sigma - M_{\perp}}{2} \right)^2 - \Delta^2 \right]}{2}. \quad (3.29)$$

The above result simply tells us that, in the isotropic helix case, the system is in a topological non-trivial phase when $M > 2\Delta$. This coincides with the exact invariant calculated in Eq.3.16, however, we do not capture the upper bound of the topological phase, *i.e.* $M < 2\sqrt{\Delta^2 + 8t^2}$, since the gap closing driving the system into a trivial phase has been projected out. This approximation scheme is of course only valid for $M/(2\sqrt{2}t) \ll 1$, *i.e.* magnetic gaps less than the high energy at the nested point. If $M \sim 2\sqrt{2}t$ the high energy nested bands start to generate gap closings.

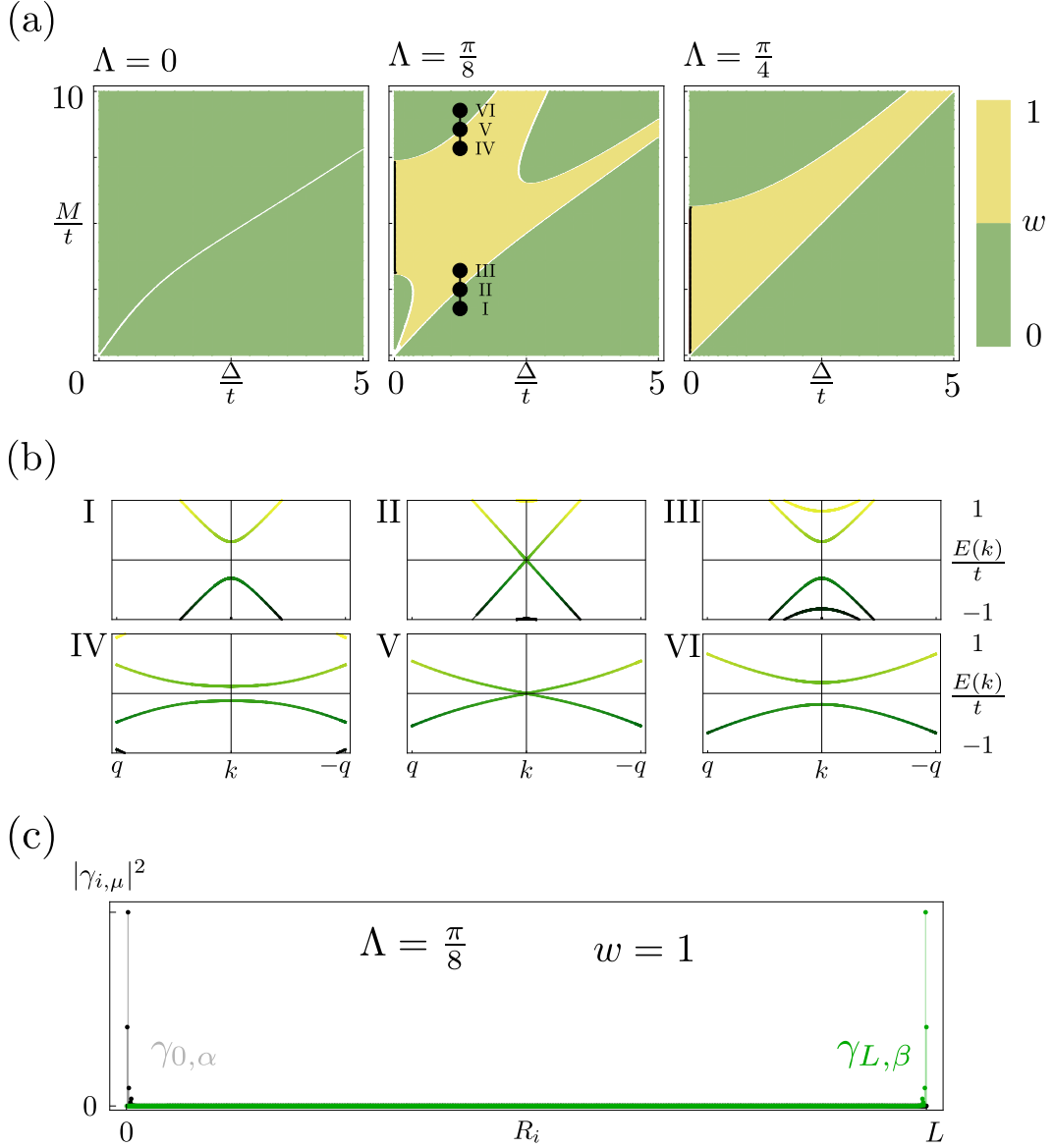


Figure 3.3: (a) Shows the topological phase diagram for different magnetic helicities for different Λ . (b) Depicts the gap structure and how it changes for a sweep in parameter space from I-VI. (c) Shows a real space calculation of the Majorana wave functions in the topological non-trivial phase. The length of the chain is $L = 1000 a$, where a is the lattice constant.

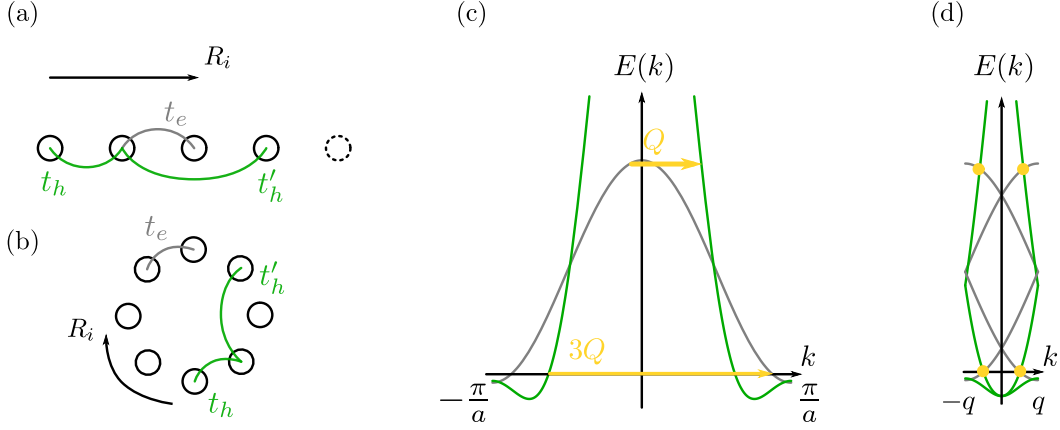


Figure 3.4: (a) Real space representation of the Two-Band Model introduced in Eq.3.30. (b) The system can be viewed as a ring of atoms when imposing PBCs. (c) Shows the band structure in the first BZ, with the nesting vectors indicated by yellow arrows. (d) Shows the RBZ after a folding with respect to Q . The nested points, k_{NP} , are indicated by yellow dots. Note that we in (c) only have shown one set of nested points, even though the system also has nested points that are connected by inversion to the ones shown.

3.2 Two-Band Model

With the theory for the 1BM in 1D established, we are now ready to extend to the 2BM in 1D, and see how an additional band modifies the symmetries and topological phases of the system. The inclusion of an additional band results in the real space Hamiltonian

$$H = \sum_{ij} \hat{d}_i^\dagger \left[\frac{\hat{t}}{2} \delta_{j,i\pm a} + \hat{t}' \left(\frac{\delta_{j,i\pm 2a}}{2} + \delta_{i,j} \right) - \hat{\epsilon} \delta_{i,j} + \kappa_x M_x \delta_{i,j} \cos(QR_i) \sigma_x + \kappa_x M_\perp \delta_{i,j} \sin(QR_i) \sigma_y \right] \hat{d}_j \quad (3.30)$$

where the hopping parameters, magnetic order parameters and on-site energies now are matrices in band space spanned by $\{\mathbf{1}_\kappa, \kappa_x, \kappa_y, \kappa_z\}$;

$$\hat{t} = \frac{t_e + t_h}{2} + \frac{t_e - t_h}{2} \kappa_z, \quad \hat{t}' = t'_h \frac{\mathbf{1}_\kappa - \kappa_z}{2}, \quad \hat{\epsilon} = \frac{\epsilon_e + \epsilon_h}{2} + \frac{\epsilon_e - \epsilon_h}{2} \kappa_z. \quad (3.31)$$

with e and h labeling the two bands. We have chosen the magnetic order parameter to be strictly inter-band, since the inclusion of the additional band is done so to capture the effect of nesting between different pockets in a 2D system, similar to Fig.2.2.(b). In order to generate nesting at the Fermi level, we have tuned the parameters as shown in Table.3.1. The choice of the 2BM seems rather arbitrary, but reproduces a FS in 2D somewhat similar to the FS of the five-orbital model in [39]. It has the desired electron pockets at the high symmetry points X and Y , and hole pockets at Γ and M , as will become evident for the 2BM in 2D. A transformation to Bloch space gives a Hamiltonian of the form in Eq.3.4, but with the terms being matrices in band space, and with the two band dispersions

$$\xi_k^e = t_e \cos(k) - \epsilon_e, \quad \xi_k^h = t_h \cos(k) + t'_h [\cos(2k) + 1] - \epsilon_h. \quad (3.32)$$

Parameter	Value [t_e]
t_h	2.86
t'_h	1
ϵ_e	-0.92
ϵ_h	-0.80

Table 3.1: Values of parameters in units of t_e , in order to achieve nesting at the Fermi level.

Fig.3.4.(a)-(b) show the real space representation of the hopping matrix elements with PBCs. In Fig. 3.4.(c) we have shown the band structure for the two distinct bands; green for the band labeled by h , and gray for the band labeled by e . The nested points are indicated by arrows, and we note that the inclusion of an extra band allows yet another set of nested points, namely the inversion transformed counterparts of the ones shown in the figure. Lastly is the folded band structure shown in Fig.3.4.(d), where we again have illustrated all the set of nested points by yellow dots.

Two-Band Model in the Isotopic Helix Phase

Once again the isotropic helix allows for the unitary transformation as in Eq. 3.5;

$$H = \sum_{ij} \hat{d}_i^\dagger e^{-iqR_i\sigma_z} \left[e^{iqR_i\sigma_z} \left(\hat{t} \delta_{j,i\pm a} + \hat{t}' \left(\frac{\delta_{j,i\pm 2a}}{2} + \delta_{i,j} \right) \right) e^{-iqR_i\sigma_z} - \hat{\epsilon} \delta_{i,j} + \frac{M\kappa_x\sigma_x}{2} \delta_{i,j} \right] e^{iqR_j\sigma_z} \hat{d}_j \quad (3.33)$$

where we have used the spinor $\hat{d}_i = (\hat{d}_{ie}, \hat{d}_{ih})^\top = (d_{ie\uparrow}, d_{ie\downarrow}, d_{ih\uparrow}, d_{ih\downarrow})^\top$. Including the pairing potential, followed by a transformation to Bloch space, we arrive at

$$\hat{\mathcal{H}}(k) = \tau_z \left[\frac{\xi_k^{e+} + \xi_k^{h+}}{2} + \frac{\xi_k^{e+} - \xi_k^{h+}}{2} \kappa_z \right] + \tau_z \left[\frac{\xi_k^{e-} + \xi_k^{h-}}{2} + \frac{\xi_k^{e-} - \xi_k^{h-}}{2} \kappa_z \right] \sigma_z + \frac{M\kappa_x\sigma_x}{2} + \Delta\tau_x. \quad (3.34)$$

where Eq.3.7. was applied to the dispersions ξ_k^μ , with $\mu = \{e, h\}$. We already see here that, the band degree of freedom allows for the symmetry $\kappa_z\sigma_z$, which splits the Hamiltonian into the two blocks labeled by σ , after a unitary transformation with the operator $\hat{\mathcal{O}} = (\kappa_z\sigma_z + \sigma_x)/\sqrt{2}$;

$$\hat{\mathcal{H}}^\sigma(k) = \tau_z \left[\frac{\xi_k^{e+} + \xi_k^{h+}}{2} + \frac{\xi_k^{e+} - \xi_k^{h+}}{2} \kappa_z \right] + \sigma\tau_z \left[\frac{\xi_k^{e-} + \xi_k^{h-}}{2} \kappa_z + \frac{\xi_k^{e-} - \xi_k^{h-}}{2} \right] + \frac{\sigma M\kappa_x}{2} + \Delta\tau_x. \quad (3.35)$$

The momentum transfer spaces are not included, and complex conjugation operation must be the usual \mathcal{K} . We observe that the second term in the Hamiltonian breaks the generalized time-reversal symmetry Θ , and the generalized charge conjugation symmetry Ξ , but leaves a chiral symmetry $\Pi = \tau_y\kappa_z$, resulting in the class AIII \oplus AIII. By inspection of Table.2.2, one

would be surprised that this symmetry class emerges, but this is simply because the system has a symmetry due to the band degree of freedom, whereas in the classification in Sec. 2.3 it was assumed that the band/orbital matrices had a random form. Even though each block of the Hamiltonian do not support MFs, a combination of the two does. As we will see later in this section, the Hamiltonian has a symmetry ensuring the occurrence of a pair of topologically protected states at each edge when the system is in the topologically non-trivial phase. These two states can be combined into two real wave functions, *i.e.* MFs.

Once again the chiral symmetry allows for block off-diagonalization, through the unitary operator $\hat{U} = (\tau_y \kappa_z + \tau_z) / \sqrt{2}$

$$\hat{U}^\dagger \hat{\mathcal{H}}^\sigma(k) \hat{U} = \begin{pmatrix} 0 & \hat{A}^\sigma(k) \\ (\hat{A}^\sigma)^\dagger(k) & 0 \end{pmatrix}, \quad \hat{A}^\sigma(k) = -i(\varepsilon_{k,0}^\sigma + \varepsilon_{k,1}^\sigma \kappa_z) - \frac{\sigma M \kappa_y}{2} - \Delta, \quad (3.36)$$

where, for brevity, the following was defined

$$\varepsilon_{k,0}^\sigma = \frac{\xi_k^{e+} - \xi_k^{h+}}{2} + \sigma \frac{\xi_k^{e-} + \xi_k^{h-}}{2}, \quad \varepsilon_{k,1}^\sigma = \frac{\xi_k^{e+} + \xi_k^{h+}}{2} + \sigma \frac{\xi_k^{e-} - \xi_k^{h-}}{2}, \quad (3.37)$$

which leads to the parametrizing vector $\mathbf{d}(k)$, with the components

$$d_x^\sigma(k) = (\varepsilon_{k,1}^\sigma)^2 - (\varepsilon_{k,0}^\sigma)^2 - \frac{M^2}{4} + \Delta^2, \quad d_y^\sigma(k) = 2\Delta \varepsilon_{k,0}^\sigma. \quad (3.38)$$

We can confirm that gap closings for the 2BM also takes place at the nested points, since $d_y(k) = 0$ when

$$\varepsilon_{k_{\text{GC}},0}^\sigma = 0 \quad \Rightarrow \quad \xi_{k_{\text{GC}}}^{e+} + \sigma \xi_{k_{\text{GC}}}^{e-} = \xi_{k_{\text{GC}}}^{h+} - \sigma \xi_{k_{\text{GC}}}^{h-} \quad \Rightarrow \quad \xi_{k_{\text{GC}}-\sigma q}^e = \xi_{k_{\text{GC}}+\sigma q}^h, \quad (3.39)$$

with the last equality being the criteria for nesting between the two bands, *i.e.* $k_{\text{GC}} \equiv k_{\text{NP}}$. The equation above also indicates that each block has a separate set of nested points, k_{NP}^σ . The nested points in one σ -block is connected to the other through inversion, as discussed in the figure text of Fig.3.4.(c). This can be seen through the relation

$$\mathcal{I} \xi_{k_{\text{NP}}-\sigma q}^e = \mathcal{I} \xi_{k_{\text{NP}}+\sigma q}^h \quad \Rightarrow \quad \xi_{-k_{\text{NP}}+\sigma q}^e = \xi_{-k_{\text{NP}}-\sigma q}^h. \quad (3.40)$$

We thus find $k_{\text{NP}}^\sigma = -k_{\text{NP}}^{-\sigma}$. Solving $\mathbf{d}^\sigma(k_{\text{NP}}^\sigma) = \mathbf{0}$ leaves us with the criteria for gap closing

$$M = \pm 2 \sqrt{\Delta^2 + (\varepsilon_{k_{\text{NP}}^\sigma,1}^\sigma)^2} = \pm 2 \sqrt{\Delta^2 + (\xi_{k_{\text{NP}}^\sigma}^{e+} + \sigma \xi_{k_{\text{NP}}^\sigma}^{e-})^2} = \pm 2 \sqrt{\Delta^2 + \xi_{\text{NP}}^2}, \quad (3.41)$$

where $\xi_{\text{NP}} = \xi_{k_{\text{NP}}^\sigma-\sigma q}^e = \xi_{k_{\text{NP}}^\sigma+\sigma q}^h$ is the energy at the nested point. It is clear that the criteria is similar to the criteria obtained for the 1BM in an isotropic helix phase in Eq. 3.12. To calculate the winding number for each block, we can once again linearize about the nested points

$$\varepsilon_{k,0}^\sigma \approx \alpha_{\text{NP}}^\sigma k, \quad \varepsilon_{k,1}^\sigma \approx \xi_{\text{NP}} + \beta_{\text{NP}}^\sigma k \quad (3.42)$$

where $\alpha_{\text{NP}}^\sigma$ and β_{NP}^σ are functions of the set of nested points k_{NP}^σ . The expansion coefficients of the two blocks are connect in the way

$$\alpha_{\text{NP}}^\sigma = -\alpha_{\text{NP}}^{-\sigma}, \quad \beta_{\text{NP}}^\sigma = -\beta_{\text{NP}}^{-\sigma}, \quad (3.43)$$

as can be seen from the inversion symmetry of $\varepsilon_{k,0}^\sigma$ and $\varepsilon_{k,1}^\sigma$ upon differentiation. To make this statement more transparent, take the relation for $\alpha_{\text{NP}}^\sigma$

$$\begin{aligned}\alpha_{\text{NP}}^\sigma &= \partial_k \varepsilon_{k,0}^\sigma \Big|_{k=k_{\text{NP}}^\sigma} = \partial_k \left[\frac{\xi_k^{e+} - \xi_k^{h+}}{2} + \sigma \frac{\xi_k^{e-} + \xi_k^{h-}}{2} \right] \Big|_{k=k_{\text{NP}}^\sigma} \\ &= \left[\underbrace{\partial_k \frac{\xi_k^{e+} - \xi_k^{h+}}{2}}_{\text{Odd}} + \sigma \underbrace{\partial_k \frac{\xi_k^{e-} + \xi_k^{h-}}{2}}_{\text{Even}} \right] \Big|_{k=k_{\text{NP}}^\sigma} \\ &= -\alpha_{\text{NP}}^{-\sigma},\end{aligned}\tag{3.44}$$

where a similar logic can be applied for the other expansion coefficient β_{NP}^σ . The components of the parametrizing vector thus becomes

$$d_x^\sigma(k) = \xi_{\text{NP}}^2 + 2\xi_{\text{NP}}\beta_{\text{NP}}^\sigma k - \frac{M^2}{4} + \Delta^2, \quad d_y^\sigma(k) = 2\Delta\alpha_{\text{NP}}^\sigma k,\tag{3.45}$$

which results in the winding for each block of the Hamiltonian

$$w^\sigma = \sum_{k_{\text{NP}}^\sigma \in \text{BZ}} \text{Sign}[\alpha_{\text{NP}}^\sigma \Delta] \frac{\text{Sign}\left[\frac{M^2}{4} - \Delta^2 - \xi_{\text{NP}}^2\right]}{2}.\tag{3.46}$$

From the relation in Eq.3.43. the winding of the two blocks are related in the way

$$w^\sigma = -w^{-\sigma}.\tag{3.47}$$

Once again due to the non-compactified $\vec{d}^\sigma(k)$ vector, we need to combine the two windings in a right manner. A straight forward guess would be to subtract the two, *i.e.*

$$w = w^{\sigma=+1} - w^{\sigma=-1} = 2w^\sigma,\tag{3.48}$$

since the other possible combination would result in $w = w^{\sigma=+1} + w^{\sigma=-1} = 0$, see Eq.3.47. Since we do not have a benchmark to compare the total winding number with, as for the isotropic helix in the 1BM, we could include an infinitesimal symmetry breaking term and calculate the winding of the total Hamiltonian $\widehat{\mathcal{H}}(k)$. We will instead assume Eq. 3.48 to hold, and verify this through real space calculations later in this section.

Each block has two nested points k_{NP} , one with low energy, and one with high energy, as seen in Fig.3.4.(c). The energies at the nested points are respectively $\xi_{\text{NP}} = \{0, 1.88 t_e\}$, and the sign of the expansion coefficients are $\text{Sign}[\alpha_{\text{NP}}^\sigma] = \{+1, -1\}$ for each point respectively. This gives us the total winding number of the Hamiltonian

$$w = \text{Sign}[\Delta] \text{Sign}\left[\frac{M^2}{4} - \Delta^2\right] - \text{Sign}[\Delta] \text{Sign}\left[\frac{M^2}{4} - \Delta^2 - (1.88 t_e)^2\right].\tag{3.49}$$

This result tells us that we get two topological protected states at each end of the system, whenever $2\Delta < M < 2\sqrt{\Delta^2 + (1.88 t_e)^2}$. We observe that the inclusion of an additional band imposes an inversion symmetry connecting $\vec{d}^\sigma(k)$ of the two blocks, and thereby insures the occurrence of a pair of modes at each end, when opening the ring in Fig.3.4.(b). Thus every time a gap closes at k_{NP}^σ , the connecting inversion symmetry ensures a similar gap closing at $-k_{\text{NP}}^\sigma$. This confirms that we obtain a pair of topological protected states at each edge, which can be combined into two real MF solutions even though we are in the class AIII \oplus AIII.

Two-Band Model in the Anisotropic Helix Phase

Once again, extending the above analysis to a general anisotropic helix phase requires the inclusion of the momentum transfer spaces, as in Eq.3.17. The Hamiltonian thus becomes

$$\begin{aligned} \widehat{\mathcal{H}}(k) = \tau_z \left(\hat{h}_0^+(k) + \hat{h}_1^+(k)\eta_z + \hat{h}_2^-(k)\rho_z + \hat{h}_3^-(k)\eta_z\rho_z \right) \\ + \kappa_x \frac{M_x\rho_x\sigma_x + M_\perp\rho_y\sigma_y}{2} + \kappa_x\eta_x \frac{M_x\rho_x\sigma_x - M_\perp\rho_y\sigma_y}{2} + \Delta\tau_x \end{aligned} \quad (3.50)$$

with the spinor

$$\widehat{\Psi}_k^\dagger = \left(\Psi_k^\dagger, -i\Psi_{-k}^\dagger\rho_x\sigma_y \right), \quad \Psi_k^\dagger = \left(\psi_{ke}^\dagger, \psi_{kh}^\dagger \right), \quad \psi_{k\mu}^\dagger = \left(\hat{d}_{k+q\mu}^\dagger, \hat{d}_{k-q\mu}^\dagger, \hat{d}_{k-3q\mu}^\dagger, \hat{d}_{k+3q\mu}^\dagger \right) \quad (3.51)$$

The matrices $\hat{h}_i^s(k)$ are now linear combinations of $\hat{\xi}_k = \text{Diag} \{ \xi_k^e, \xi_k^h \}$ shifted with the appropriate momenta, similar to the ones defined in Eq.2.48. Firstly we note the Hamiltonian enjoys the symmetry $\rho_z\sigma_z$, as for the 1BM in an anisotropic helix phase. We block diagonalize with $\widehat{\mathcal{O}} = (\rho_z\sigma_z + \sigma_x)/\sqrt{2}$, to get the Hamiltonian of the two sectors as

$$\begin{aligned} \widehat{\mathcal{H}}^\sigma(k) = \tau_z \left(\hat{h}_0^+(k) + \hat{h}_1^+(k)\eta_z + \hat{h}_2^-(k)\rho_z + \hat{h}_3^-(k)\eta_z\rho_z \right) \\ + \kappa_x\rho_x \frac{M_x\sigma - M_\perp}{2} + \kappa_x\eta_x\rho_x \frac{M_x\sigma + M_\perp}{2} + \Delta\tau_x. \end{aligned} \quad (3.52)$$

Additionally we find the symmetry $\kappa_z\rho_z$, which results to additional block diagonalization with $\widehat{\mathcal{O}} = (\kappa_z\rho_z + \rho_x)/\sqrt{2}$, resulting in the Hamiltonian for each block

$$\begin{aligned} \widehat{\mathcal{H}}^{\rho\sigma}(k) = \tau_z \left(\hat{h}_0^+(k) + \hat{h}_1^+(k)\eta_z + \rho\kappa_z\hat{h}_2^-(k) + \rho\kappa_z\hat{h}_3^-(k)\eta_z \right) \\ + \rho\kappa_x \frac{M_x\sigma - M_\perp}{2} + \rho\kappa_x\eta_x \frac{M_x\sigma + M_\perp}{2} + \Delta\tau_x. \end{aligned} \quad (3.53)$$

With the chiral symmetry present $\Pi = \tau_y\kappa_z$, we find the matrix $\hat{A}^{\rho\sigma}(k)$ by off diagonalizing the Hamiltonian with the unitary operator $\widehat{U} = (\tau_z\kappa_z + \tau_y)/\sqrt{2}$;

$$\begin{aligned} \hat{A}^{\rho\sigma}(k) = -i \left(\hat{h}_0^+(k)\kappa_z + \hat{h}_1^+(k)\kappa_z\eta_z + \rho\hat{h}_2^-(k) + \rho\hat{h}_3^-(k)\eta_z \right) \\ + \rho\kappa_y \frac{M_x\sigma - M_\perp}{2} + \rho\kappa_y\eta_x \frac{M_x\sigma + M_\perp}{2} - \Delta. \end{aligned} \quad (3.54)$$

The symmetry giving rise to the σ block structure was the same as for the 1BM, which indicates that the winding for each of these should be subtracted to constitute a topological invariant. We also know from the 2BM in a isotropic helix phase that, the inclusion of an additional band gave rise to two blocks connected by inversion, which for the given case, seems to be the two ρ -sectors. This would immediately give us the following combination of the windings

$$w = (w^{\rho=+1\sigma=+1} - w^{\rho=+1\sigma=-1}) - (w^{\rho=-1\sigma=+1} - w^{\rho=-1\sigma=-1}). \quad (3.55)$$

To check the equation above, let us write the block Hamiltonians $\hat{h}^{\rho\sigma}(k)$ explicitly on matrix form, when excluding Nambu space;

$$\hat{h}^{\rho=1\sigma}(k) = \begin{pmatrix} \xi_{k+q}^e & 0 & \frac{M_x\sigma - M_\perp}{2} & \frac{M_x\sigma + M_\perp}{2} \\ 0 & \xi_{k-3q}^e & \frac{M_x\sigma + M_\perp}{2} & \frac{M_x\sigma - M_\perp}{2} \\ \frac{M_x\sigma - M_\perp}{2} & \frac{M_x\sigma + M_\perp}{2} & \xi_{k-q}^h & 0 \\ \frac{M_x\sigma + M_\perp}{2} & \frac{M_x\sigma - M_\perp}{2} & 0 & \xi_{k+3q}^h \end{pmatrix}, \quad (3.56a)$$

and

$$\hat{h}^{\rho=-1\sigma}(k) = \begin{pmatrix} \xi_{k-q}^e & 0 & -\frac{M_x\sigma-M_\perp}{2} & -\frac{M_x\sigma+M_\perp}{2} \\ 0 & \xi_{k+3q}^e & -\frac{M_x\sigma+M_\perp}{2} & -\frac{M_x\sigma-M_\perp}{2} \\ -\frac{M_x\sigma-M_\perp}{2} & -\frac{M_x\sigma+M_\perp}{2} & \xi_{k+q}^h & 0 \\ -\frac{M_x\sigma+M_\perp}{2} & -\frac{M_x\sigma-M_\perp}{2} & 0 & \xi_{k-3q}^h \end{pmatrix}. \quad (3.56b)$$

We observe from the matrices, that ρ indeed describes the two blocks connected by inversion

$$\mathcal{I} \xi_{k_{\text{NP}}-\rho q}^e = \mathcal{I} \xi_{k_{\text{NP}}+\rho q}^h, \quad \Rightarrow \quad \xi_{-k_{\text{NP}}+\rho q}^e = \xi_{-k_{\text{NP}}-\rho q}^h, \quad (3.57)$$

in equivalence to the two σ -sector for the 2BM in the isotropic helix phase. This tells us that $w^{\rho\sigma} = -w^{-\rho\sigma}$. We also observe that in the isotropic helix limit, $M_x = M_\perp = M/2$, only certain bands are nested in each σ -sector. For $\sigma = +1$ we get the matrix

$$\hat{h}^{\rho\sigma=+1}(k) = \begin{pmatrix} \xi_{k+\rho q}^e & 0 & 0 & \rho\frac{M}{2} \\ 0 & \xi_{k-\rho 3q}^e & \rho\frac{M}{2} & 0 \\ 0 & \rho\frac{M}{2} & \xi_{k-\rho q}^h & 0 \\ \rho\frac{M}{2} & 0 & 0 & \xi_{k+\rho 3q}^h \end{pmatrix}. \quad (3.58)$$

We have the following nestings: $\xi_{k+\rho q}^e = \xi_{k+\rho 3q}^h$ and $\xi_{k-\rho 3q}^e = \xi_{k-\rho q}^h$, which do not have a solution in the RBZ, *i.e.* $k_{\text{NP}} \notin \text{RBZ}$, and we can thus simply concentrate on the single $\sigma = -1$ block, and the winding number can thus be found through

$$w = 2w^{\rho\sigma=-1}. \quad (3.59)$$

It is now straightforward to linearize the dispersions about the nested points in the $\sigma = -1$ block, and calculate the winding. This procedure is as in the preceding sections, but the result is long and unintuitive, so we have instead plotted the winding in parameter space for different values of Λ , see Fig.3.5.(a). In Fig.3.5.(b) we show how the band structure develops as we make a sweep in parameter space from I-VI ($\Lambda = \pi/8$). Here we see that the inversion symmetry that connects the two blocks of the Hamiltonian, indeed ensures gap closings at $\pm k_{\text{NP}}^\rho$, giving rise to two topologically protected states at each end, as seen from Fig.3.5.(c), where we have plotted the absolute square of the obtained wave functions in real space. A state $\gamma_{i\mu}$ and $\tilde{\gamma}_{i\mu}$ are degenerate, and will always come in pairs. We see that the guess in Eq.3.48 indeed was a good guess, since the edge states did arise. Furthermore we see that the inclusion of an extra band modifies the phase diagram, but most drastically makes the topologically protected edge states to come in pairs.

Low Energy Projection of the Two-Band Model

We can also for this model carry out a projection onto the low energy states, to get an effective model describing gap closings at the Fermi level. Again using Eq. 3.27, on the free part of the Hamiltonian in Eq.3.53, we find that the low energy model is obtained by projection the Hamiltonian onto the states $|\kappa_z = \pm 1, \eta_z = -1\rangle$.

$$\mathcal{H}^{\rho\sigma}(k) = \tau_z \left(\frac{\xi_{k-\rho 3q}^e + \xi_{k+3\rho q}^h}{2} + \frac{\xi_{k-\rho 3q}^e - \xi_{k+3\rho q}^h}{2} \nu_z \right) + \rho \nu_x \frac{M_x\sigma - M_\perp}{2} + \Delta \tau_x \quad (3.60)$$

where ν is acting on the nested bands. This low energy model carries the resemblance of the low energy model of the 1BM but with an additional band index. We find the winding number for each σ block to be

$$w^\sigma = \text{Sign}[\Delta] \text{Sign} \left[\left(\frac{M_x \sigma - M_\perp}{2} \right)^2 - \Delta^2 \right] \quad (3.61)$$

where we have used the fact that $w^{\rho\sigma} = -w^{-\rho\sigma}$. Note that the Hamiltonian in this low energy basis has nested points in both σ -sectors, resulting in the topological invariant $w = w^{\sigma=+1} - w^{\sigma=-1}$. This approximation scheme is valid as long as the magnetic gap is less than the energy at the upper nested point, *i.e.* $M/(1.88 t_e) \ll 1$.

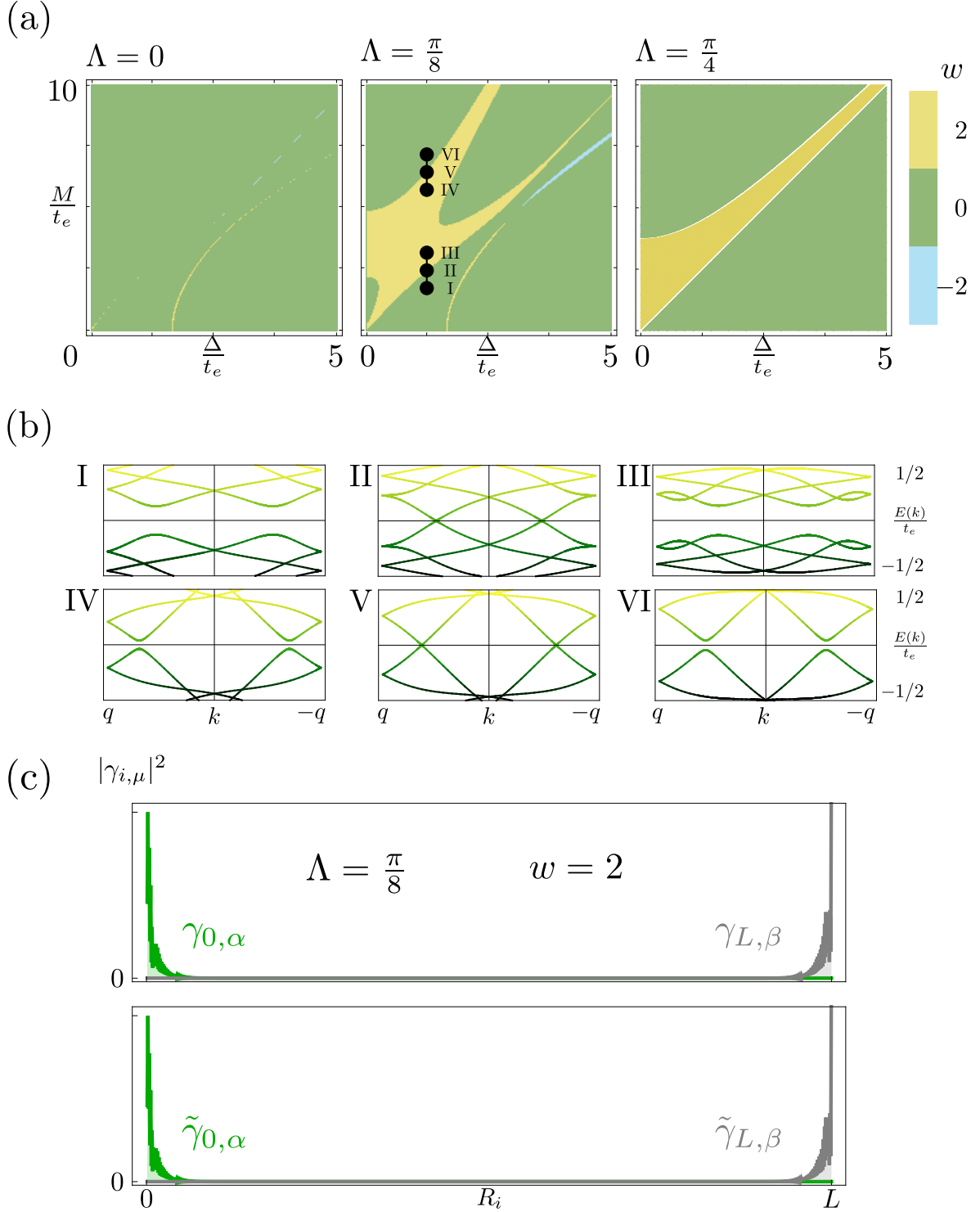


Figure 3.5: (a) Shows the topological phase diagram for different magnetic helices distinguished by Λ . The narrow blue region seems to be an numerical error, and could not be detected in real space simulations. (b) Depicts the gap structure and how it changes for a sweep in parameter space from I-VI. (c) Shows a real space calculation of the topological states' wave functions in the topological non-trivial phase. The length of the chain is $L = 1000 a$, where a is the lattice constant. One obtains two MFs per edge due to the band doubling.

Chapter 4

Topological Phases of 2D Magnetic Superconductors

After having carried out the studies of the possible topological phases of the 1BM and 2BM in 1D, we will now extend our analysis to 2D, in order to obtain a deeper insight in the topological phases of the FeSCs. The approach will be the same as in the previous chapter, *i.e.* we will start from the 1BM and proceed with the 2BM.

In the process of determining the phases of the 2D models, we found out that the low energy Hamiltonian can be described by expanding about single- \mathbf{Q} and double- \mathbf{Q} nested points. The former is similar to the single- \mathbf{Q} magnetic helices discussed up to this point, with gap closings at the set of nested point \mathbf{k}_{NP} . The physics of the double- \mathbf{Q} nested points are arising with the increase in dimensionality, and allow for gap closings to take place at the set of double- \mathbf{Q} nested point \mathbf{k}_{DN} . The single- \mathbf{Q} nested points can effectively be described as quasi-1D systems, which give rise to Majorana flat bands (MFB) (see Sec. 1.5), whereas the double- \mathbf{Q} nested points produce either chiral or helical modes, depending on the symmetry class (see Sec.1.5). To clarify the above, we will start from a 2D system in the magnetic helix phase, reminiscing the behavior of the single- \mathbf{Q} nested points for a 2D model in a Double- \mathbf{Q} C_4 -symmetric Spin-Whirl Crystal (\bullet) phase. Thus we get an effective quasi-1D model, as discussed below.

4.1 Quasi-1D Single-Band Model

As stated above we will here pursue a better understanding the single- \mathbf{Q} nested points in the full 2D model. To do this, we consider the extension of the 1BM to 2D in a helix magnetic phase. The real space Hamiltonian is therefore simply

$$H = \sum_{ij} \hat{d}_i^\dagger \left[-\frac{t}{2} \sum_{\mathbf{u}} \delta_{\mathbf{R}_j, \mathbf{R}_i + \mathbf{u}} + \left(\mu + M_x \cos(\mathbf{Q} \cdot \mathbf{R}_i) \sigma_x + M_\perp \sin(\mathbf{Q} \cdot \mathbf{R}_i) \sigma_y \right) \delta_{\mathbf{R}_i, \mathbf{R}_j} \right] \hat{d}_j, \quad (4.1)$$

where \mathbf{u} connects next nearest neighbor sites, as shown in Fig.4.1.(a). The magnetic texture is only modulated in one direction \mathbf{Q} , and the system can therefore be considered as a stack of 1D BDI chains. If the ordering wave-vector is along, say, the k_x -direction $\mathbf{Q} = (Q, 0)$,

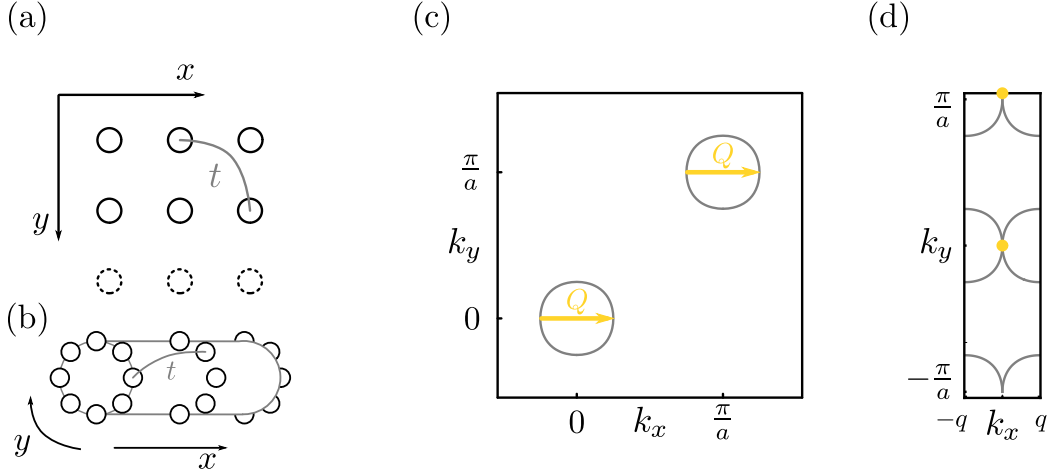


Figure 4.1: (a) Real space representation of the hopping matrix elements for the 2D 1BM. (b) Imposing periodic boundary conditions along the direction perpendicular to the ordering wave-vector, in this case along the y -direction, the system is equivalent to a cylinder. (c) Fermi surface for the 1BM in 2D with nesting along $\mathbf{Q} = (Q, 0)$, as indicated by the yellow arrows. As we know from the 1D case, nesting can also take place at finite energy away from the FS (not shown). (d) The folded FS in the RBZ, where the yellow dots represent the nested points at the FS. Note again that we must have points at finite energy, since nesting also takes place away from the FS.

as shown on the FS in Fig.4.1.(c), we can impose periodic boundary conditions along the y -direction, as in Fig.4.1.(b), and have k_y as a parameter of the system. By explicitly performing the transformation in y , we get the Hamiltonian for each k_y

$$H(k_y) = \sum_{i,j} \hat{d}_{i k_y}^\dagger [-t \delta_{j, i \pm a} \cos(k_y) + \mu \delta_{i,j} + M_x \cos(Q R_i) \delta_{i,j} \sigma_x + M_\perp \sin(Q R_i) \delta_{i,j} \sigma_y] \hat{d}_{j k_y}, \quad (4.2)$$

where the summation over i and j are lattice sites for each 1D BDI chain. We see that the Fourier transformation simply renormalizes the hopping matrix element $t \rightarrow t \cos(k_y)$. The Hamiltonian for $k_y = 0$ connects to the 1BM in 1D, as desired. By a transformation to Bloch space in both direction, followed by a folding of the FS along \mathbf{Q} , we arrive at the FS in the RBZ in Fig.4.1.(d), with the yellow dots indicating the nested points \mathbf{k}_{NP} at the FS. We know from the 1D 1BM that nesting also takes place at finite energy away from the FS (not shown).

Quasi-1D Single-Band Model in the Isotropic Helix Phase

Since k_y constitutes a parameter of the quasi-1D model, we can perform the exact same calculations as for the 1D 1BM in a isotropic helix phase, but with the renormalized hopping

matrix element. The straightforward calculation yields the k_y -dependent winding

$$w^{k_y} = \sum_{k_{\text{NP}} \in \text{BZ}} \text{Sign} [\Delta v_{\text{NP}} \cos(k_y)] \frac{\text{Sign} \left[\frac{M^2}{4} - \Delta^2 - \overbrace{[\sqrt{2}t - \sqrt{2}t \cos(k_y) \cos(k_{\text{NP}})]^2}^{\xi_{\text{NP}}(k_y)} \right]}{2},$$

where the energy at the nested points now is a function of k_y , as indicated by $\xi_{\text{NP}}(k_y)$. It is straightforward to find the nested points for each k_y value by solving, see Eq.3.10;

$$\xi_{k_{\text{NP}}}^-(k_y) = 0 \quad \Rightarrow \quad \sin(k_{\text{NP}}) \sin(q) \cos(k_y) = 0 \quad \Rightarrow \quad k_{\text{NP}} = \{0, \pi/a\}. \quad (4.3)$$

Note that we have omitted the solution $k_y = \pi/(2a)$ as will be discussed later. Clearly we have nesting for every k_y -value, however, these do not take place at the FS, but at finite energy away from the FS, as can be seen from the relation for the energy at the nested point $\xi_{\text{NP}}(k_y)$. The latter indicates that we have a whole continuum of nested points above the FS. By inserting the values for the nested points k_{NP} we retrieve the winding number

$$\begin{aligned} w^{k_y} &= \text{Sign} [\Delta \cos(k_y)] \frac{\text{Sign} \left[\frac{M^2}{4} - \Delta^2 - 2t^2[1 - \cos(k_y)]^2 \right] - \text{Sign} \left[\frac{M^2}{4} - \Delta^2 - 2t^2[1 + \cos(k_y)]^2 \right]}{2} \\ &= \text{Sign} [\Delta] \frac{\text{Sign} \left[\frac{M^2}{4} - \Delta^2 - 2t^2[1 - \cos(k_y)]^2 \right] - \text{Sign} \left[\frac{M^2}{4} - \Delta^2 - 2t^2[1 + \cos(k_y)]^2 \right]}{2} \end{aligned} \quad (4.4)$$

with $k_y \in (-\frac{\pi}{a}, \frac{\pi}{a}] \setminus \{-\frac{\pi}{2a}, \frac{\pi}{2a}\}$, since $k_y = \pm\pi/(2a)$ removes all hopping elements and breaks the symmetry, *i.e.* no winding number can be defined. We thus have one MF at each end whenever

$$2\sqrt{\Delta^2 + 2t^2[1 - \cos(k_y)]^2} < M < 2\sqrt{\Delta^2 + 2t^2[1 + \cos(k_y)]^2} \quad (4.5)$$

which clearly coincides with the result for the strictly 1D case with $k_y = 0$. Observe that the maximum span for a topological nontrivial window is for $k_y = 0$, thus the strictly 1D model sets the threshold for the topological non-trivial phase, but also the threshold for the reentrance of the trivial phase. In the region in parameter space spanned by the thresholds for $k_y = 0$, MFs occurs and disappears at different k_y values, which generates MFB.

Quasi-1D Single-Band Model in the Anisotropic Helix Phase

By performing the transformation in both direction, *i.e.* also in x , and employing the momentum transfer Pauli matrices ρ and η , as shown in Fig. 4.1.(d), we arrive at the defining matrix for each σ -block

$$\begin{aligned} \hat{A}^\sigma(\mathbf{k}) &= -i(h_0^+(\mathbf{k})\rho_z + h_1^+(\mathbf{k})\eta_z\rho_z + h_2^-(\mathbf{k}) + h_3^-(\mathbf{k})\eta_z) \\ &\quad -\rho_y \frac{M_x\sigma - M_\perp}{2} - \eta_x\rho_y \frac{M_x\sigma + M_\perp}{2} - \Delta. \end{aligned} \quad (4.6)$$

We remember that the matrix was block diagonalized to $\hat{\mathcal{H}}^{\sigma=+1}(\mathbf{k}) \oplus \hat{\mathcal{H}}^{\sigma=-1}(\mathbf{k})$, due to the symmetry $\rho_z\sigma_z$. Once again we linearize the functions $h_i^s(\mathbf{k})$, which now has renormalized

hopping matrix elements, about the nested point $k_{\text{NP}} = 0$, see the yellow dots in Fig.4.1.(d)., and keep k_y as a free parameter:

$$h_0^+(\mathbf{k}) \approx \sqrt{2}t, \quad h_1^+(\mathbf{k}) \approx -\sqrt{2}t \cos(k_y) \quad (4.7a)$$

$$h_2^-(\mathbf{k}) \approx 0, \quad h_3^-(\mathbf{k}) \approx -\sqrt{2}t \cos(k_y) k_x, \quad (4.7b)$$

which results in the parametrizing vector components

$$d_x^\sigma(k_x) = 4t^2 \cos^2(k_y) (\Delta^2 + M_\perp M_x \sigma + t^2 \cos^2(k_y) - 2t^2) + (M_\perp^2 - 2t^2 - \Delta^2) (M_x^2 - 2t^2 - \Delta^2) \quad (4.8a)$$

$$d_y^\sigma(k_x) = 16\sqrt{2}t^3 \Delta \cos^2(k_y) k_x. \quad (4.8b)$$

This results in the winding number for each block:

$$w^{\sigma k_y} = \text{Sign}[t\Delta] \text{Sign}[4t^2 \cos^2(k_y) (\Delta^2 + M_\perp M_x \sigma + t^2 \cos^2(k_y) - 2t^2) + (M_\perp^2 - 2t^2 - \Delta^2) (M_x^2 - 2t^2 - \Delta^2)] / 2. \quad (4.9)$$

As expected from the strictly 1D 1BM, are the vectors $\mathbf{d}^\sigma(k_x)$ not compactified, and only combined can they constitute a topological invariant;

$$\begin{aligned} w^{k_y} &= w^{k_y \sigma=+1} - w^{k_y \sigma=-1} \\ &= \frac{\text{Sign}[t\Delta]}{2} (\text{Sign}[4t^2 \cos^2(k_y) (\Delta^2 + M_\perp M_x + t^2 \cos^2(k_y) - 2t^2) + (M_\perp^2 - 2t^2 - \Delta^2) (M_x^2 - 2t^2 - \Delta^2)] \\ &\quad - \text{Sign}[4t^2 \cos^2(k_y) (\Delta^2 - M_\perp M_x + t^2 \cos^2(k_y) - 2t^2) + (M_\perp^2 - 2t^2 - \Delta^2) (M_x^2 - 2t^2 - \Delta^2)]). \end{aligned} \quad (4.10)$$

To illustrate accessible values of the above topological invariant we have shown in Fig.4.2. the topological phase diagram for different values of k_y , in the anisotropic helix phase with $\Lambda = \pi/8$ (see Eq.3.26. for the relation of the magnitudes of the moments and Λ). Certain regions in parameter space harbor MFs for a whole range of k_y , unlike the usual case with a single k -value. This range of k_y -values indicates that we get MFs with flat dispersion, *i.e.* MFBs, and we would expect the width of this flat band to be dependent on where in parameter space the system resides. To verify this, we opened the system along the x -direction, and plotted the energy dispersions as a function of the parameterizing k_y in Fig.4.3. We clearly see that when entering the topological non-trivial phase flat bands at zero energy occurs. Additionally we see that the width of the flat bands increases to a certain point, and decreases upon approaching the trivial zone.

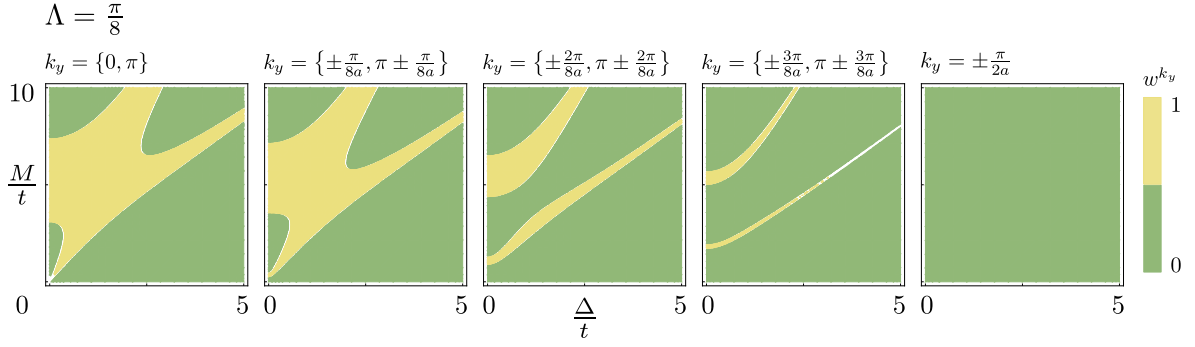


Figure 4.2: Display of topological phase diagrams for $k_y \in [-\frac{\pi}{a}, \frac{\pi}{a})$ in steps of $\frac{\pi}{8a}$. We have here shown them for the magnetic anisotropic case with $\Lambda = \frac{\pi}{8}$. The figure clearly shows that no topological phase can be obtained for $k_y = \pm \frac{\pi}{2a}$.

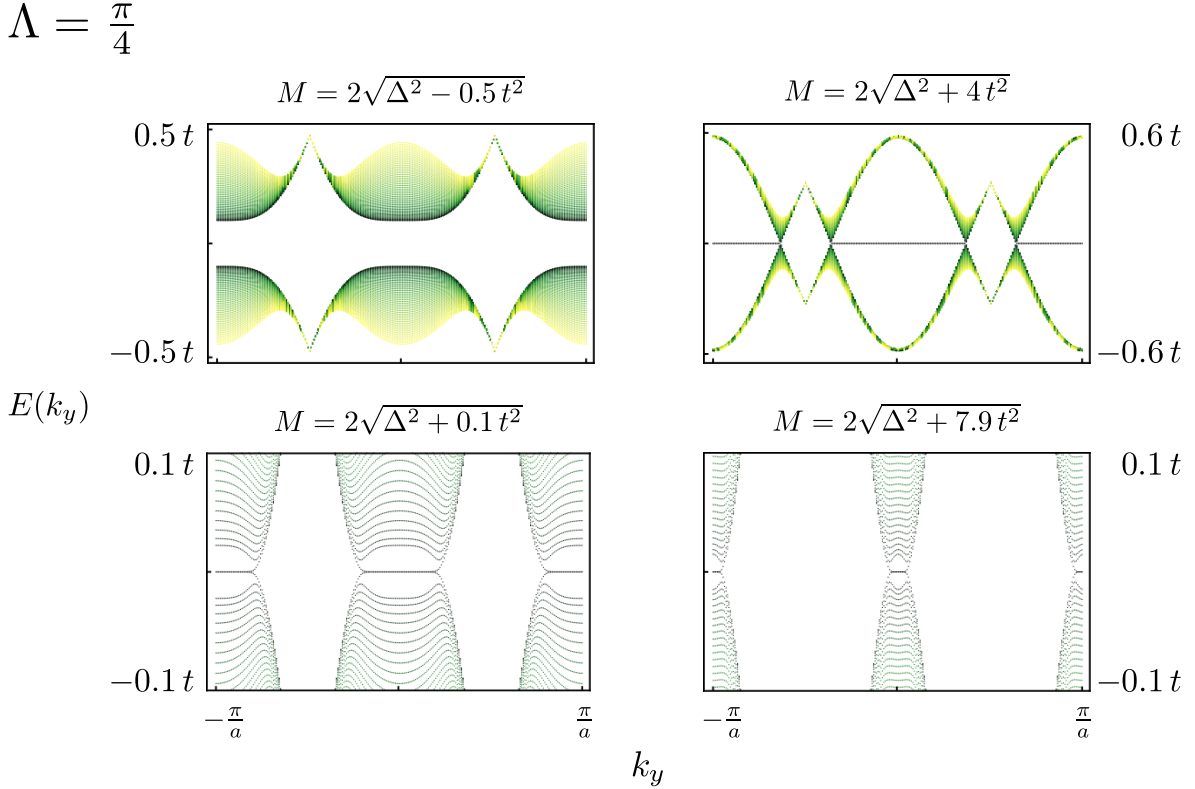


Figure 4.3: We show the flat energy dispersions for the MFBs at different points in parameter space, with $\Lambda = \frac{\pi}{4}$. Note that the topological non-trivial regime is spanned by the topological regime in the strictly 1D case, *i.e.* $2\Delta < M < 2\sqrt{\Delta^2 + 8t^2}$. Clearly the width of the flat bands increase to a certain point in parameter space, and starts shrinking again when approaching the trivial regime. We have shown the 100 lowest eigenvalues for each value of k_y , for a system of $L_x = 500a$, $\Delta = 2.5t$, and a step size of $\frac{\pi}{128a}$ in k_y .

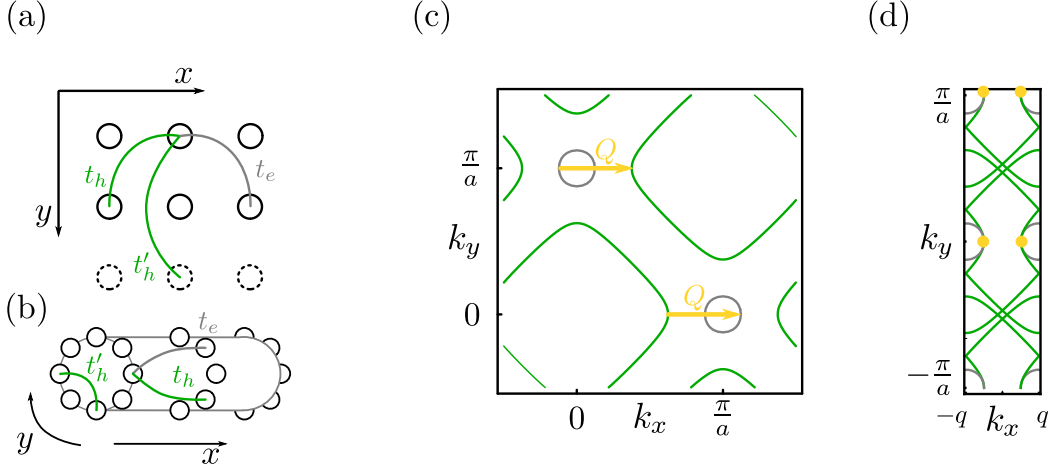


Figure 4.4: (a) Real space representation of the hopping matrix elements, with the colors depicting the two flavors of electrons generating the two bands. (b) By imposing periodic boundary condition along the y -direction, the system can be viewed as a cylinder, allowing for a transformation to Bloch space along this direction. (c) Fermi surface of the 2BM in 2D with nesting along $\mathbf{Q} = (Q, 0)$, as indicated by the yellow arrows. We have here only shown one set of nesting vectors, but nesting also takes place with the inversion transformed counterparts of the ones shown. (d) Fermi surface after a folding along \mathbf{Q} , here the yellow dots represent all nested points at the FS.

4.2 Quasi-1D Two-Band Model

Next, to explore the single- \mathbf{Q} nested behavior for the 2BM model in 2D, we find the real-space quasi-1D Hamiltonian

$$H = \sum_{ij} \hat{d}_i^\dagger \left[\frac{\hat{t}}{4} \sum_{\mathbf{u}} \delta_{\mathbf{R}_j, \mathbf{R}_i + \mathbf{u}} + \frac{\hat{t}'}{2} \sum_{\mathbf{u}'} \delta_{\mathbf{R}_j, \mathbf{R}_i + \mathbf{u}'} - \hat{\epsilon} \delta_{\mathbf{R}_i, \mathbf{R}_j} + \kappa_x M_x \delta_{\mathbf{R}_i, \mathbf{R}_j} \cos(\mathbf{Q} \cdot \mathbf{R}_i) \sigma_x + \kappa_x M_\perp \delta_{\mathbf{R}_i, \mathbf{R}_j} \sin(\mathbf{Q} \cdot \mathbf{R}_i) \sigma_y \right] \hat{d}_j, \quad (4.11)$$

with the matrices defined in Eq.3.31. The vectors \mathbf{u} and \mathbf{u}' connect next nearest, and next next nearest neighbor sites, respectively, as illustrated in Fig.4.4.(a). Let us, once again, focus on nesting taking place along the x -direction, allowing for a Fourier transformation along y , as in Fig.4.4.(b). The resulting Hamiltonian becomes

$$H(k_y) = \sum_{ij} \hat{d}_{ik_y}^\dagger \left[\frac{\hat{t}}{2} \delta_{j, i \pm a} \cos(k_y) + \hat{t}' \left(\frac{\delta_{i, j \pm 2a}}{2} + \cos(2k_y) \delta_{i, j} \right) - \hat{\epsilon} \delta_{i, j} + \kappa_x M_x \cos(Rx_i) \delta_{i, j} \sigma_x + \kappa_x M_\perp \sin(QR_i) \delta_{i, j} \sigma_y \right] \hat{d}_{jk_y} \quad (4.12)$$

again with the summation running over the lattice sites for each 1D chain. The Hamiltonian coincides with Eq.3.30 when $k_y = 0$. Similar to the quasi-1D 1BM we see that this transformation simply renormalizes the hopping parameter $\hat{t} \rightarrow \hat{t} \cos(k_y)$, but also the on-site energy $\hat{\epsilon} \rightarrow \hat{\epsilon} - \hat{t}' \cos(2k_y)$. A full transformation to Bloch space in both directions, followed by a folding of the FS along the nesting direction \mathbf{Q} , results in the FS shown in Fig.4.4.(d).

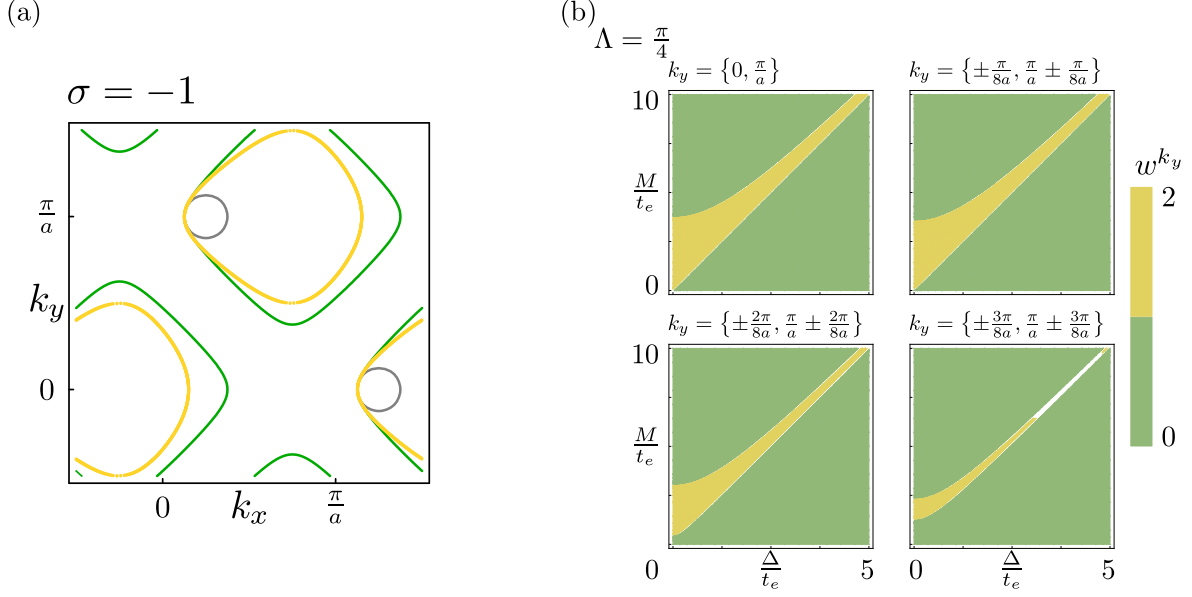


Figure 4.5: (a) Set of nested points for each parameterizing k_y -values projected onto the FS generated in the $\sigma = -1$ sector. It is sufficient to only study one sectors, since the two are connected by inversion. (b) The topological phase diagrams for different values of k_y . Certain regions supports MFs for a range of k_y -values, and would generate MFBs. Note also that the winding in the topological non-trivial regions is $w^{k_y} = 2$, meaning that the inversion symmetry connecting the two σ -blocks once again ensures a pair of MFs to occur at each edge.

Quasi-1D Two-Band Model in the Isotropic/Anisotropic Helix Phase

Since k_y now enters as a parameter, and the fact that the Fourier transformation simply renormalizes the hopping parameters and on-site energies, we can perform the exact same calculations as for the 2BM in 1D, and get the k_y dependent winding number when the system is in the isotropic spiral phase

$$w^{k_y \sigma} = \sum_{k_{\text{NP}}^\sigma \in \text{BZ}} \text{Sign} [\alpha_{\text{NP}}^\sigma \Delta \cos(k_y)] \frac{\text{Sign} \left[\frac{M^2}{4} - \Delta^2 - \frac{\xi_{\text{NP}}(k_y)}{2} \right]^2}{2}. \quad (4.13)$$

We remind ourself that the Hamiltonian in 1D has the symmetry $\kappa_z \sigma_z$, leaving it on the form $\hat{\mathcal{H}}^{\sigma=+1}(\mathbf{k}) \oplus \hat{\mathcal{H}}^{\sigma=-1}(\mathbf{k})$. The two blocks are connected by inversion, and have to be combined in the following way to give rise to a topological invariant

$$w^{k_y} = w^{k_y \sigma=+1} - w^{k_y \sigma=-1} = 2w^{k_y \sigma}. \quad (4.14)$$

As it is known from Sec.3.2. gap closings take place at the nested points k_{NP} , which can be found via the relation

$$\xi_{k_{\text{NP}}^\sigma - \sigma q}^\epsilon(k_y) = \xi_{k_{\text{NP}}^\sigma + \sigma q}^h(k_y), \quad (4.15)$$

where we remember that the dispersions have been renormalized, and now are dependent on k_y . The locations of the nested points for this more complicated band structure become a function of k_y , *i.e.* $k_{\text{NP}}^\sigma(k_y)$, and is not as simple as the quasi-1D 1BM. To illustrate this, we have numerically found the set of nested points for each k_y -value, in the $\sigma = -1$ block, and project them onto the FS generated by $\xi_{\mathbf{k}+q}^e$ and $\xi_{\mathbf{k}-q}^h$, see the yellow points in Fig.4.5.(a). With the nested points known for a given σ -block, one can retrieve the k_y -dependent winding given in Eq.4.13. We show in Fig.4.5 the topological phase diagrams for different values of the parametrizing k_y . Again we see that some regions have several k_y -values supporting MFs resulting in MFBs, similar to the 1BM. Note once again that the threshold for the topological nontrivial phase is determined by the strictly 1D case, *i.e.* $2\Delta < M < 2\sqrt{\Delta^2 + (1.88t_e)^2}$. The inversion symmetry that connects the two σ -blocks ensures the occurrence of two MFBs at each edge, as for the 1D 2BM. We have, as for the 1BM, shown the flat dispersions for the MFBs, see Fig.4.6. We see that the width of the bands increases to a certain point, and decreases when approaching the trivial regime (compare to Fig.4.5.(b)). Each flat band is four times degenerate, in agreement with the winding number w^{k_y} , with two MFs located at each end when the system is opened in the x -direction.

For the system in the anisotropic helix phase the procedure is the same, *i.e.* insert the renormalized hopping matrix elements and on-site energies, and calculate the winding numbers. Remember that the Hamiltonian in the anisotropic helix in 1D gets on the block form $\widehat{\mathcal{H}}^{\rho\sigma}(k)$, where ρ now is the two sectors connected by inversion, and that only the $\sigma = -1$ block constitutes nested points. We thus obtain the total winding number

$$w^{k_y} = 2w^{k_y \rho \sigma = -1}. \quad (4.16)$$

Again is the final result long an unintuitive, and therefore not include. It is, however, a simple manner to calculate when all the nested points are know, as shown in Fig.4.5.

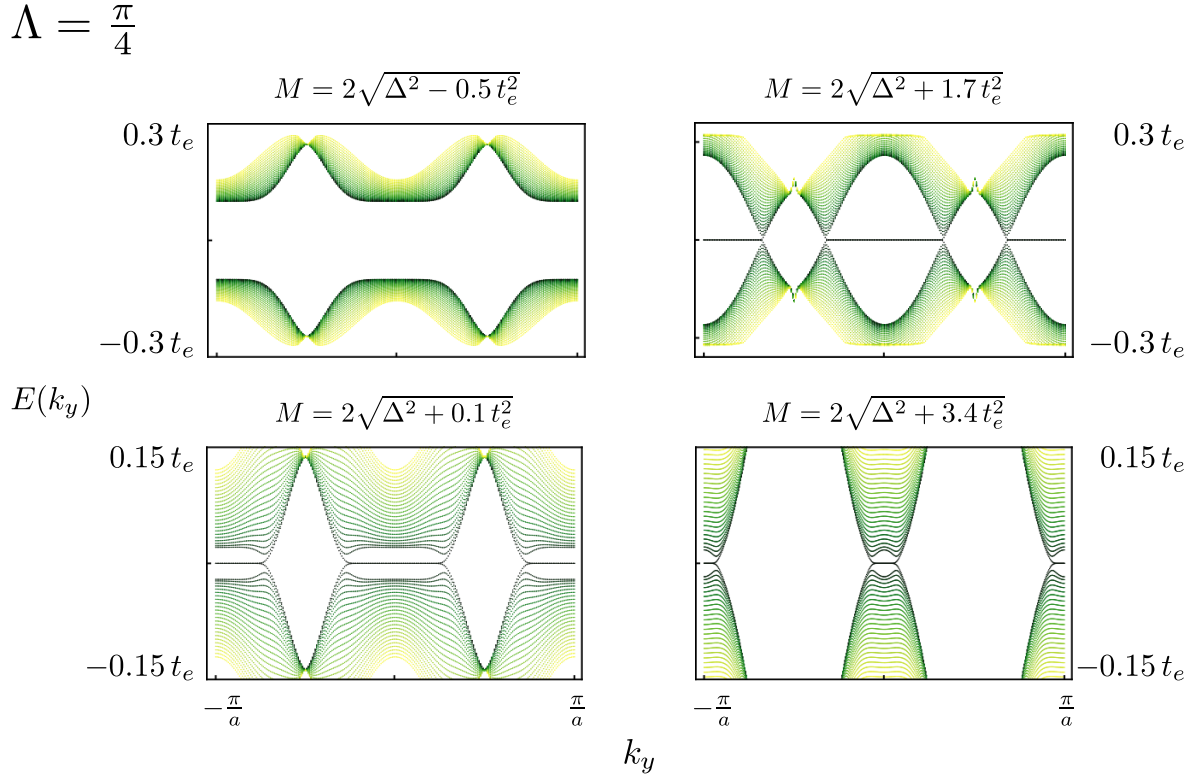


Figure 4.6: MFBs in different regions in parameter space, with increasing/decreasing width of the flat energy bands. Similar to the 1BM we have $L = 500a$, $\Delta = 2.5t_e$ and a step size of $\pi/(128a)$ in k_y . Again we can confirm that the threshold for the topological non-trivial phase is given for the strictly 1D 2BM, *i.e.* for $k_y = 0$. Lastly is each flat band four times degenerate, meaning that we get two MFs at each edge, due to the inversion symmetry connecting the two blocks of the Hamiltonian.

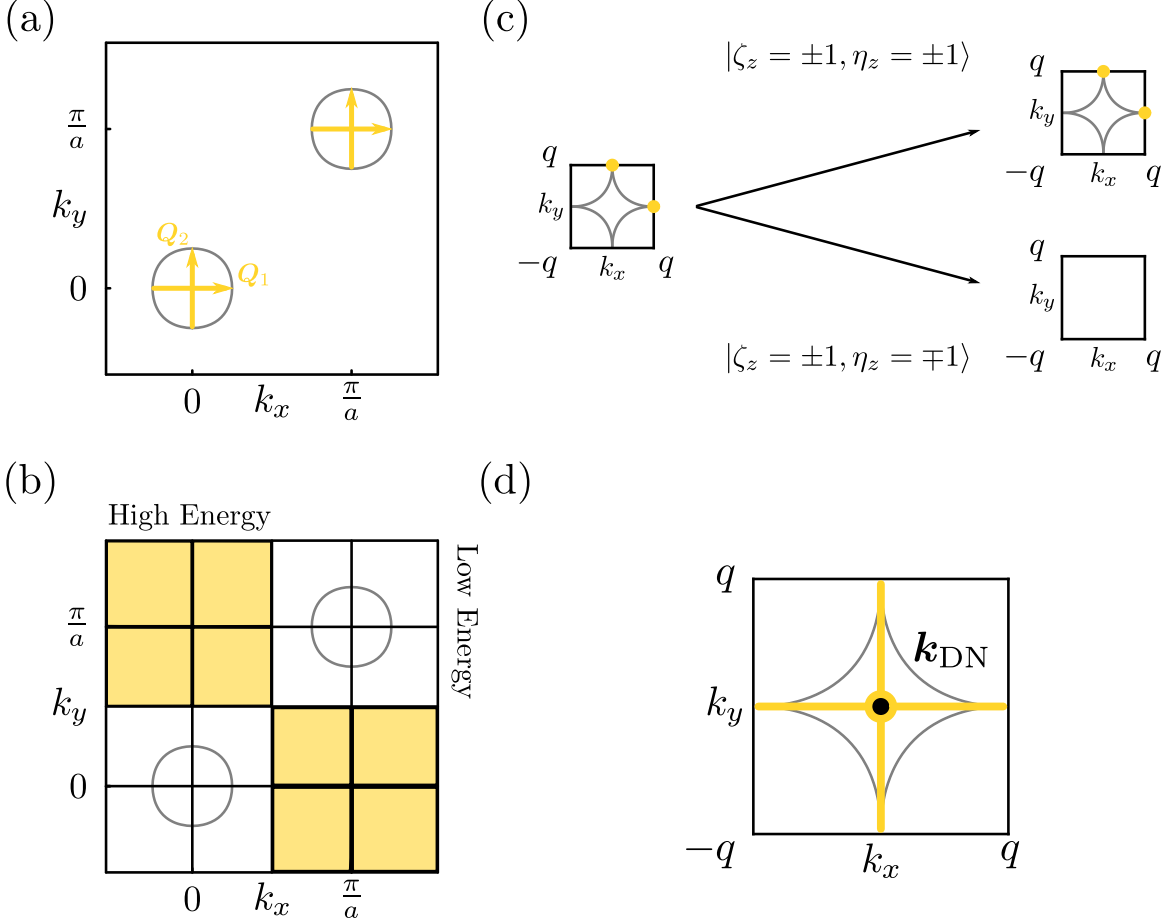


Figure 4.7: (a) The FS of the 1BM with nesting along both \mathbf{Q}_1 and \mathbf{Q}_2 . (b) We can project the Hamiltonian onto the nested bands at the FS in order to get an effective low energy Hamiltonian. The parts of the band structure that are not nested at the FS are colored yellow. (c) After a folding of the FS, we can project it onto either the high (bottom), or low energy (top) sector. Clearly only the low energy sector has nesting at the FS. (d) The yellow lines show all the nested points \mathbf{k}_{NP} , where we have a double- \mathbf{Q} nested point at the center of the FS, \mathbf{k}_{DN} , indicated by the black dot.

4.3 2D Single-Band Model

When we now focus on the Double- \mathbf{Q} C_4 -symmetric Spin-Whirl Crystal (\bullet) magnetic phase, the real space Hamiltonian takes the form

$$\begin{aligned}
 H = \sum_{ij} \hat{d}_i^\dagger \left[-\frac{t}{2} \sum_{\mathbf{u}} \delta_{\mathbf{R}_j, \mathbf{R}_i + \mathbf{u}} + \mu \delta_{\mathbf{R}_i, \mathbf{R}_j} + M_x \delta_{\mathbf{R}_i, \mathbf{R}_j} [\cos(\mathbf{Q}_1 \cdot \mathbf{R}_i) + \cos(\mathbf{Q}_2 \cdot \mathbf{R}_i)] \sigma_x \right. \\
 \left. + M_\perp \delta_{\mathbf{R}_i, \mathbf{R}_j} [\sin(\mathbf{Q}_1 \cdot \mathbf{R}_i) \sigma_z + \sin(\mathbf{Q}_2 \cdot \mathbf{R}_i) \sigma_y] \right] \hat{d}_j,
 \end{aligned} \tag{4.17}$$

with nesting taking place along the x and y -direction, as indicated by the yellow arrows in Fig.4.7.(a). With the magnetic texture in question, we cannot perform the usual unitary transformation of the real space Hamiltonian, and therefore we need to employ the momentum

transfer spaces η and ρ as defined in Eq.3.3. However, these only take care of momentum transfer in the direction of \mathbf{Q}_1 , so additionally we employ the following momentum transfers

$$\zeta : \{\mathbf{k}, \mathbf{k} - 4\mathbf{q}_2\}, \quad \lambda : \{\mathbf{k} + \mathbf{q}_2, \mathbf{k} - \mathbf{q}_2\}, \quad (4.18)$$

and extend Eq.3.3. to its 2D analog. The single particle Hamiltonian in Bloch space, with a singlet s -wave superconducting order parameter, takes on the form

$$\begin{aligned} \widehat{\mathcal{H}}(\mathbf{k}) = \widehat{\mathcal{H}}_0(\mathbf{k}) &+ \frac{M_x \rho_x \sigma_x + M_\perp \rho_y \sigma_z}{2} + \frac{M_x \lambda_x \sigma_x + M_\perp \lambda_y \sigma_y}{2} \\ &+ \eta_x \frac{M_x \rho_x \sigma_x - M_\perp \rho_y \sigma_z}{2} + \zeta_x \frac{M_x \lambda_x \sigma_x - M_\perp \lambda_y \sigma_y}{2} + \Delta \tau_x, \end{aligned} \quad (4.19)$$

where $\widehat{\mathcal{H}}_0(\mathbf{k})$ is the dispersion of the system, consisting of the appropriate combinations of $h_i^s(\mathbf{k})$ and the momentum transfer matrices $\{\zeta_z, \eta_z, \lambda_z, \rho_z\}$. In this formalism we find the complex conjugation operation to be $\mathcal{K} = \lambda_x \rho_x \mathcal{K}'$, since the new momentum transfer spaces η and ζ are invariant under complex conjugation, $4\mathbf{q}_l \equiv -4\mathbf{q}_l$. The topological classification in Eq.2.52 is preserved for this Hamiltonian, and the system therefore resides in the class DIII. An external magnetic field can reduce the symmetry of the system, and leave it in the class D, similar to the 1BM in 1D. The class DIII, due to a generalized time-reversal operator squaring to -1 , has Majorana Kramers pairs, whereas class D has chiral Majorana modes, since this class has broken chiral symmetry (see Sec.1.5).

We show in Fig. 4.7 the FS of the 1BM with nesting along \mathbf{Q}_1 and \mathbf{Q}_2 , as indicated by the yellow arrows. Upon folding in both nesting directions, we obtain the seemingly simple FS in Fig.4.7.(c). The RBZ shows two nested points at the FS (yellow dots), whereas the FS in the full BZ, Fig. 4.7.(a), has four (yellow arrows). The folded FS in the RBZ does, in fact, have four nested points, but the folding puts these at the exact same points. The reason for this is that the two pockets in the first BZ are connected by the reciprocal lattice vector $\mathbf{G} = 2\mathbf{Q}_1 + 2\mathbf{Q}_2$ of the RBZ. Bloch's theorem thus tells us that the two pockets at $\Gamma = (0, 0)$ and $M = (\frac{\pi}{a}, \frac{\pi}{a})$ must be located at the same point in the RBZ.

Low Energy Sector

To achieve a physical understanding and intuition about the topological physics arising from the single- and double- \mathbf{Q} nested points, we will in the following project the Hamiltonian onto the low energy sector, similar to the low energy projections of Sec.3.1-3.2. By inspection of Fig. 4.7.(b) we see that nesting at the FS, which by definition is the low energy sector, takes place in the vicinity of Γ and M . The spinor for these low energy systems must be either

$$\psi_{\mathbf{k}}^\dagger = \left(\hat{d}_{\mathbf{k}+\mathbf{q}_1+\mathbf{q}_2}^\dagger, \hat{d}_{\mathbf{k}-\mathbf{q}_1+\mathbf{q}_2}^\dagger, \hat{d}_{\mathbf{k}+\mathbf{q}_1-\mathbf{q}_2}^\dagger, \hat{d}_{\mathbf{k}-\mathbf{q}_1-\mathbf{q}_2}^\dagger \right) \quad (4.20a)$$

or

$$\psi_{\mathbf{k}}^\dagger = \left(\hat{d}_{\mathbf{k}-3\mathbf{q}_1-3\mathbf{q}_2}^\dagger, \hat{d}_{\mathbf{k}+3\mathbf{q}_1-3\mathbf{q}_2}^\dagger, \hat{d}_{\mathbf{k}-3\mathbf{q}_1+3\mathbf{q}_2}^\dagger, \hat{d}_{\mathbf{k}+3\mathbf{q}_1+3\mathbf{q}_2}^\dagger \right). \quad (4.20b)$$

This indicates that the low energy sector is achieved by projecting the Hamiltonian onto the states $|\zeta_z = \pm 1, \eta_z = \pm 1\rangle$. We have illustrated this low energy projection in Fig.4.7.(c). This figure also shows the effect of a projection onto the high energy states, $|\zeta_z = \pm 1, \eta_z = \mp 1\rangle$,

which does not result in a FS, but only nesting at finite energy. Conveniently, the low energy projection also decouples the two pockets in the first BZ, Fig. 4.7.(a), since these only are connected by nesting at finite energy (see the magnetic OPs proportional to η_x or ζ_x in Eq. 4.19). This low energy projection is valid as long as $M_{x\perp}/E_{\text{lim}} \ll 1$, with $E_{\text{lim}} \approx 1.4t$, which is the energy at the nested point connecting the low and the high energy sectors.

We learned from the quasi-1D case, that nesting not only takes place at the FS, but also at finite energy away from it. For nesting along \mathbf{Q}_1 we know that the nested points are $k_{x\text{NP}} = 0$ for each quasi-1D subsystem labeled by k_y . By a C_4 rotation we achieve the nested points for the quasi-1D system with nesting along \mathbf{Q}_2 , *i.e.* with each sub-system, labeled by k_x , and the nested point being $k_{y\text{NP}} = 0$. Evidentially the nested points from both single- \mathbf{Q} systems will intersect at $\mathbf{k}_{\text{DN}} = (0, 0)$, giving rise to a point of double- \mathbf{Q} nesting, see Fig.4.7.(d).

Majorana Flat Bands in Single-Band Model

By focusing on the block of the low energy Hamiltonian, which describes the pocket located at Γ , we find the effective Hamiltonian of the form

$$\begin{aligned} \widehat{\mathcal{H}}'(\mathbf{k}) = \tau_z (h_0^+(\mathbf{k}) + h_1^-(\mathbf{k})\lambda_z + h_2^-(\mathbf{k})\rho_z + h_3^+(\mathbf{k})\lambda_z\rho_z) + \frac{M_x\rho_x\sigma_x + M_\perp\rho_y\sigma_z}{2} \\ + \frac{M_x\lambda_x\sigma_x + M_\perp\lambda_y\sigma_y}{2} + \Delta\tau_x, \end{aligned} \quad (4.21)$$

with $h_i^s(\mathbf{k})$ defined as in Eq. 2.14. We can further expand the low energy Hamiltonian about the single- \mathbf{Q} nested points \mathbf{k}_{NP} by projecting it onto the states that partake in the nesting, obtained through the relation

$$\widehat{\mathcal{H}}'_0(\mathbf{k}_{\text{NP}})|\nu, \mathbf{k}_{\text{NP}}\rangle = \xi_{\text{NP}}|\nu, \mathbf{k}_{\text{NP}}\rangle. \quad (4.22)$$

By projecting the Hamiltonian onto the above obtained states, we find the effective quasi-1D single- \mathbf{Q} nested Hamiltonian;

$$\begin{aligned} \widehat{\mathcal{H}}^{\text{eff.}}(\mathbf{k}) = \tau_z \left(\frac{\xi_{\mathbf{k}+\mathbf{q}_l-\rho\mathbf{q}_\perp} + \xi_{\mathbf{k}-\mathbf{q}_l-\rho\mathbf{q}_\perp}}{2} + \frac{\xi_{\mathbf{k}+\mathbf{q}_l-\rho\mathbf{q}_\perp} - \xi_{\mathbf{k}-\mathbf{q}_l-\rho\mathbf{q}_\perp}}{2}\nu_z \right) + \\ \frac{M_x\nu_x\sigma_x + M_\perp\nu_y\sigma_y}{2} + \Delta\tau_x, \end{aligned} \quad (4.23)$$

with ν acting on the nested bands, with $\rho = \pm 1$ depending on the nested points, and \mathbf{q}_l is the nesting direction, whereas \mathbf{q}_\perp is the direction perpendicular to it. Due to rotational spin invariance, we have picked the magnetic moments to be along the spin x and y axis. Let us for instance take a nested point at $\mathbf{k}_{\text{NP}} = (0, \pm q/8)$, here the nesting direction must be \mathbf{Q}_1 , since the $k_{y\text{NP}}$ labels the given quasi-1D system. For this nested point the ordering wave vectors takes the form $\mathbf{q}_l = \mathbf{q}_1$ and $\mathbf{q}_\perp = \mathbf{q}_2$. Lastly $\rho = +1$ describes the nested point for positive $k_{y\text{NP}}$, and $\rho = -1$ for the negative nested k_y -values. The above Hamiltonian thus describes all single- \mathbf{Q} nested points in the low energy sector. We observe that the Hamiltonian has the symmetry $\nu_z\sigma_z$, which allows us to block diagonalize in the usual way, to obtain

$$\begin{aligned} \widehat{\mathcal{H}}^{\text{eff.}\sigma}(\mathbf{k}) = \tau_z \left(\frac{\xi_{\mathbf{k}+\mathbf{q}_l-\rho\mathbf{q}_\perp} + \xi_{\mathbf{k}-\mathbf{q}_l-\rho\mathbf{q}_\perp}}{2} + \frac{\xi_{\mathbf{k}+\mathbf{q}_l-\rho\mathbf{q}_\perp} - \xi_{\mathbf{k}-\mathbf{q}_l-\rho\mathbf{q}_\perp}}{2}\nu_z \right) + \\ \nu_x \frac{M_x\sigma - M_\perp}{2} + \Delta\tau_x. \end{aligned} \quad (4.24)$$

The observant reader notices that this Hamiltonian is nothing but the 1D 1BM low-energy projected Hamiltonian in Eq.3.28. extended to quasi-1D. Let us in the following focus on the nested point $\mathbf{k}_{\text{NP}} = (0, \pm k_y)$. Since the gap closing takes place at $k_x = 0$, we can linearize the above Hamiltonian about this point, and keep k_y as a free parameter labeling the quasi-1D systems (as long $k_y \neq 0$). The linearized Hamiltonian gets on the form

$$\hat{\mathcal{H}}^{\text{eff.}\sigma}(\mathbf{k}) \approx \tau_z (\xi_{\text{NP}}(k_y) + v_{\text{NP}}(k_y)k_x\nu_z) + \nu_x \frac{M_x\sigma - M_\perp}{2} + \Delta\tau_x, \quad (4.25)$$

with $\xi_{\text{NP}}(k_y) = \sqrt{2}t(1 - \cos(k_y))$, and $v_{\text{NP}}(k_y) = -\sqrt{2}t \cos(k_y)$. By means of the chiral symmetry $\Pi = \tau_y\sigma_z$, we block off-diagonalize the Hamiltonian, and find the k_y -dependent winding

$$w^{k_y\sigma} = \text{Sign}[v_{\text{NP}}(k_y)\Delta] \frac{\text{Sign}\left[\left(\frac{M_x\sigma - M_\perp}{2}\right)^2 - \Delta^2 - \xi_{\text{NP}}^2(k_y)\right]}{2}, \quad (4.26)$$

which indicates that the system will exhibit MFBs, in a certain range in parameter space, as long as $M/E_{\text{lim}} \ll 1$. We have shown in Fig. 4.8.(a) the predicted topological phase diagram obtained from the winding number in Eq.4.26. Each gray line represent the threshold for the topological phase for different k_y -values. In order to verify that the emergent MFs indeed are of the flat band type, we Fourier transformed the real space Hamiltonian in Eq. 4.17 along the y -direction, followed by a folding to the RBZ. The resulting Hamiltonian becomes

$$\begin{aligned} H(k_y) = \sum_{i,j} \hat{d}_{i k_y}^\dagger \left[-t\delta_{i,j\pm a} [h_0(k_y) + h_1(k_y)\zeta_z + h_2(k_y)\lambda_z + h_3(k_y)\zeta_z\lambda_z] \right. \\ \left. + \mu\delta_{i,j} + \frac{M_x\lambda_x\sigma_x + M_\perp\lambda_y\sigma_y}{2} + \zeta_x \frac{M_x\lambda_x\sigma_x - M_\perp\lambda_y\sigma_y}{2} \right. \\ \left. + M_x\delta_{i,j} \cos(QR_i)\sigma_x + M_\perp\delta_{i,j} \sin(QR_i)\sigma_z \right] \hat{d}_{j k_y}, \end{aligned} \quad (4.27)$$

with the summation running over the lattice sites of the quasi-1D chain, and where the functions $h_i(k_y)$ are linear combinations $\cos(k_y)$ shifted with the appropriate momenta. We have shown in Fig.4.8.(b) the energy dispersions of the above Hamiltonian for a open system along the x -direction, *i.e.* like the cylinder in Fig.4.1.(b). We observe that upon going from the trivial region (I), to the topologically non-trivial regime (II) the system exhibits MFBs centered at the RBZ boundaries $\pm q$. Additionally we obtain a feature at $k_y = 0$, which looks like a Dirac cone, however, when we plot the corresponding wave functions, we find them to be highly delocalized, *i.e.* not topologically protected edge modes. This unexplained feature can be some effect from the high energy sector that we do not capture in our approximation, and needs further investigation in a non-approximative manner. Note lastly that the flat bands are four times degenerate, since a Kramers pair occurs at each edge, due to $\Theta^2 = -1$.

Majorana Current in Single-Band Model

Let us now in the following apply the same method, but now for the double- \mathbf{Q} nested point. We use the following relation to find the low energy states of the Hamiltonian at \mathbf{k}_{DN} ;

$$\hat{\mathcal{H}}'_0(\mathbf{k}_{\text{DN}})|\nu \mathbf{k}_{\text{DN}}\rangle = \xi_{\text{DN}}|\nu \mathbf{k}_{\text{DN}}\rangle. \quad (4.28)$$

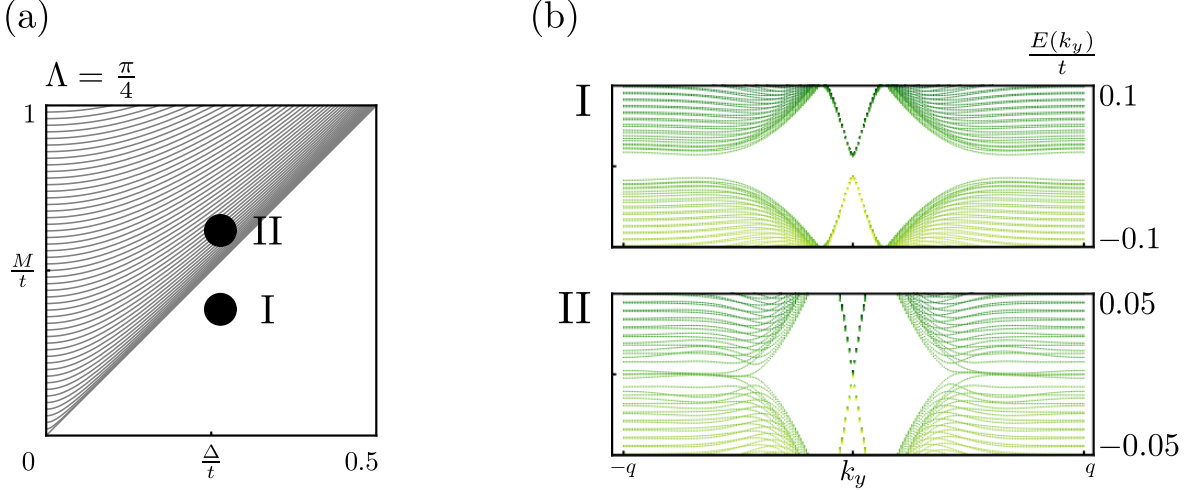


Figure 4.8: (a) Predicted single- \mathbf{Q} phase diagram obtained from the winding number in Eq.4.26 for a set of k_y -values. (b) The energy dispersion of the Hamiltonian in Eq.4.28 upon going from the topologically trivial phase (I), to the topologically non-trivial one (II), as seen in (b). We obtain MFBs centered at the RBZ boundary $k_y = q$, and unexplained features at $k_y = 0$.

All bands in the low energy sector partake in the nesting at this point, and the resulting low energy Hamiltonian, upon linearization about \mathbf{k}_{DN} , is simply

$$\widehat{\mathcal{H}}^{\text{eff.}}(\mathbf{k}) \approx \tau_z (\xi_{\text{DN}} - [k_y \lambda_z + k_x \rho_z]) + \frac{M_x \rho_x \sigma_x + M_{\perp} \rho_y \sigma_z}{2} + \frac{M_x \lambda_x \sigma_x + M_{\perp} \lambda_y \sigma_y}{2} + \Delta \tau_x. \quad (4.29)$$

The Hamiltonian has the following eigenvalues

$$E = \pm \frac{M_x}{2} \pm \frac{1}{2} \sqrt{2M_{\perp}^2 + M_x^2 + 4\Delta^2 + 4\xi_{\text{DN}}^2 \pm 4\sqrt{2M_{\perp}^2 \Delta^2 + M_x^2 \Delta^2 + 2M_{\perp}^2 \xi_{\text{DN}}^2 + M_x^2 \xi_{\text{DN}}^2}} \quad (4.30)$$

where each energy is double degenerate, and one should consider all the combinations of \pm . In the following we will for clarity consider the isotropic case, *i.e.* $\Lambda = \frac{\pi}{4}$, which apply us with a simpler criteria for gap closings at \mathbf{k}_{DN}

$$M = \pm 2\sqrt{2}\sqrt{2\Delta^2 + 2\xi_{\text{DN}}^2 \pm \sqrt{3}(\Delta^2 + \xi_{\text{DN}}^2)}. \quad (4.31)$$

Note that this criteria is not the topological invariant, but can give us knowledge of when a gap closes, which could lead to a topological non-trivial phase.

With the criteria for gap closings at \mathbf{k}_{DN} in Eq.4.31, we have shown the modified predicted phase diagram in Fig.4.9.(a). Alongside this diagram we show the energy dispersions of Eq.4.28 centered at q , for the three points in the phase diagram (I-III). When approaching what we expect to be the helical region in the phase diagram (yellow), we see that the flat bands get tilted, and thereby acquire a velocity, and eventually split up into double degenerate bands (III). By finding the corresponding wave functions, we find that each band has a mode located at opposite edges. Had the velocity of one of the bands been of opposite sign, we

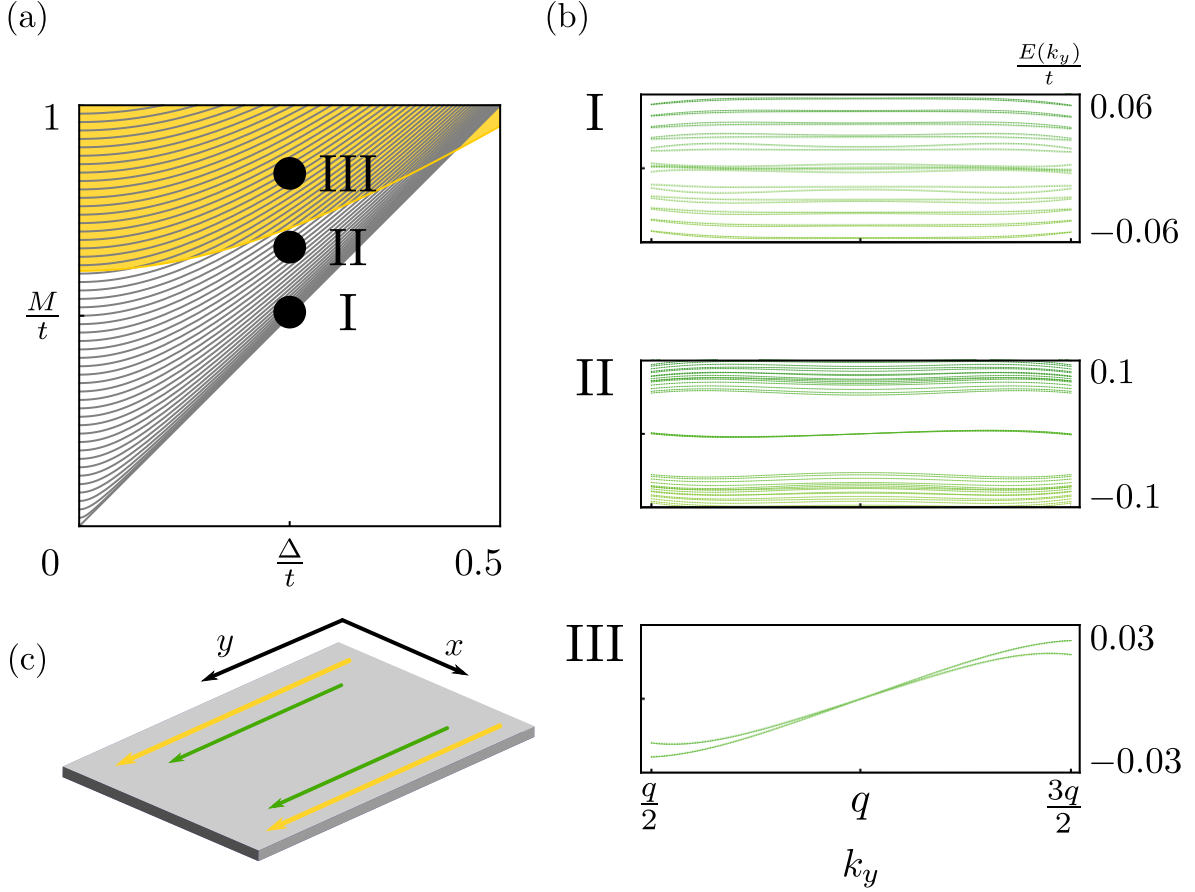


Figure 4.9: (a) Shows the expected phase diagram, with the gray regions indicating a MFB phase, whereas the yellow region is the expected helical phase. (b) The energy dispersion as a function of k_y for the three points (I-III) in parameter space in (a). As the system approaches the helical phase, the flat bands acquire a velocity, but do not become helical since the velocities have the same sign. The system instead carries a supercurrent, as illustrated in (c), where the magnitudes of the arrows indicate the velocity of the modes, *i.e.* the yellow modes originate from the band with the steepest slope.

would indeed obtain the predicted helical edge modes. However, since all the modes have the same sign of the velocity, we conclude that the system experiences a supercurrent, as illustrated in Fig.4.9.(c).

As touched upon earlier, it is possible to make the transition from DIII to D by inclusion of an external magnetic field, say $\hat{\mathcal{H}}_Z = B\sigma_x$. We get the low energy Hamiltonian expanded about the double- \mathbf{Q} nest point to be

$$\begin{aligned} \hat{\mathcal{H}}^{\text{eff.}}(\mathbf{k}) \approx & \tau_z (\xi_{\text{DN}} - (k_y\lambda_z + k_x\rho_z)) + \frac{M_x\rho_x\sigma_x + M_\perp\rho_y\sigma_z}{2} \\ & + \frac{M_x\lambda_x\sigma_x + M_\perp\lambda_y\sigma_y}{2} + B\sigma_x + \Delta\tau_x \end{aligned} \quad (4.32)$$

where we from this equation can find the new established criteria for gap closings, followed by a newly established expected topological phase diagram. We will instead take the Hamiltonian of Eq.4.28, and adiabatically turn on the external magnetic field, and inspect how the energy

dispersions change. We show in Fig.4.10.(a) the dispersions at different strengths of the magnetic field B . In the simulation $M = 0.4t$ and $\Delta = 0.25t$. We see that the field lifts the degeneracy of each band, and makes the bands cross, such that states localized at the same edge become degenerate, and upon $B \sim 1t$ obtains chiral dispersions. In order to make the transition to chiral modes more transparent, we have sketched the development of the dispersion in Fig. 4.10.(b). Lastly are the topologically protected edge modes illustrated in Fig.4.10.(c) for no magnetic field, and $B \sim 1t$.

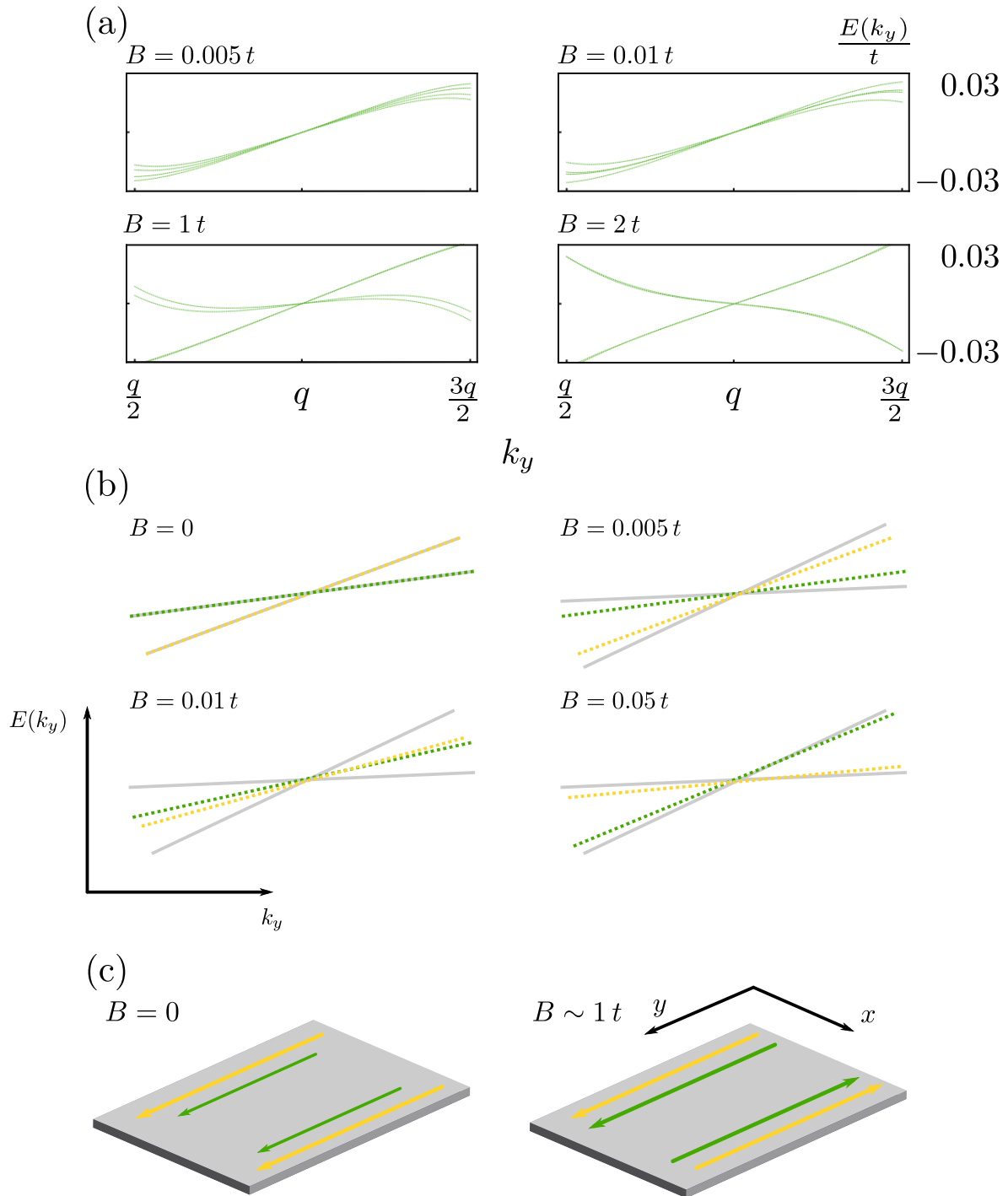


Figure 4.10: (a) Shown is the development of the energy dispersion at different magnetic fields. (b) We show a sketch of the development of the energy dispersion, in order to make the transition to chiral modes more transparent. (c) An illustration of the resulting MF modes for $B = \{0, 1t\}$.

Chapter 5

Conclusions and Outlook

In this thesis we have discussed and explored an alternative method of obtaining topological superconductors, namely through magnetic superconductors. We first established the theory of topological superconductivity, and how it can be induced through magnetic textures. We formulated a general Hamiltonian for the iron-based superconductors, and multi-band superconductors in general, and performed an exhaustive topological classification of the nine predicted magnetic phases coexisting with a general spin-singlet pairing. We found that indeed some of the magnetic textures give rise to topological superconductivity. Furthermore we explored the symmetry point group aspects of the FeSCs, and band models in general, belonging to the group D_{4h} .

We performed a bottom-up approach on the simple single/two-band model in the Double- Q C_4 -symmetric Spin-Whirl Crystal (\bullet) magnetic phase. We first studied the system in 1D, where the magnetic texture in question gets reduced to a magnetic helix, and studied the possible topological phases, and how the inclusion of an additional band changed our results. We found that the 2BM has an inversion symmetry connecting different blocks of the Hamiltonian, which ensured the occurrence of pairs of MFs at the edges. In two dimensions we found that the low energy Hamiltonian expanded about the nested points (gap closing points), can give rise to quasi-1D systems with single- Q nesting, and genuine 2D double- Q nesting. The single- Q nested points give rise to Majorana flat bands, whereas the double- Q were expected to give rise to helical edge modes. However, when simulating the 2D system in the predicted non-trivial helical region, we found instead Majorana currents. These current do come in pairs of two, but these were not helical Majoranas. Upon applying an external magnetic field we found two species chiral Majorana edge modes, since the field reduced the symmetry of the system $D_{III} \rightarrow D$. The discrepancy between the predicted helical edge modes, and the actual Majorana current needs to be studied further, in a non-approximate manner.

In future prospects we would like to study the helical case in greater depth, to see where our approximation fails. Furthermore the 2D analysis should be carried out by defining topological invariants, as for the 1D and quasi-1D cases, instead of simple gap closing criteria. Next natural step is of course to carry out the analysis in 2D for the 2BM, which was commenced but not terminated, and therefore not included here. The two-band model is of paramount importance in understanding the topological physics of multi-band superconductors, since the low energy Hamiltonian in this model can give information about the relevant

pairing functions favoring topological superconductivity. Lastly we would like to apply the obtained knowledge in this thesis, on a more realistic five-orbital model [42], and see for which criteria (intrinsic) topological superconductivity can arise.

Bibliography

- [1] Ettore Majorana. Teoria simmetrica dell'elettrone e del positrone. *Il Nuovo Cimento (1924-1942)*, 14(4):171, Sep 2008.
- [2] K. v. Klitzing, G. Dorda, and M. Pepper. New method for high-accuracy determination of the fine-structure constant based on quantized hall resistance. *Phys. Rev. Lett.*, 45:494–497, Aug 1980.
- [3] B. Andrei Bernevig, Taylor L. Hughes, and Shou-Cheng Zhang. Quantum spin hall effect and topological phase transition in hgte quantum wells. *Science*, 314(5806):1757–1761, 2006.
- [4] F. D. M. Haldane. Model for a quantum hall effect without landau levels: Condensed-matter realization of the "parity anomaly". *Phys. Rev. Lett.*, 61:2015–2018, Oct 1988.
- [5] Panagiotis Kotetes. Topological insulators and superconductors, https://www.tfp.kit.edu/mitarbeiter_245.php 2012/2013.
- [6] Xiao-Liang Qi and Shou-Cheng Zhang. The quantum spin hall effect and topological insulators. *Physics Today*, 63:33–38, 2010.
- [7] A Yu Kitaev. Unpaired majorana fermions in quantum wires. *Physics-Uspekhi*, 44(10S):131, 2001.
- [8] Chetan Nayak, Steven H. Simon, Ady Stern, Michael Freedman, and Sankar Das Sarma. Non-abelian anyons and topological quantum computation. *Rev. Mod. Phys.*, 80:1083–1159, Sep 2008.
- [9] Grigory E. Volovik. *The Universe in a Helium Droplet*. Oxford University Press, 2003.
- [10] A.P Mackenzie and Y Maeno. p-wave superconductivity. *Physica B: Condensed Matter*, 280(1):148 – 153, 2000.
- [11] Jay D. Sau and Sumanta Tewari. Topological superconducting state and majorana fermions in carbon nanotubes. *Phys. Rev. B*, 88:054503, Aug 2013.
- [12] Liang Fu and C. L. Kane. Superconducting proximity effect and majorana fermions at the surface of a topological insulator. *Phys. Rev. Lett.*, 100:096407, Mar 2008.
- [13] Guang Yang, Peter Stano, Jelena Klinovaja, and Daniel Loss. Majorana bound states in magnetic skyrmions. *Phys. Rev. B*, 93:224505, Jun 2016.

- [14] Roman M. Lutchyn, Jay D. Sau, and S. Das Sarma. Majorana fermions and a topological phase transition in semiconductor-superconductor heterostructures. *Phys. Rev. Lett.*, 105:077001, Aug 2010.
- [15] Yuval Oreg, Gil Refael, and Felix von Oppen. Helical liquids and majorana bound states in quantum wires. *Phys. Rev. Lett.*, 105:177002, Oct 2010.
- [16] Martin Leijnse and Karsten Flensberg. Introduction to topological superconductivity and majorana fermions. *Semiconductor Science and Technology*, 27(12):124003, 2012.
- [17] Jason Alicea, Yuval Oreg, Felix von Oppen, and Matthew P. A. Fischer. Non-abelian statistics and topological quantum information processing in 1d wire networks. *Nat Phys*, 7, 2011.
- [18] Morten Kjaergaard, Konrad Wölms, and Karsten Flensberg. Erratum: Majorana fermions in superconducting nanowires without spin-orbit coupling [phys. rev. b 85, 020503(r) (2012)]. *Phys. Rev. B*, 90:059901, Aug 2014.
- [19] M. Z. Hasan and C. L. Kane. Colloquium. *Rev. Mod. Phys.*, 82:3045–3067, Nov 2010.
- [20] Alexander Altland and Martin R. Zirnbauer. Nonstandard symmetry classes in mesoscopic normal-superconducting hybrid structures. *Phys. Rev. B*, 55:1142–1161, Jan 1997.
- [21] Shinsei Ryu, Andreas P Schnyder, Akira Furusaki, and Andreas W W Ludwig. Topological insulators and superconductors: tenfold way and dimensional hierarchy. *New Journal of Physics*, 12(6):065010, 2010.
- [22] Alexei Kitaev. Periodic table for topological insulators and superconductors. *AIP Conference Proceedings*, 1134(1):22–30, 2009.
- [23] Panagiotis Kotetes. Classification of engineered topological superconductors. *New Journal of Physics*, 15(10):105027, 2013.
- [24] Chong Wang, Andrew C. Potter, and T. Senthil. Classification of interacting electronic topological insulators in three dimensions. *Science*, 343(6171):629–631, 2014.
- [25] J.J Sakurai and Jim. J. Napolitano. *Modern Quantum Mechanics*. Person, 2014.
- [26] Sten Rettrup. *Introduction to Group Theoretical Methods in Quantum Chemistry*. Department of Chemistry, University of Copenhagen, 2014.
- [27] M.S. Dresselhaus, G. Dresselhaus, and A. Jorio. *Group Theory: Application to the physics of Condensed Matter*. Springer Berlin Heidelberg, 2008.
- [28] Xiao-Liang Qi, Taylor L. Hughes, and Shou-Cheng Zhang. Topological invariants for the fermi surface of a time-reversal-invariant superconductor. *Phys. Rev. B*, 81:134508, Apr 2010.
- [29] B. Andrei Bernevig and Taylor L. Hughes. *Topological Insulators and Topological Superconductors*. Princeton University Press, 2013.

-
- [30] Sumanta Tewari and Jay D. Sau. Topological invariants for spin-orbit coupled superconductor nanowires. *Phys. Rev. Lett.*, 109:150408, Oct 2012.
- [31] Yoichi Kamihara, Takumi Watanabe, Masahiro Hirano, and Hideo Hosono. Iron-based layered superconductor $\text{La}[\text{O}_{1-x}\text{F}_x]\text{FeAs}$ ($x = 0.05 - 0.12$) with $T_c = 26$ K. *Journal of the American Chemical Society*, 130(11):3296–3297, 2008.
- [32] Rafael M Fernandes and Andrey V Chubukov. Low-energy microscopic models for iron-based superconductors: a review. *Reports on Progress in Physics*, 80(1):014503, 2017.
- [33] Qimiao Si, Rong Yu, and Elihu Abrahams. High-temperature superconductivity in iron pnictides and chalcogenides. *Nature Reviews Materials*, 1, 2016.
- [34] S. Graser, T.A. Maier, P.J. Hirschfeld, and D.J. Scalapino. Near-degeneracy of several pairing channels in multiorbital models for the fe pnictides. *New Journal of Physics*, 11, 2009.
- [35] L. Wang, F. Hardy, A. E. Böhmer, T. Wolf, P. Schweiss, and C. Meingast. Complex phase diagram of $\text{Ba}_{1-x}\text{Na}_x\text{Fe}_2\text{As}_2$: A multitude of phases striving for the electronic entropy. *Phys. Rev. B*, 93:014514, Jan 2016.
- [36] M.N. Gastiasoro. Bogoliubov-de gennes studies of fe-based superconductors. Master’s thesis, University of Copenhagen, 2013.
- [37] Maria N. Gastiasoro and Brian M. Andersen. Competing magnetic double- q phases and superconductivity-induced reentrance of C_2 magnetic stripe order in iron pnictides. *Phys. Rev. B*, 92:140506, Oct 2015.
- [38] P J Hirschfeld, M M Korshunov, and I I Mazin. Gap symmetry and structure of fe-based superconductors. *Reports on Progress in Physics*, 74(12):124508, 2011.
- [39] Morten H. Christensen, Brian M. Andersen, and Panagiotis Kotetes. Unravelling incommensurate magnetism and the path to intrinsic topological superconductivity in iron-pnictides, [arXiv:1612.07633](https://arxiv.org/abs/1612.07633) [cond-mat.supr-con] 2016.
- [40] Alexander Altland and Ben D. Simons. *Second quantization*, page 39–94. Cambridge University Press, 2 edition, 2010.
- [41] Karsten Flensberg and Henrik Bruus. *Many-Body Quantum Theory in Condensed Matter Physics*. Oxford Graduate Texts, 2004.
- [42] Hiroaki Ikeda, Ryotaro Arita, and Jan Kuneš. Phase diagram and gap anisotropy in iron-pnictide superconductors. *Phys. Rev. B*, 81:054502, Feb 2010.
- [43] S. Raghu, Xiao-Liang Qi, Chao-Xing Liu, D. J. Scalapino, and Shou-Cheng Zhang. Minimal two-band model of the superconducting iron oxypnictides. *Phys. Rev. B*, 77:220503, Jun 2008.

- [44] Nobumi Miyawaki and Hiroshi Shimahara. Phase transition to the fulde–ferrell–larkin–ovchinnikov state in a quasi-one-dimensional organic superconductor with anion order. *Journal of Physics: Conference Series*, 702(1):012002, 2016.
- [45] D. Mandler. Topological phases in systems with coexisting density waves and superconductivity. Diploma thesis, Karlsruhe Institut für Technologie, 2012.
- [46] Mark H Fischer. Gap symmetry and stability analysis in the multi-orbital fe-based superconductors. *New Journal of Physics*, 15(7):073006, 2013.
- [47] Manfred Sgrist and Kazuo Ueda. Phenomenological theory of unconventional superconductivity. *Rev. Mod. Phys.*, 63:239–311, Apr 1991.
- [48] Morten H. Christensen, Daniel D. Scherer, Panagiotis Kotetes, and Brian M. Andersen. On the role of multiorbital effects in the magnetic phase diagram of iron-pnictides, [arXiv:1704.07862 \[cond-mat.supr-con\]](https://arxiv.org/abs/1704.07862) 2017.
- [49] WebQC. Point croup character tables, July 2017. <http://www.webqc.org/symmetrypointgroup-d4h.html>.
- [50] Andreas Heimes, Daniel Mandler, and Panagiotis Kotetes. Interplay of topological phases in magnetic adatom-chains on top of a rashba superconducting surface. *New Journal of Physics*, 17(2):023051, 2015.
- [51] R. Frésard and G. Kotliar. Interplay of mott transition and ferromagnetism in the orbitally degenerate hubbard model. *Physical Review B*, 20, 1997.
- [52] E. Dagotto, T. Hotta, and A. Moreo. Colossal magnetoresistant materials: The key role of phase separation. *Physical Reports*, 344, 2001.

Appendix A

SU(N) Generators

SU(2) Pauli Matrices

$$\sigma_x = \begin{pmatrix} 0 & 1 \\ 1 & 0 \end{pmatrix}, \quad \sigma_y = \begin{pmatrix} 0 & -i \\ i & 0 \end{pmatrix}, \quad \sigma_z = \begin{pmatrix} 1 & 0 \\ 0 & -1 \end{pmatrix}. \quad (\text{A.1})$$

Appendix B

Mean-Field Decoupling Approach

This appendix will give a short review on mean-field decoupling of a general interaction, followed by a decoupling in the magnetic channel of the interaction in Eq.2.7. We also show how an effective attractive interaction for the FeSCs can be decoupled in the Cooper channel.

General Mean-Field in Electron-Hole Channel

Let us start with a general interaction represented in second quantization, with the quantum numbers α , β , γ and δ

$$H_{\text{int}} = \sum_{\alpha\beta\gamma\delta} V^{\alpha\beta\gamma\delta} c_{\alpha}^{\dagger} c_{\beta}^{\dagger} c_{\gamma} c_{\delta}, \quad (\text{B.1})$$

where c_{α} annihilates an electron with quantum number α . Furthermore we have the matrix element

$$V^{\alpha\beta\gamma\delta} = \langle \alpha, \beta | \hat{V} | \gamma, \delta \rangle \quad (\text{B.2})$$

where \hat{V} is some two body operator. With this interaction we will perform a mean-field decoupling in the electron-hole channel, *i.e.* channels of the form $\langle c_{\alpha}^{\dagger} c_{\beta} \rangle$. To do this we assume that the operators deviate only little from their expectation values

$$c_{\alpha}^{\dagger} c_{\beta} \approx \langle c_{\alpha}^{\dagger} c_{\beta} \rangle + \underbrace{\left\{ c_{\alpha}^{\dagger} c_{\beta} - \langle c_{\alpha}^{\dagger} c_{\beta} \rangle \right\}}_{\text{Small deviation}}, \quad (\text{B.3})$$

where the second term is the fluctuation, and is only taken to linear order. From this we get the direct term

$$H_{\text{Hartree}}^{\text{MF}} = \sum_{\alpha\beta\gamma\delta} V^{\alpha\beta\gamma\delta} \left(c_{\alpha}^{\dagger} c_{\delta} \delta_{\beta,\gamma} - 2c_{\alpha}^{\dagger} c_{\gamma} \langle c_{\beta}^{\dagger} c_{\delta} \rangle + \langle c_{\alpha}^{\dagger} c_{\gamma} \rangle \langle c_{\beta}^{\dagger} c_{\delta} \rangle \right) \quad (\text{B.4})$$

and the Fock term

$$H_{\text{Fock}}^{\text{MF}} = \sum_{\alpha\beta\gamma\delta} V^{\alpha\beta\gamma\delta} \left(-c_{\alpha}^{\dagger} c_{\gamma} \delta_{\beta,\delta} + 2c_{\alpha}^{\dagger} c_{\delta} \langle c_{\beta}^{\dagger} c_{\gamma} \rangle - \langle c_{\alpha}^{\dagger} c_{\delta} \rangle \langle c_{\beta}^{\dagger} c_{\gamma} \rangle \right), \quad (\text{B.5})$$

where we have used $\langle \alpha, \beta | \hat{V} | \gamma, \delta \rangle = \langle \beta, \alpha | \hat{V} | \delta, \gamma \rangle$, since $|\alpha, \beta\rangle = \frac{1}{\sqrt{2}} (|\alpha\rangle \otimes |\beta\rangle - |\beta\rangle \otimes |\alpha\rangle)$, which is clearly anti-symmetric under quantum number exchange.

General Mean-Field in Cooper Channel

When formulating a general mean-field decoupling in the Cooper channel, *i.e.* channels of the form $\langle c_\alpha^\dagger c_\beta^\dagger \rangle$, we again start with the general interaction in Eq.B.1. However, now \hat{V} represents a general effective electron electron interaction, which is attractive near the Fermi Surface, resulting in an instability of the Fermi gas. We therefore end up with

$$H_{\text{int}} = - \sum_{\alpha\beta\gamma\delta} V^{\alpha\beta\gamma\delta} c_\alpha^\dagger c_\beta^\dagger c_\gamma c_\delta, \quad (\text{B.6})$$

and assume that the operators can be described by their expectation values,

$$c_\alpha^\dagger c_\beta^\dagger \approx \langle c_\alpha^\dagger c_\beta^\dagger \rangle + \underbrace{\left\{ \langle c_\alpha^\dagger c_\beta^\dagger \rangle - \langle c_\alpha^\dagger c_\beta^\dagger \rangle \right\}}_{\text{Small deviation}}, \quad (\text{B.7})$$

and thereby produce an effective Hamiltonian bilinear in creation and annihilation operators. After the decoupling we obtain the Hamiltonian

$$H_{\text{BCS}}^{\text{MF}} = - \sum_{\alpha\beta\gamma\delta} V^{\alpha\beta\gamma\delta} \left(c_\alpha^\dagger c_\beta^\dagger \langle c_\gamma c_\delta \rangle + c_\gamma c_\delta \langle c_\alpha^\dagger c_\beta^\dagger \rangle - \langle c_\alpha^\dagger c_\beta^\dagger \rangle \langle c_\gamma c_\delta \rangle \right). \quad (\text{B.8})$$

For later purposes we will also here define a general superconducting order parameter in the way

$$\Delta_{\alpha\beta} = - \sum_{\gamma\delta} V^{\alpha\beta\gamma\delta} \langle c_\gamma c_\delta \rangle, \quad \Delta_{\alpha\beta}^* = - \sum_{\gamma\delta} V^{\delta\gamma\beta\alpha} \langle c_\delta^\dagger c_\gamma^\dagger \rangle. \quad (\text{B.9})$$

Where we have used $\langle \alpha, \beta | \hat{V} | \gamma, \delta \rangle^* = \langle \delta, \gamma | \hat{V}^\dagger | \beta, \alpha \rangle$, and in order for the two-particle operator to be an observable with real eigenvalues we must have $\hat{V}^\dagger = \hat{V}$. Notice again, that if we interchange two quantum numbers we get a minus, due to the fermionic nature of the particles, *i.e.* $\Delta_{\alpha\beta} = -\Delta_{\beta\alpha}$. So we arrive at the well-known BCS Hamiltonian

$$H_{\text{BCS}}^{\text{MF}} = \sum_{\alpha\beta} \left(c_\alpha^\dagger \Delta_{\alpha\beta} c_\beta^\dagger - c_\beta \Delta_{\beta\alpha}^* c_\alpha \right) + \sum_{\alpha\beta\gamma\delta} \Delta_{\delta\gamma}^* (V^{-1})^{\gamma\delta\alpha\beta} \Delta_{\alpha\beta}. \quad (\text{B.10})$$

The Case of Iron-Based Superconductors

The 3d-electrons of the Fe-atoms are assumed to be localized at each atom, and we can therefore simplify the interaction to be the on-site Coulomb-interaction. Inserting this interaction in the general expression in Eq.B.1, and by doing the following transformation

$$c_\alpha^\dagger = \sum_i \sum_\mu \sum_\sigma \langle i\mu\sigma | \alpha \rangle d_{i\mu\sigma}^\dagger, \quad (\text{B.11})$$

we obtain the interaction

$$H_{\text{int}} = \frac{1}{2} \sum_{\sigma\sigma'} \sum_{\mu\nu\nu'} \sum_i d_{i\mu\sigma}^\dagger d_{i\nu\sigma'}^\dagger V^{\mu\nu\nu'\mu'} d_{i\nu'\sigma'} d_{i\mu'\sigma} \quad (\text{B.12})$$

where we have the matrix element defined as (after inserting four resolutions of identity $\mathbb{1} = \int d\mathbf{r} |\mathbf{r}\rangle \langle \mathbf{r}|$)

$$\langle \mu, \nu | \hat{V} | \nu', \mu' \rangle = \int d\mathbf{r} d\mathbf{r}' \langle \mu | \mathbf{r} \rangle \langle \nu | \mathbf{r}' \rangle V(\mathbf{r}, \mathbf{r}') \langle \mathbf{r}' | \nu' \rangle \langle \mathbf{r} | \mu' \rangle. \quad (\text{B.13})$$

The main contributions come from matrix elements involving only two different orbitals [51]. With this at mind we can rewrite the interaction in four distinct terms; the intra-orbital Coulomb interaction, the pair-hopping, the inter-orbital Coulomb interaction and the Hund's coupling interaction, as respectively shown below

$$H_{\text{int}}^{(1)} = \sum_i \sum_{\mu} U n_{i\mu\uparrow} n_{i\mu\downarrow} \quad (\text{B.14a})$$

$$H_{\text{int}}^{(2)} = \frac{1}{2} \sum_i \sum_{\mu \neq \nu} \sum_{\sigma} J' d_{i\mu\sigma}^{\dagger} d_{i\mu\bar{\sigma}}^{\dagger} d_{i\nu\bar{\sigma}} d_{i\nu\sigma} \quad (\text{B.14b})$$

$$H_{\text{int}}^{(3)} = \frac{1}{2} \sum_i \sum_{\mu \neq \nu} \sum_{\sigma} U' (n_{i\mu\sigma} n_{i\nu\sigma} + n_{i\mu\sigma} n_{i\nu\bar{\sigma}}) \quad (\text{B.14c})$$

$$H_{\text{int}}^{(4)} = -\frac{1}{2} \sum_i \sum_{\mu \neq \nu} \sum_{\sigma} J (n_{i\mu\sigma} n_{i\nu\sigma} - d_{i\mu\sigma}^{\dagger} d_{i\nu\bar{\sigma}}^{\dagger} d_{i\mu\bar{\sigma}} d_{i\nu\sigma}), \quad (\text{B.14d})$$

where we have redefined the matrix elements as follows

$$U = \langle \mu, \mu | \hat{V} | \mu, \mu \rangle, \quad J' = \langle \mu, \mu | \hat{V} | \nu, \nu \rangle, \quad U' = \langle \mu, \nu | \hat{V} | \nu, \mu \rangle \quad J = \langle \mu, \nu | \hat{V} | \mu, \nu \rangle. \quad (\text{B.15})$$

We assume rotational invariance, and thereby have the conditions $J = J'$ and $U' = U - 2J$ [37, 51, 52]. Since we are interested in the development of magnetic instabilities, and thereby the possible topological phases, we will only consider the term

$$\begin{aligned} H_{\text{int}}^{(4)} &= - \sum_i \sum_{\mu \neq \nu} \sum_{\sigma} \frac{J}{2} (n_{i\mu\sigma} n_{i\nu\sigma} - d_{i\mu\sigma}^{\dagger} d_{i\nu\bar{\sigma}}^{\dagger} d_{i\mu\bar{\sigma}} d_{i\nu\sigma}) \\ &= - \sum_i \sum_{\mu \neq \nu} J \left(\mathbf{S}_i^{\mu} \cdot \mathbf{S}_i^{\nu} + \sum_{\sigma} \frac{1}{4} (n_{i\mu\sigma} n_{i\nu\sigma} + n_{i\mu\bar{\sigma}} n_{i\nu\sigma}) \right). \end{aligned} \quad (\text{B.16})$$

Magnetic Channel for Fe-Pnictides

We will here do the mean-field decoupling on the Hund's coupling, *i.e.* first term in Eq.B.16, and get

$$\begin{aligned} H_{\text{int}}^{\text{Hund}} &= - \sum_i \sum_{\mu \neq \nu} J \mathbf{S}_i^{\mu} \cdot \mathbf{S}_i^{\nu} = - \sum_i \sum_{\mu \neq \nu} \sum_{\alpha\beta\gamma\delta} \frac{J}{4} d_{i\mu\alpha}^{\dagger} \boldsymbol{\sigma}_{\alpha\beta} d_{i\mu\beta} \cdot d_{i\nu\gamma}^{\dagger} \boldsymbol{\sigma}_{\gamma\delta} d_{i\nu\delta} \\ &= - \sum_i \sum_{\mu \neq \nu} \sum_{\alpha\beta\gamma\delta} \frac{J}{4} d_{i\mu\alpha}^{\dagger} d_{i\mu\beta} d_{i\nu\gamma}^{\dagger} d_{i\nu\delta} (2\delta_{\alpha,\delta} \delta_{\beta,\gamma} - \delta_{\alpha,\beta} \delta_{\gamma,\delta}) \end{aligned} \quad (\text{B.17})$$

where we have used the relation $\boldsymbol{\sigma}_{\alpha\beta} \cdot \boldsymbol{\sigma}_{\gamma\delta} = 2\delta_{\alpha,\delta} \delta_{\beta,\gamma} - \delta_{\alpha,\beta} \delta_{\gamma,\delta}$. Now we simply need to apply the general expression for the mean-field decoupling from above. Starting with the Hartree-term

$$\begin{aligned} H_{\text{Hartree}}^{\text{MF}} &= \sum_i \sum_{\mu \neq \nu} \sum_{\alpha\beta\gamma\delta} \frac{J}{4} \left(\langle d_{i\mu\alpha}^{\dagger} d_{i\mu\beta} \rangle \langle d_{i\nu\gamma}^{\dagger} d_{i\nu\delta} \rangle - 2d_{i\mu\alpha}^{\dagger} d_{i\mu\beta} \langle d_{i\nu\gamma}^{\dagger} d_{i\nu\delta} \rangle \right) (2\delta_{\alpha,\delta} \delta_{\beta,\gamma} - \delta_{\alpha,\beta} \delta_{\gamma,\delta}) \\ &= \sum_i \sum_{\mu \neq \nu} \frac{J}{4} \left(\langle \hat{d}_{i\mu}^{\dagger} \boldsymbol{\sigma} \hat{d}_{i\mu} \rangle \cdot \langle \hat{d}_{i\nu}^{\dagger} \boldsymbol{\sigma} \hat{d}_{i\nu} \rangle - 2\hat{d}_{i\mu}^{\dagger} \boldsymbol{\sigma} \hat{d}_{i\mu} \cdot \langle \hat{d}_{i\nu}^{\dagger} \boldsymbol{\sigma} \hat{d}_{i\nu} \rangle \right), \end{aligned} \quad (\text{B.18})$$

with $\hat{d}_{i\mu}^\dagger = (d_{i\mu\uparrow}^\dagger, d_{i\mu\downarrow}^\dagger)$. And similar for the Fock-term

$$H_{\text{Fock}}^{\text{MF}} = \sum_i \sum_{\mu \neq \nu} \sum_{\alpha\beta\gamma\delta} \frac{J}{4} (2\delta_{\alpha,\delta}\delta_{\beta,\gamma} - \delta_{\alpha,\beta}\delta_{\gamma,\delta}) \times \left(-\langle d_{i\mu\alpha}^\dagger d_{i\nu\delta} \rangle \langle d_{i\nu\gamma}^\dagger d_{i\mu\beta} \rangle + 2d_{i\mu\alpha}^\dagger d_{i\nu\delta} \langle d_{i\nu\gamma}^\dagger d_{i\mu\beta} \rangle - d_{i\mu\alpha}^\dagger d_{i\mu\beta} \delta_{\delta,\gamma} \right). \quad (\text{B.19})$$

To get this expression on a form similar to the last line in Eq.B.18, we interchange the spin indices δ and β , and split the expression up as follows

$$H_{\text{Fock}}^{\text{MF}} = \sum_i \sum_{\mu \neq \nu} \sum_{\alpha\beta\gamma\delta} \frac{J}{4} \left[\frac{1}{2} \left(\langle d_{i\mu\alpha}^\dagger d_{i\nu\beta} \rangle \langle d_{i\nu\gamma}^\dagger d_{i\mu\delta} \rangle - 2d_{i\mu\alpha}^\dagger d_{i\nu\beta} \langle d_{i\nu\gamma}^\dagger d_{i\mu\delta} \rangle \right) (2\delta_{\alpha,\delta}\delta_{\gamma,\beta} - \delta_{\alpha,\beta}\delta_{\delta,\gamma}) - \frac{3}{2} \left(\langle d_{i\mu\alpha}^\dagger d_{i\nu\beta} \rangle \langle d_{i\nu\gamma}^\dagger d_{i\mu\delta} \rangle \langle -2d_{i\mu\alpha}^\dagger d_{i\nu\beta} \langle d_{i\nu\gamma}^\dagger d_{i\mu\delta} \rangle \right) \delta_{\alpha,\beta}\delta_{\delta,\gamma} + d_{i\mu\alpha}^\dagger d_{i\mu\delta} \delta_{\gamma,\delta} (\delta_{\alpha,\delta}\delta_{\gamma,\beta} - 2\delta_{\alpha,\beta}\delta_{\delta,\gamma}) \right]. \quad (\text{B.20})$$

If we know evaluate the Kronecker deltas, and define the charge density operator $n_{\mu\nu} = \sum_\sigma d_{i\mu\sigma}^\dagger d_{i\nu\sigma}$ we get the Fock term on the form

$$H_{\text{Fock}}^{\text{MF}} = \sum_i \sum_{\mu \neq \nu} \frac{J}{4} \left(\frac{1}{2} \langle \hat{d}_{i\mu}^\dagger \boldsymbol{\sigma} \hat{d}_{i\nu} \rangle \cdot \langle \hat{d}_{i\nu}^\dagger \boldsymbol{\sigma} \hat{d}_{i\mu} \rangle - \hat{d}_{i\mu}^\dagger \boldsymbol{\sigma} \hat{d}_{i\nu} \cdot \langle \hat{d}_{i\nu}^\dagger \boldsymbol{\sigma} \hat{d}_{i\mu} \rangle - \frac{3}{2} \langle n_{\mu\nu} \rangle \langle n_{\mu\nu} \rangle + 3n_{\mu\nu} \langle n_{\nu\mu} \rangle - n_{\mu\mu} \right). \quad (\text{B.21})$$

For the topological classifications later on, we will only consider the magnetic order parameters, and hence not focus on the charge density orders. This results in the total magnetic Hamiltonian

$$H_{\text{mag}} = \sum_i \sum_{\mu \neq \nu} J \left(-\frac{1}{2} \hat{d}_{i\mu}^\dagger \boldsymbol{\sigma} \hat{d}_{i\mu} \cdot \langle \hat{d}_{i\nu}^\dagger \boldsymbol{\sigma} \hat{d}_{i\nu} \rangle - \frac{1}{4} \hat{d}_{i\mu}^\dagger \boldsymbol{\sigma} \hat{d}_{i\nu} \cdot \langle \hat{d}_{i\nu}^\dagger \boldsymbol{\sigma} \hat{d}_{i\mu} \rangle + \frac{1}{4} \langle \hat{d}_{i\mu}^\dagger \boldsymbol{\sigma} \hat{d}_{i\mu} \rangle \cdot \langle \hat{d}_{i\nu}^\dagger \boldsymbol{\sigma} \hat{d}_{i\nu} \rangle + \frac{1}{8} \langle \hat{d}_{i\mu}^\dagger \boldsymbol{\sigma} \hat{d}_{i\nu} \rangle \cdot \langle \hat{d}_{i\nu}^\dagger \boldsymbol{\sigma} \hat{d}_{i\mu} \rangle \right). \quad (\text{B.22})$$

At this point we will now define the magnetic order parameters in the way

$$\mathbf{M}_i^{\mu\mu} = -\frac{J}{2} \langle \hat{d}_{i\nu}^\dagger \boldsymbol{\sigma} \hat{d}_{i\nu} \rangle, \quad \mathbf{M}_i^{\mu\nu} = -\frac{J}{4} \langle \hat{d}_{i\nu}^\dagger \boldsymbol{\sigma} \hat{d}_{i\mu} \rangle \quad (\text{B.23})$$

and get the Hamiltonian

$$H_{\text{mag}} = \sum_i \sum_{\mu \neq \nu} \left(\hat{d}_{i\mu}^\dagger \mathbf{M}_i^{\mu\mu} \cdot \boldsymbol{\sigma} \hat{d}_{i\mu} + \hat{d}_{i\mu}^\dagger \mathbf{M}_i^{\mu\nu} \cdot \boldsymbol{\sigma} \hat{d}_{i\nu} + \frac{\mathbf{M}_i^{\nu\nu} \cdot \mathbf{M}_i^{\mu\mu} + 2|\mathbf{M}_i^{\mu\nu}|^2}{J} \right) \quad (\text{B.24})$$

We transform to Bloch-space, since the system is considered to be translational invariant, and introduce the transformed operators between Bloch and Wannier space

$$d_{\mathbf{k}\mu\sigma}^\dagger = \frac{1}{\sqrt{N}} \sum_i e^{i\mathbf{k}\cdot\mathbf{R}_i} d_{i\mu\sigma}^\dagger, \quad \iff \quad d_{i\mu\sigma}^\dagger = \frac{1}{\sqrt{N}} \sum_{\mathbf{k}} e^{-i\mathbf{k}\cdot\mathbf{R}_i} d_{\mathbf{k}\mu\sigma}^\dagger \quad (\text{B.25})$$

and thereby get

$$H_{\text{mag}}(\mathbf{k}) = \sum_{\mathbf{k}} \sum_{\mathbf{q}_l} \sum_{\mu \neq \nu} \left(\hat{d}_{\mathbf{k}+\mathbf{q}_l\mu}^\dagger \mathbf{M}_l^{\mu\mu} \cdot \boldsymbol{\sigma} \hat{d}_{\mathbf{k}-\mathbf{q}_l\mu} + \hat{d}_{\mathbf{k}+\mathbf{q}_l\mu}^\dagger \mathbf{M}_l^{\mu\nu} \cdot \boldsymbol{\sigma} \hat{d}_{\mathbf{k}-\mathbf{q}_l\nu} \right) + \sum_{\mathbf{q}_l} \sum_{\mu \neq \nu} \frac{\mathbf{M}_l^{\mu\mu} \cdot \mathbf{M}_l^{\nu\nu} + 2|\mathbf{M}_l^{\mu\nu}|^2}{J}. \quad (\text{B.26})$$

Note here that the \mathbf{q}_l -sum runs over all the nesting vectors, $\mathbf{Q}_l = 2\mathbf{q}_l$, on the Fermi surface. We have in the above used the Bloch representation of the magnetic order parameters

$$\mathbf{M}_l^{\mu\nu} = \frac{1}{N} \sum_i \mathbf{M}_i^{\mu\nu} e^{-i\mathbf{Q}_l \cdot \mathbf{R}_i}, \quad \Longleftrightarrow \quad \mathbf{M}_i^{\mu\nu} = \sum_{\mathbf{Q}_l} \mathbf{M}_l^{\mu\nu} e^{i\mathbf{Q}_l \cdot \mathbf{R}_i}. \quad (\text{B.27})$$

Cooper Channel for Fe-Pnictides

Through the same procedure, but now with a general effective electron electron interaction, \hat{V}_{eff} , we obtain the BCS Hamiltonian in Wannier-space

$$H_{\text{BCS}} = - \sum_{ij} \sum_{\mu\nu\lambda\kappa} \sum_{\alpha\beta\gamma\delta} V_{ij,\alpha\beta\gamma\delta}^{\mu\nu\lambda\kappa} d_{i\mu\alpha}^\dagger d_{j\nu\beta}^\dagger d_{j\lambda\gamma} d_{i\kappa\delta}, \quad (\text{B.28})$$

with the matrix element defined as

$$V_{ij,\alpha\beta\gamma\delta}^{\mu\nu\lambda\kappa} = \langle i\mu\alpha, j\nu\beta | \hat{V}_{\text{eff}} | j\lambda\gamma, i\kappa\delta \rangle = \int d\mathbf{r} d\mathbf{r}' \langle \alpha\mu | \mathbf{r} \rangle \langle \beta\nu | \mathbf{r}' \rangle V_{\text{eff}}(\mathbf{r}, \mathbf{r}') \langle \mathbf{r}' | \lambda\gamma \rangle \langle \mathbf{r} | \kappa\delta \rangle \quad (\text{B.29})$$

where $\{\alpha, \beta, \gamma, \delta\}$ are spin labels, and $\{\mu, \nu, \lambda, \kappa\}$ the orbital labels. Notice that we have such a matrix element, since the interaction could be spin, orbital and lattice dependent. After a mean-field decoupling, using the general expression in section.B, we end up with the Hamiltonian

$$H_{\text{BCS}}^{\text{MF}} = \sum_{ij} \sum_{\mu\nu} \sum_{\alpha\beta} \left(d_{i\mu\alpha}^\dagger \Delta_{ij,\alpha\beta}^{\mu\nu} d_{j\nu\beta}^\dagger + \text{h.c.} \right) + \sum_{ij} \sum_{\mu\nu\lambda\kappa} \sum_{\alpha\beta\gamma\delta} \left(\Delta_{ji,\gamma\delta}^{\kappa\lambda} \right)^* (V^{-1})_{ij,\gamma\delta\alpha\beta}^{\lambda\kappa\mu\nu} \Delta_{ij,\alpha\beta}^{\mu\nu}, \quad (\text{B.30})$$

with the following order parameters

$$\Delta_{ij,\alpha\beta}^{\mu\nu} = - \sum_{\lambda\kappa} \sum_{\gamma\delta} V_{ij,\alpha\beta\gamma\delta}^{\mu\nu\lambda\kappa} \langle d_{j\lambda\gamma} d_{i\kappa\delta} \rangle, \quad \left(\Delta_{\alpha\beta}^{\mu\nu} \right)^* = - \sum_{\lambda\kappa} \sum_{\gamma\delta} V_{ij,\delta\gamma\beta\alpha}^{\kappa\lambda\nu\mu} \langle d_{i\kappa\delta}^\dagger d_{j\lambda\gamma}^\dagger \rangle. \quad (\text{B.31})$$

Again we would like to go from Wannier to Bloch spaces through the definitions in in Eq.B.25. For simplicity we will not include the constant term, and thereby obtain the final BCS Hamiltonian in reciprocal space

$$H_{\text{BCS}}(\mathbf{k}) = \sum_{\mathbf{k}\mathbf{q}} \sum_{\mu\nu} \sum_{\alpha\beta} \left(d_{\mathbf{k}+\mathbf{q}/2,\mu\alpha}^\dagger \Delta_{\mathbf{k}\mathbf{q},\alpha\beta}^{\mu\nu} d_{-\mathbf{k}+\mathbf{q}/2,\nu\beta}^\dagger + \text{h.c.} \right), \quad (\text{B.32})$$

where the total momentum of the Cooper pair \mathbf{q} , usually is zero. Note we have defined the Bloch representation of the pairing potential as

$$\Delta_{\mathbf{k}\mathbf{q},\alpha\beta}^{\mu\nu} = \frac{1}{N} \sum_{ij} \Delta_{ij,\alpha\beta}^{\mu\nu} e^{-i\mathbf{k} \cdot (\mathbf{R}_i - \mathbf{R}_j)} e^{-i\mathbf{q} \cdot \frac{\mathbf{R}_i + \mathbf{R}_j}{2}}, \quad \Longleftrightarrow \quad \Delta_{ij,\alpha\beta}^{\mu\nu} = \sum_{\mathbf{k}\mathbf{q}} \Delta_{\mathbf{k}\mathbf{q},\alpha\beta}^{\mu\nu} e^{i\mathbf{k} \cdot (\mathbf{R}_i - \mathbf{R}_j)} e^{i\mathbf{q} \cdot \frac{\mathbf{R}_i + \mathbf{R}_j}{2}} \quad (\text{B.33})$$

Where we see that \mathbf{q} is the momentum of the center of mass of the cooper pair, and \mathbf{k} is simply the relative momentum.

Appendix C

Topological Classification of FeSCs

We will in this appendix carry out all the topological classifications for the nine magnetic phases discussed in Chap. 2 coexisting with superconductivity. All the magnetic profiles are listed in Eqs. 2.2 and Eq. 2.3. In order to obtain the BdG Hamiltonian, one should Fourier transform the magnetic profiles and insert them in Eq. 2.48, as done in Sec.2.3. When a Hamiltonian has a symmetry $\hat{\mathcal{O}}$, *i.e.* $[\hat{\mathcal{H}}(\mathbf{k}), \hat{\mathcal{O}}] = 0$, we can simultaneously block diagonalize the two matrices and label each block by the eigenvalues of $\hat{\mathcal{O}}$.

Single- \mathbf{Q} Stripe Phase

Since this magnetic phase is single- \mathbf{Q} nested, we only need to do the folding along the nesting wave vector \mathbf{Q} . Additionally we find the Hamiltonian to have the symmetry σ_y . The block diagonalized Hamiltonian thus takes the form

$$\begin{aligned} \hat{\mathcal{H}}^\sigma(\mathbf{k}) = & \tau_z \left[\hat{h}_0^+(\mathbf{k}) + \hat{h}_2^-(\mathbf{k})\rho_z \right] + \sigma \frac{\widehat{M}_z \rho_x}{2} \\ & + \tau_x \left[\hat{\Delta}_0^{+\text{Re}}(\mathbf{k}) + \hat{\Delta}_2^{-\text{Re}}(\mathbf{k})\rho_z \right] - \tau_y \left[\hat{\Delta}_0^{+\text{Im}}(\mathbf{k}) + \hat{\Delta}_2^{-\text{Im}}(\mathbf{k})\rho_z \right]. \end{aligned} \quad (\text{C.1})$$

In this basis complex conjugation is defined as $\mathcal{K} = \rho_x \mathcal{K}'$, with \mathcal{K}' not acting on \mathbf{q}_1 , but \mathbf{k} . Let us study the following cases:

- **Real Superconducting OP:**

By setting the imaginary part of the pairing potential equal to zero, the system obtains the chiral symmetry $\Pi = \tau_y \rho_z$. Additionally we find $\Theta = \rho_x \mathcal{K}'$ and $\Xi = \tau_y \rho_y \mathcal{K}'$, resulting in the class $\text{BDI} \oplus \text{BDI}$.

- **Complex Superconducting OP:**

The inclusion of a complex pairing potential breaks both chiral and generalized time-reversal symmetry, due to the presence of all Nambu matrices. The Hamiltonian resides in the class $\text{D} \oplus \text{D}$ with $\Xi = \tau_y \rho_y \mathcal{K}'$.

Double- Q Charge Spin Density Wave

This system only has the symmetry σ_y , if the profile is defined as in Eqs. 2.2. The Hamiltonian gets on the block form

$$\begin{aligned} \widehat{\mathcal{H}}^\sigma(\mathbf{k}) = & \tau_z \left[\hat{h}_0^+(\mathbf{k}) + \hat{h}_1^-(\mathbf{k})\lambda_z + \hat{h}_2^-(\mathbf{k})\rho_z + \hat{h}_3^+(\mathbf{k})\lambda_z\rho_z \right] + \sigma \frac{\widehat{M}_z\rho_x + \widehat{M}_z\lambda_x}{2} \\ & + \tau_x \left[\hat{\Delta}_0^{+\text{Re}}(\mathbf{k}) + \hat{\Delta}_1^{-\text{Re}}(\mathbf{k})\lambda_z + \hat{\Delta}_2^{-\text{Re}}(\mathbf{k})\rho_z + \hat{\Delta}_3^{+\text{Re}}(\mathbf{k})\lambda_z\rho_z \right] \\ & - \tau_y \left[\hat{\Delta}_0^{+\text{Im}}(\mathbf{k}) + \hat{\Delta}_1^{-\text{Im}}(\mathbf{k})\lambda_z + \hat{\Delta}_2^{-\text{Im}}(\mathbf{k})\rho_z + \hat{\Delta}_3^{+\text{Im}}(\mathbf{k})\lambda_z\rho_z \right]. \end{aligned} \quad (\text{C.2})$$

Since the Hamiltonian maintains its structure in the momentum transfer spaces, one retrieves the usual complex conjugation $\mathcal{K} = \lambda_x\rho_x\mathcal{K}'$.

- **Real Superconducting OP:**

By setting the imaginary part of the pairing potential equal to zero, the system obtains the chiral symmetry $\Pi = \tau_y\lambda_z\rho_z$. Additionally we find $\Theta = \lambda_x\rho_x\mathcal{K}'$ and $\Xi = \tau_y\lambda_y\rho_y\mathcal{K}'$, resulting in the class $\text{CI} \oplus \text{CI}$.

- **Complex Superconducting OP:**

The inclusion of a complex pairing potential breaks both chiral and generalized time-reversal symmetry, due to the presence of all Nambu matrices. The Hamiltonian resides in the class $\text{C} \oplus \text{C}$ with $\Xi = \tau_y\lambda_y\rho_y\mathcal{K}'$.

Double- Q Spin-Vortex Crystal

In this magnetic phase the Hamiltonian enjoys the symmetry $\lambda_z\rho_z\sigma_z$. The moments are assumed to be in the (x, y) -plane in spin space. The Hamiltonian is block diagonalized through the unitary operator $\widehat{\mathcal{O}} = (\lambda_z\rho_z\sigma_z + \sigma_x)/\sqrt{2}$, where we obtain

$$\begin{aligned} \widehat{\mathcal{O}}^\dagger \widehat{\mathcal{H}}(\mathbf{k}) \widehat{\mathcal{O}} = & \tau_z \left[\hat{h}_1^+(\mathbf{k}) + \hat{h}_2^-(\mathbf{k})\lambda_z + \hat{h}_3^-(\mathbf{k})\rho_z + \hat{h}_4^+(\mathbf{k})\lambda_z\rho_z \right] + \frac{\sigma\widehat{M}_x\rho_x - \widehat{M}_y\lambda_x\rho_z}{2} \\ & + \tau_x \left[\hat{\Delta}_1^{+\text{Re}}(\mathbf{k}) + \hat{\Delta}_2^{-\text{Re}}(\mathbf{k})\lambda_z + \hat{\Delta}_3^{-\text{Re}}(\mathbf{k})\rho_z + \hat{\Delta}_4^{+\text{Re}}(\mathbf{k})\lambda_z\rho_z \right] \\ & - \tau_y \left[\hat{\Delta}_1^{+\text{Im}}(\mathbf{k}) + \hat{\Delta}_2^{-\text{Im}}(\mathbf{k})\lambda_z + \hat{\Delta}_3^{-\text{Im}}(\mathbf{k})\rho_z + \hat{\Delta}_4^{+\text{Im}}(\mathbf{k})\lambda_z\rho_z \right]. \end{aligned} \quad (\text{C.3})$$

The usual representation of complex conjugation is conserved $\mathcal{K} = \lambda_x\rho_x\mathcal{K}'$.

- **Real Superconducting OP:**

By setting the imaginary part of the pairing potential equal to zero, the system obtains the chiral symmetry $\Pi = \tau_y\lambda_z\rho_z$. Additionally we find $\Theta = \lambda_y\rho_x\mathcal{K}'$ and $\Xi = \tau_y\lambda_x\rho_y\mathcal{K}'$, resulting in the class $\text{BDI} \oplus \text{BDI}$. Note that the magnetic texture in 1D cannot be defined, since it takes the form of the magnetic helix.

- **Complex Superconducting OP:**

The inclusion of a complex pairing potential breaks both chiral and generalized time-reversal symmetry, due to the presence of all Nambu matrices. The Hamiltonian resides in the class $\text{D} \oplus \text{D}$ with $\Xi = \tau_y\lambda_x\rho_y\mathcal{K}'$.

Single- \mathbf{Q} Magnetic Helix (•)

Since this specific magnetic texture is single- \mathbf{Q} nested, we only need to do the folding along the nesting direction \mathbf{Q} . Additionally the Hamiltonian has the unitary symmetries $\rho_z\sigma_y$, allowing for a unitary transformation with the operator $\hat{\mathcal{O}} = (\rho_z\sigma_y + \sigma_x)/\sqrt{2}$:

$$\begin{aligned} \hat{\mathcal{O}}^\dagger \hat{\mathcal{H}}(\mathbf{k}) \hat{\mathcal{O}} = & \tau_z \left[\hat{h}_0^+(\mathbf{k}) + \hat{h}_2^-(\mathbf{k})\rho_z \right] + \widehat{M} \frac{\sigma - 1}{2} \rho_y \\ & + \tau_x \left[\hat{\Delta}_0^{+\text{Re}}(\mathbf{k}) + \hat{\Delta}_2^{-\text{Re}}(\mathbf{k})\rho_z \right] - \tau_y \left[\hat{\Delta}_0^{+\text{Im}}(\mathbf{k}) + \hat{\Delta}_2^{-\text{Im}}(\mathbf{k})\rho_z \right]. \end{aligned} \quad (\text{C.4})$$

Clearly we are only interested in the $\sigma = -1$ block, which results in a Single- \mathbf{Q} magnetic stripe phase. We therefore get the same classification.

- **Real Superconducting OP:**

By setting the imaginary part of the pairing potential equal to zero, the system obtains the chiral symmetry $\Pi = \tau_y\rho_z$. Additionally we find $\Theta = \rho_x\mathcal{K}'$ and $\Xi = \tau_y\rho_y\mathcal{K}'$, resulting in the class $\text{BDI} \oplus \text{BDI}$.

- **Complex Superconducting OP:**

The inclusion of a complex pairing potential breaks both chiral and generalized time-reversal symmetry, due to the presence of all Nambu matrices. The Hamiltonian resides in the class $\text{D} \oplus \text{D}$ with $\Xi = \tau_y\rho_y\mathcal{K}'$.

Double- \mathbf{Q} Stripe with in-plane Helix (•)

The magnetic texture has the unitary symmetry $\lambda_z\rho_z\sigma_y$. This symmetry allows for a block diagonalization with the unitary operator $\hat{\mathcal{O}} = (\lambda_z\rho_z\sigma_y + \sigma_z)/\sqrt{2}$, as such

$$\begin{aligned} \hat{\mathcal{O}}^\dagger \hat{\mathcal{H}}(\mathbf{k}) \hat{\mathcal{O}} = & \tau_z \left[\hat{h}_0^+(\mathbf{k}) + \hat{h}_1^-(\mathbf{k})\lambda_z + \hat{h}_2^-(\mathbf{k})\rho_z + \hat{h}_3^+(\mathbf{k})\lambda_z\rho_z \right] \\ & - \frac{\sigma\widehat{M}_s\rho_x}{2} + \frac{-\widehat{M}_x\lambda_x\rho_z + \sigma\widehat{M}_z\lambda_x}{2} \\ & + \tau_x \left[\hat{\Delta}_0^{+\text{Re}}(\mathbf{k}) + \hat{\Delta}_1^{-\text{Re}}(\mathbf{k})\lambda_z + \hat{\Delta}_2^{-\text{Re}}(\mathbf{k})\rho_z + \hat{\Delta}_3^{+\text{Re}}(\mathbf{k})\lambda_z\rho_z \right] \\ & - \tau_y \left[\hat{\Delta}_0^{+\text{Im}}(\mathbf{k}) + \hat{\Delta}_1^{-\text{Im}}(\mathbf{k})\lambda_z + \hat{\Delta}_2^{-\text{Im}}(\mathbf{k})\rho_z + \hat{\Delta}_3^{+\text{Im}}(\mathbf{k})\lambda_z\rho_z \right]. \end{aligned} \quad (\text{C.5})$$

We obtain the usual representation of complex conjugations $\mathcal{K} = \lambda_x\rho_x\mathcal{K}'$.

- **Real Superconducting OP:**

By setting the imaginary part of the pairing potential equal to zero, the system obtains the chiral symmetry $\Pi = \tau_y\lambda_z\rho_z$. Additionally we find $\Theta = 0$ and $\Xi = 0$, resulting in the class $\text{AIII} \oplus \text{AIII}$.

- **Complex Superconducting OP:**

The inclusion of a complex pairing potential breaks chiral symmetry, due to the presence of all Nambu matrices. The Hamiltonian is therefore left in the class $\text{A} \oplus \text{A}$.

Double- Q Stripe with out-of-plane Helix (◦)

The Hamiltonian in this magnetic phase has the unitary symmetry $\lambda_z \sigma_z$, allowing for a unitary transformation with the operator $\hat{O} = (\lambda_z \sigma_z + \sigma_x)/\sqrt{2}$, which results in the block Hamiltonian

$$\begin{aligned} \hat{\mathcal{H}}^\sigma(\mathbf{k}) = & \tau_z \left[\hat{h}_0^+(\mathbf{k}) + \hat{h}_1^-(\mathbf{k})\lambda_z + \hat{h}_2^-(\mathbf{k})\rho_z + \hat{h}_3^+(\mathbf{k})\lambda_z\rho_z \right] + \frac{\sigma\widehat{M}_s\lambda_z\rho_x}{2} + \frac{\widehat{M}_x\lambda_y\sigma + \widehat{M}_y\lambda_y}{2} \\ & + \tau_x \left[\hat{\Delta}_0^{+\text{Re}}(\mathbf{k}) + \hat{\Delta}_1^{-\text{Re}}(\mathbf{k})\lambda_z + \hat{\Delta}_2^{-\text{Re}}(\mathbf{k})\rho_z + \hat{\Delta}_3^{+\text{Re}}(\mathbf{k})\lambda_z\rho_z \right] \\ & - \tau_y \left[\hat{\Delta}_0^{+\text{Im}}(\mathbf{k}) + \hat{\Delta}_1^{-\text{Im}}(\mathbf{k})\lambda_z + \hat{\Delta}_2^{-\text{Im}}(\mathbf{k})\rho_z + \hat{\Delta}_3^{+\text{Im}}(\mathbf{k})\lambda_z\rho_z \right]. \end{aligned} \quad (\text{C.6})$$

We find the topological classification to be the following:

- **Real Superconducting OP:**

By setting the imaginary part of the pairing potential equal to zero, the system obtains the chiral symmetry $\Pi = \tau_y \lambda_z \rho_z$. Additionally we find $\Theta = \lambda_x \rho_y \mathcal{K}'$ and $\Xi = \tau_y \lambda_y \rho_x \mathcal{K}'$, resulting in the class DIII.

- **Complex Superconducting OP:**

The inclusion of a complex pairing potential breaks both chiral and generalized time-reversal symmetry, due to the presence of all Nambu matrices. The Hamiltonian resides in the class D with $\Xi = \tau_y \lambda_y \rho_x \mathcal{K}'$.

Double- Q Double Parallel Helix (◐)

The Hamiltonian enjoys the symmetry $\lambda_z \rho_z \sigma_y$, allowing for a block diagonalization with the operator $\hat{O} = (\lambda_z \rho_z \sigma_y + \sigma_x)/\sqrt{2}$:

$$\begin{aligned} \hat{O}^\dagger \hat{\mathcal{H}}(\mathbf{k}) \hat{O} = & \tau_z \left[\hat{h}_0^+(\mathbf{k}) + \hat{h}_1^-(\mathbf{k})\lambda_z + \hat{h}_2^-(\mathbf{k})\rho_z + \hat{h}_3^+(\mathbf{k})\lambda_z\rho_z \right] + \widehat{M}\rho_y \frac{\sigma - \lambda_z}{2} + \widehat{M}\lambda_y \frac{\sigma - \rho_z}{2} \\ & + \tau_x \left[\hat{\Delta}_0^{+\text{Re}}(\mathbf{k}) + \hat{\Delta}_1^{-\text{Re}}(\mathbf{k})\lambda_z + \hat{\Delta}_2^{-\text{Re}}(\mathbf{k})\rho_z + \hat{\Delta}_3^{+\text{Re}}(\mathbf{k})\lambda_z\rho_z \right] \\ & - \tau_y \left[\hat{\Delta}_0^{+\text{Im}}(\mathbf{k}) + \hat{\Delta}_1^{-\text{Im}}(\mathbf{k})\lambda_z + \hat{\Delta}_2^{-\text{Im}}(\mathbf{k})\rho_z + \hat{\Delta}_3^{+\text{Im}}(\mathbf{k})\lambda_z\rho_z \right]. \end{aligned} \quad (\text{C.7})$$

- **Real Superconducting OP:**

By setting the imaginary part of the pairing potential equal to zero, the system obtains the chiral symmetry $\Pi = \tau_y \lambda_z \rho_z$. Additionally we find $\Theta = 0$ and $\Xi = 0$, resulting in the class AIII \oplus AIII.

- **Complex Superconducting OP:**

The inclusion of a complex pairing potential breaks both chiral and generalized time-reversal symmetry, due to the presence of all Nambu matrices. The Hamiltonian resides in the class A \oplus A.

Double- Q C_4 -symmetric Spin-Whirl Crystal (●)

The system has no unitary symmetries, and obtains therefore the form

$$\begin{aligned}
 \widehat{\mathcal{H}}(\mathbf{k}) = & \tau_z \left[\widehat{h}_0^+(\mathbf{k}) + \widehat{h}_1^-(\mathbf{k})\lambda_z + \widehat{h}_2^-(\mathbf{k})\rho_z + \widehat{h}_3^+(\mathbf{k})\lambda_z\rho_z \right] \\
 & + \frac{\widehat{M}_x\rho_x\sigma_x + \widehat{M}_\perp\rho_y\sigma_z}{2} + \frac{\widehat{M}_x\lambda_x\sigma_x + \widehat{M}_\perp\lambda_y\sigma_y}{2} \\
 & + \tau_x \left(\widehat{\Delta}_0^{+\text{Re}}(\mathbf{k}) + \widehat{\Delta}_1^{-\text{Re}}(\mathbf{k})\lambda_z + \widehat{\Delta}_2^{-\text{Re}}(\mathbf{k})\rho_z + \widehat{\Delta}_3^{+\text{Re}}(\mathbf{k})\lambda_z\rho_z \right) \\
 & - \tau_y \left(\widehat{\Delta}_0^{+\text{Im}}(\mathbf{k}) + \widehat{\Delta}_1^{-\text{Im}}(\mathbf{k})\lambda_z + \widehat{\Delta}_2^{-\text{Im}}(\mathbf{k})\rho_z + \widehat{\Delta}_3^{+\text{Im}}(\mathbf{k})\lambda_z\rho_z \right).
 \end{aligned} \tag{C.8}$$

- **Real Superconducting OP:**

By setting the imaginary part of the pairing potential equal to zero, the system obtains the chiral symmetry $\Pi = \tau_y\lambda_z\rho_z$. Additionally we find $\Theta = i\lambda_y\rho_y\sigma_y\mathcal{K}'$ and $\Xi = \tau_y\lambda_x\rho_x\sigma_y\mathcal{K}'$, resulting in the class DIII.

- **Complex Superconducting OP:**

The inclusion of a complex pairing potential breaks both chiral and generalized time-reversal symmetry, due to the presence of all Nambu matrices. The Hamiltonian resides in the class D with $\Xi = \tau_y\lambda_x\rho_x\sigma_y\mathcal{K}'$.

Double- Q C_2 -symmetric Spin-Whirl Crystal (●)

Similar to the phase described above, this Hamiltonian has now unitary symmetries, and gets on the form:

$$\begin{aligned}
 \widehat{\mathcal{H}}(\mathbf{k}) = & \tau_z \left[\widehat{h}_0^+(\mathbf{k}) + \widehat{h}_1^-(\mathbf{k})\lambda_z + \widehat{h}_2^-(\mathbf{k})\rho_z + \widehat{h}_3^+(\mathbf{k})\lambda_z\rho_z \right] \\
 & + \widehat{M}_s \frac{\rho_y\sigma_x + \rho_x\sigma_z}{2} + \frac{\widehat{M}_y\lambda_y\sigma_y + \widehat{M}_z\lambda_x\sigma_z}{2} \\
 & + \tau_x \left[\widehat{\Delta}_0^{+\text{Re}}(\mathbf{k}) + \widehat{\Delta}_1^{-\text{Re}}(\mathbf{k})\lambda_z + \widehat{\Delta}_2^{-\text{Re}}(\mathbf{k})\rho_z + \widehat{\Delta}_3^{+\text{Re}}(\mathbf{k})\lambda_z\rho_z \right] \\
 & - \tau_y \left[\widehat{\Delta}_0^{+\text{Im}}(\mathbf{k}) + \widehat{\Delta}_1^{-\text{Im}}(\mathbf{k})\lambda_z + \widehat{\Delta}_2^{-\text{Im}}(\mathbf{k})\rho_z + \widehat{\Delta}_3^{+\text{Im}}(\mathbf{k})\lambda_z\rho_z \right].
 \end{aligned} \tag{C.9}$$

- **Real Superconducting OP:**

By setting the imaginary part of the pairing potential equal to zero, the system obtains the chiral symmetry $\Pi = \tau_y\lambda_z\rho_z$. Additionally we find $\Theta = i\lambda_y\rho_y\sigma_y\mathcal{K}'$ and $\Xi = \tau_y\lambda_x\rho_x\sigma_y\mathcal{K}'$, resulting in the class DIII.

- **Complex Superconducting OP:**

The inclusion of a complex pairing potential breaks both chiral and generalized time-reversal symmetry, due to the presence of all Nambu matrices. The Hamiltonian resides in the class D with $\Xi = \tau_y\lambda_x\rho_x\sigma_y\mathcal{K}'$.

Appendix D

Matrix Representation of C_{4v} Elements

Matrix Representation in Orbital Space

$$\begin{aligned}
 \hat{d}_\kappa(E) &= \mathbf{1}_\kappa & \hat{d}_\kappa(C_2) &= \begin{pmatrix} -1 & 0 & 0 & 0 & 0 \\ 0 & -1 & 0 & 0 & 0 \\ 0 & 0 & 1 & 0 & 0 \\ 0 & 0 & 0 & 1 & 0 \\ 0 & 0 & 0 & 0 & 1 \end{pmatrix}, \\
 \hat{d}_\kappa(C_4) &= \begin{pmatrix} 0 & -1 & 0 & 0 & 0 \\ 1 & 0 & 0 & 0 & 0 \\ 0 & 0 & -1 & 0 & 0 \\ 0 & 0 & 0 & -1 & 0 \\ 0 & 0 & 0 & 0 & 1 \end{pmatrix}, & \hat{d}_\kappa(\bar{C}_4) &= \begin{pmatrix} 0 & 1 & 0 & 0 & 0 \\ -1 & 0 & 0 & 0 & 0 \\ 0 & 0 & -1 & 0 & 0 \\ 0 & 0 & 0 & -1 & 0 \\ 0 & 0 & 0 & 0 & 1 \end{pmatrix}, \\
 \hat{d}_\kappa(\sigma_{xz}) &= \begin{pmatrix} 1 & 0 & 0 & 0 & 0 \\ 0 & -1 & 0 & 0 & 0 \\ 0 & 0 & -1 & 0 & 0 \\ 0 & 0 & 0 & 1 & 0 \\ 0 & 0 & 0 & 0 & 1 \end{pmatrix} & \hat{d}_\kappa(\sigma_{yz}) &= \begin{pmatrix} -1 & 0 & 0 & 0 & 0 \\ 0 & 1 & 0 & 0 & 0 \\ 0 & 0 & -1 & 0 & 0 \\ 0 & 0 & 0 & 1 & 0 \\ 0 & 0 & 0 & 0 & 1 \end{pmatrix}, & (D.1) \\
 \hat{d}_\kappa(\sigma_{x+y}) &= \begin{pmatrix} 0 & 1 & 0 & 0 & 0 \\ 1 & 0 & 0 & 0 & 0 \\ 0 & 0 & 1 & 0 & 0 \\ 0 & 0 & 0 & -1 & 0 \\ 0 & 0 & 0 & 0 & 1 \end{pmatrix}, & \hat{d}_\kappa(\sigma_{x-y}) &= \begin{pmatrix} 0 & -1 & 0 & 0 & 0 \\ -1 & 0 & 0 & 0 & 0 \\ 0 & 0 & 1 & 0 & 0 \\ 0 & 0 & 0 & -1 & 0 \\ 0 & 0 & 0 & 0 & 1 \end{pmatrix}.
 \end{aligned}$$